National Library of Canada
Bibliothèque nationale du Canada

Canadian Theses Service
Services des thèses canadiennes

Ottawa, Canada
K1A 0N4

CANADIAN THESES

THÈSES CANADIENNES

NOTICE

The quality of this microfiche is heavily dependent upon the quality of the original thesis submitted for microfilming. Every effort has been made to ensure the highest quality of reproduction possible.

If pages are missing, contact the university which granted the degree.

Some pages may have indistinct print especially if the original pages were typed with a poor typewriter ribbon or if the university sent us an inferior photocopy.

Previously copyrighted materials (journal articles, published tests, etc.) are not filmed.

Reproduction in full or in part of this film is governed by the Canadian Copyright Act, R.S.C. 1970, c. C-30. Please read the authorization forms which accompany this thesis.

AVIS

La qualité de cette microfiche dépend grandement de la qualité de la thèse soumise au microfilmage. Nous avons tout fait pour assurer une qualité supérieure de reproduction.

S'il manque des pages, veuillez communiquer avec l'université qui a conféré le grade.

La qualité d'impression de certaines pages peut laisser à désirer, surtout si les pages originales ont été dactylographiées à l'aide d'un ruban usé ou si l'université nous a fait parvenir une photocopie de qualité inférieure.

Les documents qui font déjà l'objet d'un droit d'auteur (articles de revue, examens publiés, etc.) ne sont pas microfilmés.

La reproduction, même partielle, de ce microfilm est soumise à la Loi canadienne sur le droit d'auteur, SRC 1970, c. C-30. Veuillez prendre connaissance des formules d'autorisation qui accompagnent cette thèse.

THIS DISSERTATION
HAS BEEN MICROFILMED
EXACTLY AS RECEIVED

LA THÈSE A ÉTÉ
MICROFILMÉE TELLE QUE
NOUS L'AVONS REÇUE

NL 339 (r. 86/01)

Canada

224

0-315-26955-3

National Library of Canada | Bibliothèque nationale du Canada

Canadian Theses Division | Division des thèses canadiennes

Ottawa, Canada
K1A 0N4

PERMISSION TO MICROFILM — AUTORISATION DE MICROFILMER

• Please print or type — Écrire en lettres moulées ou dactylographier

Full Name of Author — Nom complet de l'auteur

John Stiksma

Date of Birth — Date de naissance

June 19, 1960

Country of Birth — Lieu de naissance

Canada

Permanent Address — Résidence fixe

8807 - 160 St.
Edmonton, Alberta T5R 2H6

Title of Thesis — Titre de la thèse

Stress Corrosion Cracking of a Dual-Phase Steel in a Carbonate - Bicarbonate Environment

University — Université

University of Alberta

Degree for which thesis was presented — Grade pour lequel cette thèse fut présentée

M.Sc. in Metallurgical Engineering

Year this degree conferred — Année d'obtention de ce grade

1984

Name of Supervisor — Nom du directeur de thèse

Dr. S.A. Bradford

Permission is hereby granted to the NATIONAL LIBRARY OF CANADA to microfilm this thesis and to lend or sell copies of the film.

The author reserves other publication rights, and neither the thesis nor extensive extracts from it may be printed or otherwise reproduced without the author's written permission.

L'autorisation est, par la présente, accordée à la BIBLIOTHÈQUE NATIONALE DU CANADA de microfilmer cette thèse et de prêter ou de vendre des exemplaires du film.

L'auteur se réserve les autres droits de publication; ni la thèse ni de longs extraits de celle-ci ne doivent être imprimés ou autrement reproduits sans l'autorisation écrite de l'auteur.

Date

March 9, 1984

Signature

John Stiksma

NL-91 (4/77)

THE UNIVERSITY OF ALBERTA

Stress Corrosion Cracking of a Dual-Phase Steel in a Carbonate-Bicarbonate Environment

by

© John Stiksma

A THESIS

SUBMITTED TO THE FACULTY OF GRADUATE STUDIES AND RESEARCH

IN PARTIAL FULFILMENT OF THE REQUIREMENTS FOR THE DEGREE

OF Master of Science in Metallurgical Engineering

Department of Mineral Engineering

EDMONTON, ALBERTA

SPRING 1984

THE UNIVERSITY OF ALBERTA

RELEASE FORM

NAME OF AUTHOR John Stiksma

TITLE OF THESIS Stress Corrosion Cracking of a Dual-Phase Steel in a Carbonate-Bicarbonate Environment

DEGREE FOR WHICH THESIS WAS PRESENTED Master of Science in Metallurgical Engineering

YEAR THIS DEGREE GRANTED SPRING 1984

Permission is hereby granted to THE UNIVERSITY OF ALBERTA LIBRARY to reproduce single copies of this thesis and to lend or sell such copies for private, scholarly or scientific research purposes only.

The author reserves other publication rights, and neither the thesis nor extensive extracts from it may be printed or otherwise reproduced without the author's written permission.

(SIGNED) John Stiksma

PERMANENT ADDRESS:

8807 - 160 St.
Edmonton, Alberta.
T5R 2H6

DATED March 9 1984

THE UNIVERSITY OF ALBERTA

FACULTY OF GRADUATE STUDIES AND RESEARCH

The undersigned certify that they have read, and recommend to the Faculty of Graduate Studies and Research, for acceptance, a thesis entitled Stress Corrosion Cracking of a Dual-Phase Steel in a Carbonate-Bicarbonate Environment submitted by John Stiksma in partial fulfilment of the requirements for the degree of Master of Science in Metallurgical Engineering.

Samuel G. Bradford

Supervisor

T. K. Ctaell

W. Gobwayman

F. Vitovec

Date February 7, 1984

Dedication

To my parents and Arlene.

Abstract

The stress corrosion cracking (SCC) susceptibility of a Dofasco experimental as-rolled dual-phase steel in a 0.5 M Na_2CO_3 - 0.5 M $NaHCO_3$ solution at varying potentials and temperatures was investigated. Constant strain rate tests were used to evaluate SCC susceptibility. A pipeline steel (X-65) with similar mechanical properties was also tested in the same way and the results were compared. It is known that SCC of pipeline steels occurs in a critical range of potentials above the primary passivation potential (anodic peak). It was found that the dual-phase steel is less susceptible to SCC than the pipeline steel (X-65) in the "critical" potential range. Briefly-exposed, metallographically-polished dual-phase steel samples were shown to be selectively attacked at the martensite phase in the "critical" potential range. Since the martensite phase is not aligned in any way, there is no susceptible cracking path. This is reflected in the constant strain rate test results. Also, hydrogen embrittlement of the dual-phase steel is very similar to that of the pipeline steel (X-65) under the same conditions. For both steels, a considerable amount of deformation is required before hydrogen embrittlement occurs.

Acknowledgements

I would like to express my sincere thanks to my supervisor, Dr. S.A. Bradford, for his guidance and help.

My appreciation is also extended to the technical staff in the department for their help, specifically,

Mrs. Christina Barker,

Mr. Tom Forman,

Mr. Bob Konzuk, and

Mr. Henryk Skrzypek.

Also, I would like to thank Dominion Foundries and Steel, Limited (Dofasco) for supplying the dual-phase steel used in the research.

Table of Contents

Chapter		Page
1.	Introduction	1
2.	Theory	3
	2.1 Electrochemistry	3
	2.1.1 Thermodynamics	3
	2.1.2 Electrode Kinetics	5
	2.1.3 Mixed Electrodes	10
	2.1.4 Passivity	12
	2.1.5 Electrochemical Corrosion-Rate Measurements	14
	2.1.5.1 Polarization measurements	14
	2.1.5.2 Tafel extrapolation method	15
	2.1.5.3 Three-point method	16
	2.2 Stress Corrosion Cracking	19
	2.2.1 Factors Affecting SCC	19
	2.2.2 Mechanism of SCC	20
	2.2.3 Methods of Prevention	22
	2.2.4 Test Methods and Interpretation of Test Data	22
	2.2.4.1 Smooth specimen - constant strain rate test	23
3.	Literature Survey	26
	3.1 SCC of Steels in Carbonate-Bicarbonate Solutions	26
	3.1.1 SCC of Buried Pipelines	26
	3.1.2 SCC of Steel in the Lab	29
	3.1.2.1 Carbon steel	29
	3.1.2.2 Pipeline steel	32

3.2 High-Strength Low-Alloy (HSLA) Steels 33
3.2.1 HSLA Pipeline Steels 33
3.2.1.1 Ferrite-pearlite steel 34
3.2.1.2 Bainite/acicular ferrite steel 35
3.2.1.3 Multiphase steel 36
3.2.2 Dual-Phase Steel 39
3.2.2.1 Production of dual-phase steel 40
3.2.2.2 Structure-property relationships ..41
3.2.2.3 Uses 43
3.3 Environmental Attack of Dual-Phase Steel 44
4. Materials and Solutions 46
4.1 Dual-Phase Steel 46
4.2 X-65 Steel 46
4.3 Test Solution 47
4.4 Inert Oil Medium 47
5. Experimental Procedure 48
5.1 Microscopic Examination of the Steels 48
5.1.1 Dual-Phase Steel 48
5.1.2 X-65 Steel 49
5.1.3 Examination with the Microscope 49
5.2 Polarization Curves 51
5.2.1 Equipment 51
5.2.2 Cell Arrangement 52
5.2.3 Temperature Control 53
5.2.4 Sample Preparation 54
5.2.5 Scanning Procedure 54
5.3 Constant Potential Tests 57

5.3.1 Equipment 57
5.3.2 Cell Arrangement 57
5.3.3 Temperature Control 57
5.3.4 Sample Preparation 57
5.3.5 Test Procedure 58
5.3.5.1 Extended rest potential tests 59
5.3.6 Examination with the Microscope 59
5.4 Constant Strain Rate Tests 60
5.4.1 Specimen Preparation 60
5.4.2 Equipment 60
5.4.2.1 Material Test System 61
5.4.3 Cell Arrangement 62
5.4.3.1 Recirculation system 62
5.4.4 Temperature Control 63
5.4.5 Test Procedure 63
5.4.5.1 Oil tests 65
5.4.6 Examination with the Microscope 65
6. Results and Discussion 66
6.1 Microscopic Examination 66
6.1.1 Dual-Phase Steel 66
6.1.2 X-65 Steel 66
6.2 Polarization Curves 68
6.2.1 Dual-Phase Steel 68
6.2.2 X-65 Steel 71
6.2.3 Effect of Aeration 72
6.2.4 Corrosion Rate Calculations 73
6.2.5 Effect of Temperature 74

6.3 Constant Potential Tests 76

6.3.1 Dual-Phase Steel 76

6.3.1.1 Extended rest potential tests 78

6.3.2 X-65 Steel 78

6.4 Constant Strain Rate Tests 80

6.4.1 Dual-Phase Steel 80

6.4.2 Scanning Electron Microscopy 82

6.4.3 X-65 Steel 83

6.5 Comparison of the Steels 85

6.6 Suitability of Dual-Phase Steel for Pipeline Application 88

7. Conclusions 90

References 160

Appendix A 165

List of Tables

Table		Page
1.	Some Environments that may cause SCC of Ordinary Steels	91
2.	Compositions of some Solutions near Cracks (from Fessler and Barlo[13])	92
3.	Typical Compositions of Dual-Phase Steels (from Speich[24])	93
4.	Composition and Mechanical Properties of the Dofasco Dual-Phase Steel	94
5.	Composition and Mechanical Properties of the X-65 Pipeline Steel	95
6.	Active-Passive Parameters as a function of Temperature for Dual-Phase Steel	96
7.	Active-Passive Parameters as a function of Temperature for X-65 Pipeline Steel	97
8.	Active-Passive Parameters as a function of Dissolved Oxygen for Dual-Phase Steel	98
9.	Possible Reactions in Carbonate/Bicarbonate Solution	99
10.	Corrosion Rate as a function of Temperature for Dual-Phase Steel	100
11.	Corrosion Rate as a function of Temperature for X-65 Steel	101
12.	Current Densities as a function of Temperature	102

Table Page

13. Constant Strain Rate Test Results for Dual-Phase Steel 103

14. Constant Strain Rate Test Results for X-65 Steel 104

15. Comparison of Dual-Phase Steel and X-65 Steel 105

A.1. Current Densities Obtained From Polarization Curves 166

List of Figures

Figure		Page
1.	Potential-pH Diagram for the Fe-H_2O System (modified from Pourbaix[4])	106
2.	Activation Polarization Curve of a Hydrogen Electrode	107
3.	Concentration Polarization Curve	107
4.	Effect of Environmental Variables on Concentration Polarization	108
5.	Combined Polarization Curve	108
6.	Behavior of Fe in Carbonate Solution	109
7.	Corrosion of Metal under Diffusion Control	110
8.	Anodic Dissolution Behavior of an Active-Passive Metal	110
9.	Behavior of an Active-Passive Metal under Corrosive Conditions	111
10.	Electric Circuit for Cathodic Polarization Measurement	111
11.	Applied Current Cathodic Polarization Curve	112
12.	SCC Parameters (from Payer et al.[10])	112
13.	Polarization Curves and SCC Test Results for Mild Steel in 1N Na_2CO_3 - 1N $NaHCO_3$ at 90°C (modified from Sutcliffe et al.[1])	113
14.	Effect of Temperature upon SCC of Mild Steel at Various Potentials in 1N Na_2CO_3 - 1N $NaHCO_3$ at 90°C (modified from Sutcliffe et al.[1])	114
15.	The pH Dependence of the SCC Range for Pipeline Steel (from Payer et al.[2])	115
16.	Comparison of Stress-Strain Curves for Dual-Phase Steel and Conventional HSLA Steel (from Speich[24])	116
17.	Continuous-Cooling Transformation for As-Rolled Dual-Phase Steel (from Speich[24])	116

Figure Page

18. Polarization Equipment....117
19. Cell Arrangement....117
20. Working Electrode Assembly....118
21. Steel Mounted in Bakelite....119
22. Counter Electrode Assembly....119
23. Salt Bridge Assembly....120
24. Temperature Control....120
25. Tensile Specimen....121
26. Reduced Section of Tensile Specimen....121
27. Material Test System....122
28. Test Cell....122
29. Test Cell Dimensions (side view)....123
30. Test Cell Dimensions (top view)....124
31. Cemented Nylon Sleeve....125
32. Recirculation System....126
33. Dofasco Dual-Phase Steel (600X)....127
34. X-65 Pipeline Steel (600X)....127
35. Polarization Curve of Dual-Phase Steel at 22°C....128
36. Polarization Curve of Dual-Phase Steel at 50°C....129
37. Polarization Curve of Dual-Phase Steel at 70°C....130
38. Polarization Curve of Dual-Phase Steel at 90°C....131
39. Polarization Curve of X-65 Steel at 22°C....132
40. Polarization Curve of X-65 Steel at 50°C....133
41. Polarization Curve of X-65 Steel at 90°C....134

Figure Page

42. Polarization Curves of Dual-Phase Steel in Aerated and De-aerated Test Solution at 22°C.....135

43. Polarization Curves showing the Effect of Oxygen...136

44. Log i(c) and log i(p) versus 1/T Plot for Dual-Phase Steel.....137

45. Log i(c) versus 1/T Plot for X-65 Steel.....138

46. Log i(corr) versus 1/T Plot for Dual-Phase Steel.....139

47. Log i(corr) versus 1/T Plot for X-65 Steel.....140

48. Corrosion Attack of Dual-Phase Steel after 1 h at E(corr) and 50°C (600X).....141

49. Corrosion Attack of Dual-Phase Steel after 5 min at -0.800V vs. s.c.e. and 50°C (600X).....141

50. Corrosion Attack of Dual-Phase Steel after 5 min at E(pp) and 50°C (600X).....142

51. Corrosion Attack of Dual-Phase Steel after 5 min at -0.625V vs. s.c.e. and 50°C (600X).....143

52. Corrosion Attack of Dual-Phase Steel after 5 min at -0.600V vs. s.c.e. and 50°C (600X).....143

53. Corrosion Attack of X-65 Steel after 5 min at -0.790V vs. s.c.e. and 50°C (600X).....144

54. Corrosion Attack of X-65 Steel after 5 min at E(pp) and 50°C (600X).....144

55. Corrosion Attack of X-65 Steel after 5 min at -0.675V vs. s.c.e. and 50°C (600X).....145

56. Percent Elongation as a function of Potential for Dual-Phase Steel at 21°C.....146

57. Percent Elongation as a function of Potential for Dual-Phase Steel at 50°C.....147

Figure Page

58. Percent Elongation as a function of Potential for Dual-Phase Steel at 70°C.....148

59. Elongation Parameter as a function of Potential for Dual-Phase Steel at 21°C.....149

60. Elongation Parameter as a function of Potential for Dual-Phase Steel at 50°C.....150

61. Elongation Parameter as a function of Potential for Dual-Phase Steel at 70°C.....151

62. Specimen 1 (6.4X).....152

63. SEM Fractograph of Specimen 28 (1500X).....152

64. Specimen 12 (6.4X).....153

65. SEM Fractograph (cracked region) of Specimen 12 (1500X).....154

66. SEM Fractograph (overload region) of Specimen 12 (1500X).....154

67. Specimen 6 (6.4X).....155

68. SEM Fractograph of Specimen 6 (1500X).....155

69. Specimen 33 (6.4X).....156

70. SEM Fractograph of Specimen 33 (1500X).....156

71. Percent Elongation as a function of Potential for X-65 Steel at 21°C.....157

72. Elongation Parameter as a function of Potential for X-65 Steel at 21°C.....158

73. Effect of Hydrogen Charging on Percent Elongation of Dual-Phase Steel and X-65 Steel at 21°C.....159

A.1. 3-Point Method.....167

1. Introduction

Since 1965, stress corrosion cracking (SCC) has been blamed for a number of buried pipeline failures. The predominant environment responsible for SCC is a solution containing sodium carbonate (Na_2CO_3) and sodium bicarbonate ($NaHCO_3$) in varying amounts. This environment is believed to be formed when carbon dioxide from the soil reacts with the hydroxyl ions that are produced at the pipe by the action of cathodic protection currents.

Laboratory tests have been done on carbon and pipeline steels in carbonate-bicarbonate environments and it has been shown that SCC does occur in a critical range of potentials.[1-3] The critical range of potentials lies above the primary passivation potential (or anodic peak) in the region where a large anodic (active) current subsides to a small passive current. In this region, briefly-exposed, metallographically-polished steel specimens were observed to be attacked with structural dependence. The grain boundaries were selectively etched (or grooved) and this is believed to promote SCC by providing a susceptible microstructural cracking path. Therefore, SCC of carbon and pipeline steel in carbonate-bicarbonate environments is dependent on a critical combination of active and passive behavior.

In this thesis, the SCC susceptibility of a dual-phase steel in a carbonate-bicarbonate environment is investigated and compared to a pipeline steel with similar properties tested under the same conditions. Dual-phase steels are a

new class of high-strength, low-alloy (HSLA) steels characterized by a microstructure consisting of a dispersion of about 20 percent hard martensite particles in a soft, ductile ferrite matrix. Investigators have shown that dual-phase steels have a number of unique properties which include continuous yielding, a low 0.2 percent offset yield strength (≃50 ksi; 344 MPa), a high tensile strength (≃100 ksi; 690 MPa), a high work-hardening rate, and unusually high uniform and total elongation. The high work-hardening rate, combined with the high uniform elongation of these steels, gives them a formability equivalent to that of much lower strength steels.

2. Theory

2.1 Electrochemistry

Corrosion of metal is electrochemical in nature. To understand electrochemical processes one must be aware of the thermodynamic principles involved and also the electrode kinetics.

2.1.1 Thermodynamics

The thermodynamic principles applicable to corrosion phenomena and their limitations will be discussed.

Free energy change (ΔG) is related directly to the cell potential of an electrochemical reaction by the following equation:

$$\Delta G = -nEF$$

where n is the number of electrons involved in the reaction, F is the Faraday constant, and E is the cell potential.

Under standard conditions the cell potential can be calculated from the electromotive force (EMF) series which is composed of half-cell reactions. Since the concentrations of all reactants are maintained at unit activity, they are termed standard half-cells.

To determine the potential of a system in which the reactants are not at unit activity, the familiar Nernst equation can be employed.

$$E = E_0 + (2.3\ RT/nF)\ \log(a_{ox}/a_{red})$$

where E is the half-cell potential, E_0 is the standard half-cell potential, R is the gas constant, T is the absolute temperature, n is the number of electrons transferred, F is the Faraday constant, and a_{ox} and a_{red} are the activities (concentrations) of oxidized and reduced species. The more oxidized species present, the higher the oxidizing power resulting in a higher half-cell potential.

One general rule can be applied to corrosion using thermodynamics: *In any electrochemical reaction, the most negative or active half-cell tends to be oxidized, and the most positive or noble half-cell tends to be reduced.*

The above rule is very useful in predicting corrosion behavior. Metals with reversible potentials more active (negative) than hydrogen tend to corrode in acid solutions. Copper and silver are not corroded in acid solutions but if oxygen is present in solution copper and silver tend to corrode spontaneously.

Thermodynamics can be used to state a criterion for corrosion. *Corrosion will not occur unless the spontaneous direction of the reaction indicates metal oxidation.* Thermodynamics might show that a reaction can occur but in reality it proceeds at a negligible rate and therefore it is practically not occurring. Kinetics of the reaction therefore play an important role.

A lot of thermodynamic data can be shown graphically to simplify the interpretation of the data. Dr. M. Pourbaix developed potential-pH diagrams (Pourbaix diagrams).[4] Calculations using the Nernst equation and solubility data for various metal compounds are used to construct these plots. See Figure 1 for a Pourbaix diagram of the $Fe-H_2O$ system. These diagrams give predominance areas of species that are thermodynamically stable. The boundaries for the areas are set at a specific ion concentration, usually 10^{-4} Molar, which is the detection limit of most ions in solution.

The main uses of these diagrams are:

a. predicting the spontaneous direction of reactions,
b. estimating the composition of corrosion products, and
c. predicting environmental changes which will prevent or reduce corrosive attack.

One must remember that these potential-pH diagrams are thermodynamic diagrams. They represent equilibrium conditions and are not used to predict the rate of a reaction.

2.1.2 Electrode Kinetics

The kinetics or rate of corrosion is of utmost importance from an engineering standpoint. Corroding systems are not at equilibrium, and therefore thermodynamic calculations cannot be applied.

Some useful terms will be defined. *Anode* refers to the electrode where net oxidation occurs and *cathode* refers to the electrode where net reduction occurs. When corrosion occurs, the electrodes will not be at their equilibrium potential. This deviation from equilibrium potential is called *polarization*. *Polarization* can be defined as the shift of electrode potential resulting from a net current. The magnitude of polarization is called overvoltage, abbreviated η. The overvoltage is either negative or positive with respect to the equilibrium potential which is defined as zero.

At the equilibrium potential the rate of oxidation equals the rate of reduction ($r_{ox} = r_{red}$). There is no net reaction. The exchange-reaction rate can be expressed in terms of current density. The relationship between exchange-reaction rate and current density is shown by Faraday's Law:

$$r_{ox} = r_{red} = i_o/nF \text{ (moles/(cm}^2\text{.s))}$$

where i_o is the exchange current density and n and F have been previously defined.

The exchange current density (i_o) varies depending on the metal electrode; for example, the exchange current density of hydrogen on platinum is approximately 1 mA/cm^2, and on mercury is approximately 10^{-9} mA/cm^2.

The i_o depends on a number of variables, namely, the particular redox reaction, the electrode composition, the ratio of oxidized to reduced species, trace impurities, the roughness of the electrode, and the temperature. The i_o is difficult to predict and therefore must be determined experimentally.

Electrochemical polarization is divided into two main types - *activation* and *concentration* polarization. *Activation* polarization refers to electrochemical reactions which are controlled by a slow step in the reaction sequence. The relationship between reaction rate and overvoltage for activation polarization is:

$$\eta = \pm\beta \log(i/i_o)$$

where η is overvoltage, β is a constant, and i is the rate of oxidation or reduction in terms of current density. The equation is called the Tafel equation and β is termed usually the "Tafel slope" or "Tafel constant". For electrochemical reactions the value of β ranges between 0.05 and 0.15 volt, and in general, β is approximately 0.1 volt. Figure 2 shows the activation polarization curve of a hydrogen electrode. The rate of an electrochemical reaction is very sensitive to small changes in the electrode potential.

To illustrate the phenomenon of *concentration* polarization, consider the hydrogen evolution reaction. At

very high reduction rates, the region adjacent to the cathode electrode surface will become depleted of hydrogen ions. If the reduction rate is increased further, a limiting rate will be reached which is determined by the diffusion rate of hydrogen ions to the electrode surface. This limiting rate is the limiting diffusion current density i_L . It represents the maximum rate of reduction possible for a given system. The i_L is a function of a number of variables as shown by the equation:

$$i_L = DnFC_B / \delta$$

where D is the diffusion coefficient of the reacting ions, C_B is the concentration of the reacting ions in the bulk solution, and δ is the effective diffusion layer thickness.

The diffusion layer thickness is influenced by the shape of the particular electrode, the geometry of the system, and by agitation. The value of δ must be determined experimentally. Limiting diffusion current density is usually only significant during reduction processes and concentration polarization is usually negligible during metal dissolution reactions. The reason for this is, simply, that there is an almost unlimited supply of metal atoms for dissolution.

If we consider a hypothetical cathode in which there is no activation polarization, then the equation for concentration polarization is:

$$\eta = (2.3\ RT/nF)\ \log(1-i/i_L)$$

where η is the overpotential, and i is the rate of oxidation or reduction in terms of current density. Figure 3 shows a concentration polarization curve. Concentration polarization does not become apparent until the net reduction current density approaches the limiting value. Figure 4 shows how changing i_L affects the concentration polarization curve.

Figure 5 shows the combined polarization curve of activation and concentration polarization. The total polarization is the sum of the two contributions as

$$\eta_t = \eta_a + \eta_c$$

During anodic dissolution, concentration polarization is not a factor as mentioned already, and the equation for the kinetics is given by:

$$\eta_{diss} = \beta\ \log(i/i_o)$$

During reduction processes such as hydrogen evolution or oxygen reduction, concentration polarization is important. The kinetics for a reduction process is given by:

$$\eta_{red} = -\beta\ \log(i/i_o) + (2.3\ RT/nF)\ \log(1-i/i_L)$$

The importance of the two equations above cannot be overemphasized since they are the basic equations of all electrochemical reactions. Using only three basic parameters, namely, β, i_o, and i_L , the kinetics of virtually every corrosion reaction can be precisely described.

Wagner and Traud' made the first formal presentation of the mixed potential theory in 1938. The theory consists of two simple hypotheses:

1. *Any electrochemical reaction can be divided into two or more partial oxidation and reduction reactions.*
2. *There can be no net accumulation of electric charge during an electrochemical reaction.*

From these two hypotheses it follows that *during the corrosion of an electrically isolated metal sample, the total rate of oxidation must equal the total rate of reduction.*

The mixed potential theory, together with the kinetic equations decribed above, constitute the basis of modern electrode kinetics theory.

2.1.3 Mixed Electrodes

A mixed electrode is an electrode or metal sample which is in contact with two or more oxidation-reduction systems. The simplest corrosion system is a metal in contact with a single redox system (e.g. Fe in acid). Actual corrosion

systems are more complicated. Figure 6 shows the behavior of Fe in a carbonate solution which is saturated with oxygen. The E(corr) is determined by applying the basic principles of the mixed potential theory. At steady state, the total rate of oxidation must equal the total rate of reduction. The rates of the individual processes which are occurring in this system are illustrated in Figure 6. At E(corr), the corrosion current density is obtained by the following:

$$i(corr) = i_a = i_c = i_{Fe \rightarrow Fe^{2+}} = i_{H^+ \rightarrow H_2} + i_{O_2 \rightarrow OH^-}$$

The above equation satisfies the charge-conservation principle of the mixed potential theory.

In oxygen-free carbonate solution, i(corr) = H_2 evolution (c.f. i'(corr) in Figure 6). Experimentally, it is usually observed that the rate of hydrogen evolution is substantially decreased by the addition of oxygen to carbonate solutions. This phenomenon has often been termed *depolarization* and is assumed to be the result of interactions between the oxidizing agents and hydrogen gas on the surface. Figure 6 shows that this is not the case; the reduction in hydrogen-evolution rate is the direct result of the shift in corrosion potential and is completely independent of the chemical character of the oxidizing agent.

Some systems are governed by concentration polarization as shown in Figure 7. The corrosion rate of this system is

equal to i(corr) or i_L and, as before, is determined by the intersection between the total reduction rate and total oxidation rate.

2.1.4 Passivity

A loss of chemical reactivity under certain environmental conditions is observed during the corrosion of certain metals and alloys. This loss of chemical reactivity is termed passivity which results in very low corrosion rates; however, the passive film may be unstable and subject to damage. The passive state may be used to reduce corrosion, but caution must be observed.

Experiments indicate that passivity is the result of a surface film that is estimated to be 3 nm or less in thickness. The film is extremely delicate and subject to changes when removed from a metal surface or when the metal is removed from the corrosive environment.

Figure 8 schematically illustrates the typical behavior of an active-passive metal. One of the important characteristics of an active-passive metal is the position of its anodic current density maximum characterized by the primary passivation potential (E(pp)) and the critical anodic current density for passivity (i(c)). The protective film begins to form just above E(pp). The transpassive region is apparently due to the destruction of the passive film at very high potentials. The region above E(pp) where the current density drops off can be termed the "upper

slope" region, and similarly the region below E(pp) can be termed the "lower slope" region.

An increase in temperature increases i(c) substantially and also increases E(pp) and i(p) to a lesser degree.

When considering mixed electrodes involving an active-passive metal, the peculiar S-shaped anodic polarization curves of these metals often leads to unusual results. Figure 9 illustrates three possible cases which may occur when an active-passive metal is exposed to a corrosive environment. Figure 9 shows a single reduction process such as hydrogen evolution with three possible exchange current densities. In case 1 there is one stable intersection point, point A, which is in the active region, and a high corrosion rate is observed. Case 2 is particularly interesting since there are three possible intersection points at which the total rate of oxidation and total rate of reduction are equal. These points are B, C, and D. Although all three meet the basic requirements of the mixed-potential theory, point C is electrically unstable and, as a consequence, the system cannot exist at this point. However, both points B and D are stable. This system may exist in either the active or passive state. The unusual transition of iron in dilute nitric acid, upon scratching the surface, is due to a passive-to-active transition (point D to point B).

In case 3 there is only one stable point, point E, in the passive region. This system cannot be made active and always exhibits a very low corrosion rate. From an

engineering standpoint, case 3 is the most desirable. This system will spontaneously passivate and corrode very slowly.

The position of the current maximum or "nose" of the anodic polarization curve is important. Spontaneous passivation only occurs if the cathodic reduction process clears the tip of the nose of the anodic dissolution curve as shown in case 3. Knowledge of the anodic dissolution behavior of a metal or alloy can be used to quantitatively determine its ease of passivation and ultimately its corrosion resistance.

2.1.5 Electrochemical Corrosion-Rate Measurements

Methods for calculating corrosion rates from polarization measurements have been devised. These include: Tafel extrapolation, linear polarization, three-point, and two-point methods. All the methods are based on the mixed potential theory. The Tafel extrapolation method and the three-point method will be discussed after an introduction to polarization measurements.

2.1.5.1 Polarization measurements

A schematic diagram for conducting polarization measurements is shown in Figure 10. The metal sample is termed the working electrode and current is supplied to it or drawn from it by means of an auxiliary (counter) electrode composed of some inert material such as platinum. Current is measured by means of an ammeter A, and the potential of the working electrode is measured with respect

to a reference electrode by a potentiometer-electrometer circuit. In practice, current is increased by reducing the value of the variable resistance R; the potential and current at various settings are simultaneously measured. It is important to note that Figure 10 is schematic and that polarization measurements cannot be conducted in the simple fashion shown here. Many precautions are required, and the actual experimental arrangement is much more complex than indicated.

Figure 11 shows an applied current cathodic polarization curve of a corroding metal. Applied cathodic current is equal to the difference between the current corresponding to the reduction process and that corresponding to the oxidation or dissolution process.

2.1.5.2 Tafel extrapolation method

In practice, an applied polarization curve becomes linear on a semilogarithmic plot at approximately 50 mV more active or more noble than the corrosion potential. This region of linearity is termed the Tafel region. To determine the corrosion rate from such polarization measurements, the Tafel region is extrapolated to the corrosion potential.

To ensure reasonable accuracy, the Tafel region must extend over a current range of at least one order of magnitude. In many systems this cannot be achieved because of interference from concentration polarization and other extraneous effects. Also, the method can only be applied to systems containing one reduction process, since the Tafel

region is usually distorted if more than one reduction process occurs.

2.1.5.3 Three-point method

Wagner and Traud' developed in 1938 a general rate equation describing electrochemical kinetics of corrosion. A useful, dimensionless form of the general rate equation, used by Barnartt', is

$$i/i(corr) = \pm\{\exp(2.3\Delta E/\beta_a) - \exp(2.3\Delta E/\beta_c)\}$$

where i(corr) is the corrosion current (at the corrosion potential), β_a and β_c are the Tafel slopes for the anodic and cathodic reactions, and $\Delta E = E - E(corr)$. The plus sign in front of the braces refers to anodic polarization, the negative sign to cathodic polarization.

The three-point method developed by Barnartt' in 1970 makes use of current measurements at three interrelated potentials, two anodic and one cathodic (or vice versa), such as ΔE, $2\Delta E$, and $-2\Delta E$. A quadratic method is used. The experimental data are combined into a single quadratic equation, the two roots of which yield numerical values of β_a, β_c, and i(corr).

In analyzing the experimental data, two ratios are formed:

$$r_1 = i(2\Delta E)/i(-2\Delta E)$$

$$r_2 = i(2\Delta E)/i(\Delta E)$$

These ratios are interrelated through the quadratic equation

$$u^2 - r_2 u + \sqrt{r_1} = 0$$

the two roots of which are

$$\exp(2.3\Delta E/\beta_c) \text{ and}$$

$$\exp(2.3\Delta E/\beta_a)$$

the larger and smaller roots respectively. When the Tafel slopes are known, any one of the three (i,E) data points is substituted into the general rate equation to obtain the corrosion current.

A new three-point method has been published by Barnartt and Donaldson[8] in 1983. It permits either cathodic polarization measurements only or anodic only. Restriction to cathodic measurements only is useful where anodic current causes surface etching. The new method is a direct search analysis of the general type described by Hooke and Jeeves.[9] It operates on three equations obtained from the general rate equation by inserting numerical values of current densities i_1, i_2, and i_3 measured at potential changes ΔE_1, ΔE_2, and ΔE_3, respectively. These nonlinear relations can be

solved by a minimization procedure described by Barnartt and Donaldson. First they are combined to yield a function equal to zero for the correct values of β_a, β_c, and i(corr). Starting with initial estimates of these three "unknowns", the minimization routine is applied by computer to change the unknowns by increments and gradually bring the function as close to zero as desired.

2.2 Stress Corrosion Cracking

A good definition of stress corrosion cracking (SCC) formulated by the American Society for Testing of Materials (ASTM) is as follows:

A cracking process requiring the simultaneous action of a corrodent and sustained tensile stress.

This definition leaves out hydrogen embrittlement because corrosion must occur. It also leaves out corrosion fatigue since a sustained tensile stress is required.

During SCC, the metal or alloy is virtually unattacked over most of its surface, while fine cracks progress through it. This cracking phenomenon has serious consequences since it can occur at stresses within the range of typical design stresses. There are usually specific environments in which certain metals or alloys crack. The number of different environments in which a given alloy will crack is generally small. Table 1 shows some environments that may cause SCC of ordinary steels.

2.2.1 Factors Affecting SCC

The important variables affecting SCC are temperature, solution composition, metal composition, stress, and metal structure.

Stress corrosion cracks appear as a brittle mechanical fracture while, in fact, they are the result of local corrosion processes. Both intergranular and transgranular SCC are observed. Both modes of cracking often occur in the

same alloy, depending on the environment or the metal structure.

Cracking generally proceeds perpendicular to the applied stress. Some cracks branch out like a river delta while others are virtually unbranched. The amount of branching is dependent on the metal structure and composition as well as the environment composition.

The applied tensile stress may be due to any source: applied, residual, thermal, or welding. Even corrosion products have been shown to be a source of stress.

As is the case with most chemical reactions, SCC is accelerated by increasing temperature. Most alloys susceptible to cracking will begin cracking at least as low as 100°C.

The susceptibility to SCC is affected by the average chemical composition, preferential orientation of grains, composition and distribution of precipitates, dislocation interactions, and progress of a phase transformation (or the degree of metastability). These factors interact with environmental composition and stress to affect the time to cracking.

2.2.2 Mechanism of SCC

Although SCC is one of the most important corrosion problems, the mechanisms are not well understood. The main reason is the complex interaction between the metal, the interface, and the environment. Also, it is unlikely that a

specific mechanism will be found which applies to all metal-environment systems.

Corrosion plays an important part in the initiation of cracks. A pit or trench on the surface of the metal acts as a stress raiser and it has been observed that cracks do initiate at the base of pits. Once the crack has started, the tip of the crack has a small radius and the stress concentration is high.

Crack propagation has been stopped in some cases when the corrosion was stopped by application of cathodic protection. When corrosion began again the crack continued to propagate.

Plastic deformation at the crack tip can enhance the crack propagation. The plastic deformation may cause the metal at the crack tip to be more active and thereby increase the dissolution of the metal and propagation of the crack.

Plastic deformation may also cause a phase transformation to occur (austenite to martensite in the nickel stainless steels). The newly formed phase may be more susceptible than the parent metal to SCC in the specific environment.

The role of tensile stress has been shown to be important in rupturing films during both initiation and propagation of cracks. The films could be tarnish films (brasses), thin oxide films, or other passive films. Breaks in the passive film allow more rapid corrosion at various

points on the surface and thereby initiate cracks. Breaking of the film at the crack tip would be irreparable, and propagation would continue. Continuous rapid local dissolution is required for rapid propagation.

For intergranular cracking to occur the grain boundaries are attacked preferentially. The grain boundaries could be more anodic because of precipitated phases, depletion, enrichment, or adsorption, thus providing a susceptible path for the crack.

2.2.3 Methods of Prevention

Stress corrosion cracking may be reduced or prevented by application of one or more of the following methods:

a. Lowering the stress below the threshold value if one exists.
b. Eliminating the critical environmental species.
c. Changing the alloy if the stress and environment cannot be changed.
d. Applying cathodic protection, although care must be taken that hydrogen embrittlement does not occur.
e. Adding inhibitors to the system if feasible.

2.2.4 Test Methods and Interpretation of Test Data

In most laboratory corrosion experiments an attempt is made to obtain data in a relatively short time, usually by increasing the severity of the test. In stress corrosion

testing, this has been done by increasing the relative aggressiveness of the environment by altering its composition, temperature or pressure; by stimulating the corrosion reactions galvanostatically or potentiostatically; by increasing the relative susceptibility of the alloy to cracking through changes in structure or composition; or by introducing a notch or precrack into the specimen.

There are three fundamentally different types of specimens and tests. One employs an essentially smooth specimen under static load, the second uses a precracked specimen (also called a fracture mechanics specimen) also under static load, and the third employs a smooth specimen under a rising load with a constant strain rate. The latter will be discussed in some detail.

2.2.4.1 Smooth specimen - constant strain rate test

The constant strain rate test is basically a slow tensile test in an environment.[10] The application of slow dynamic strain assists in stress corrosion crack initiation and has the advantage that the test is not terminated after some arbitrary time, since the conclusion is always achieved by the specimen fracturing. The criterion of cracking susceptibility is then related to the mode of fracture. The slow strain rate test will usually result in failure in not more than a few days, either by ductile fracture or by SCC. Metallographic and other parameters then may be used in assessing the cracking response. The test concludes in a positive manner and therefore is attractive.

The choice of strain rate is critical since the same strain rate does not produce the same response in all systems. If the strain rate is too high, the necessary corrosion reactions for SCC do not have time to occur. If the strain rate is too low, the cracks that do initiate can corrode out and blunt, thereby discontinuing the propagation of the crack. For many systems it has been found that a tensile strain rate in the region of 10^{-5} to 10^{-6} s^{-1} will promote SCC, but the absence of cracking in tests conducted at such rates cannot be taken as an indication of immunity to cracking for a given system until tests have also been conducted at faster and slower strain rates.

The method of assessing the results where SCC is observed can be by a variety of parameters. The effects of SCC are reflected in the load-deflection curve that may be recorded during a constant strain rate test. A comparison of the load-deflection curves for specimens with and without SCC will usually reveal significant differences.

Metallography or fractography is essential to confirm the presence or absence of SCC. Unambiguous evidence indicating SCC susceptibility includes loss of ductility, crack propagation by brittle mode, and numerous secondary cracks along the gagelength perpendicular to the applied stress.

A parameter (elongation, time to failure, ultimate load, or energy absorption) is needed to express SCC severity quantitatively. See Figure 12 which illustrates SCC

parameters on a load-elongation curve. SCC severity is expressed as the ratio of a parameter from the SCC test to the same parameter from a slow strain rate test in an inert environment such as air or oil. A ratio of one indicates no susceptibility and lower ratios indicate increasing SCC severity. If a number of alloys are tested in the same environment the least susceptible or one that is not susceptible would be used.

Finally, the slow strain rate technique is of a conservative nature in that alloys exhibiting SCC in the test can be acceptable in service if stresses are controlled.

3. Literature Survey

3.1 SCC of Steels in Carbonate-Bicarbonate Solutions

3.1.1 SCC of Buried Pipelines

SCC from an external environment has been recognized since 1965 as a possible cause of failures in buried pipelines.[11-14] Such failures have arisen from multiple cracks that are branched, intergranular and usually parallel to the axis of the pipe. Black deposits of magnetite (Fe_3O_4), which sometimes contain iron carbonate ($FeCO_3$), can be observed on the surface of the cracks.

Slightly alkaline water solutions containing primarily sodium carbonate (Na_2CO_3) and sodium bicarbonate ($NaHCO_3$) have been found in voids between the coating and the pipe in the immediate vicinity of stress corrosion cracks. Table 2 lists the compositions of the solutions near the cracks. It is believed that the sodium carbonate and sodium bicarbonate were formed when carbon dioxide from the soil reacted with the hydroxyl ions that were produced at the pipe by the action of the cathodic-protection currents. The reactions involved are as follows:

$$CO_2 + OH^- \rightarrow HCO_3^-$$

$$HCO_3^- + OH^- \rightarrow CO_3^{2-} + H_2O$$

It has been shown that the severity of cracking increases with the concentration of the solution; the lowest concentrations that will produce cracking to a significant extent are in the range of 0.1 to 0.25 N.[1] Cracking has been observed over a wide range of solution compositions in which the ratio of carbonate to bicarbonate has varied from 0 to at least 7.[1,3]

The carbonate-bicarbonate environment that is capable of causing SCC can be produced in a wide variety of geological conditions. In the U.S. stress corrosion cracks have been found in pipelines in heavy clay, light sand, rocky soils, and swamps. The pH of the soils has ranged from 4.7 to 8.8.

There are basically 6 factors responsible for SCC in buried pipelines. They are:

1. Stress level.
2. Physical and chemical properties of the metal.
3. Nature of the environment around the pipe.
4. Potential of the metal in its environment.
5. Temperature.
6. Coating system.

Service failures have mostly occurred at stress levels between 60 and 72 % of the pipe's specified minimum yield strength (SMYS). Fluctuating pressure in a pipeline is also known to accelerate the rate of crack growth. Control of pressure can significantly reduce the susceptibilty to SCC.

Virtually all steels used for pipelines are susceptible to SCC in varying degrees. The presence of a mill scale has a significant effect. Shot peening the surface to remove the mill scale results in a compressive state which increases resistance to SCC.

Environments other than carbonates and/or bicarbonates that have been shown to promote SCC in pipelines include chlorides, nitrates, and hydroxides. Inhibitors can be added to the coating and primer to control the environment at the pipe surface.

The potential of the metal in its environment has to be measured as close as possible to where SCC occurs. In most situations this would be at the base of a pinhole in the coating. Measuring of potentials at the pipe surface under field conditions is an active area of research. Tests have indicated that SCC of pipeline steel in a carbonate-bicarbonate environment will occur only within a narrow range of cathodic electrode potentials such as -670 mV to -770 mV vs. a Cu-$CuSO_4$ reference electrode. Interrupted or fluctuating protective currents have been shown to somewhat minimize the possibility of the cathodic potential being in the critical range.

SCC failures have occurred at temperatures ranging between 10 and 57°C, with most being in the 32 to 38°C range. Temperature has been shown to have a major effect on the rate of crack growth. An increase in temperature can cause coating damage, increase the concentration of harmful

chemicals in contact with the pipe, and expand the critical potential range within which cracking will initiate.

An improvement in the resistance of a pipeline to SCC can be expected if the temperature is lowered. The time to failure can be approximately doubled by reducing the temperature 10°C.

SCC usually occurs at a coating defect, that is, where the coating is disbonded. The coating somewhat shields the cathodic protection currents from properly reaching the metal under the disbonded area. This results in a buildup of harmful chemical environments and the development of potentials in the critical range. Proper coating application is essential for reducing the susceptibility to SCC.

Proper control of any of the above six factors could prevent or at least significantly retard SCC of buried pipelines.

3.1.2 SCC of Steel in the Lab

3.1.2.1 Carbon steel

Polarization curves have been determined by Sutcliffe et al.[1] for carbon steel in a 1 N Na_2CO_3 - 1 N $NaHCO_3$ solution at temperatures ranging from 22 to 90°C. Also SCC tests, including constant strain rate tests, were performed at constant potentials selected from the polarization curves. The strain rate used was 10^{-6} s^{-1}. Figure 13 shows two polarization curves at 90°C, one at a fast scan rate of 1000 mV/min, and another at a slow scan rate of 20mV/min.

Superimposed on these curves is a reduction in area versus potential plot. Carbon steel is susceptible to intergranular SCC at potentials in a critical range . Figure 13 shows that the critical range for SCC lies from approximately -750 mV to -600 mV vs. s.c.e. Constant strain rate tests were also performed at temperatures of 22, 50, and 70°C and the results are shown in Figure 14. Note that the critical range lowers in potential and becomes broader as the temperature is increased. Also, as the temperature is increased the reduction in area is decreased, resulting in increased SCC severity. The critical range for intergranular SCC corresponds to where a black, adherent film of Fe_3O_4 and $FeCO_3$ is formed.'' Also, hydrogen embrittlement occurs at potentials more negative than -800 mV vs. s.c.e. (see Figure 13).

The nature of the surface attack on polished specimens during the early stages of exposure at different potentials in the carbonate-bicarbonate solution was observed. At -675 mV vs. s.c.e., close to the potential for maximum susceptibility to intergranular SCC at 90°C, corrosion attack after 2 min was observed to be structurally dependent resulting in grain boundary grooving. At -750 mV vs. s.c.e. and 90°C, a strong contrast between grains with considerable pitting was observed after 2 min. At -850 mV vs. s.c.e., the rate of attack was reduced and pitting almost absent, as compared with the effects observed at -750 mV vs. s.c.e.

The rates of current decay in the critical range are intermediate between those of more positive potentials (in the passive region) and more negative potentials (anodic peak region). Current decays in the passive region to a steady value in a few seconds, whereas, current decays in the anodic peak region above the primary passivation potential to a steady value after hours. Considering current decay and microstructural attack it is evident that the conditions for intergranular cracking involve a rather fine balance between the dissolution and passivation characteristics of the steel in the environment.[18-23]

A procedure for assessing SCC in a particular environment was presented as follows.[1]

1. Obtain, by stepping or continuous sweeping in the negative to positive direction, and at a fast rate (e.g., 1000 mV/min), the potentiodynamic polarization curve.
2. If an anodic peak is exhibited, repeat the experiment at a slower rate of sweeping (e.g, 20 mV/min) or make measurements of the current decay in the region of the anodic peak.
3. If marked current decay occurs in part of the active peak range, or if the slow potentiodynamic polarization curve shows much lower currents in the peak region, briefly expose metallographically polished specimens at various potentials in the region of current decay, to determine whether or

not the corrosion shows structure dependence.

4. If structural dependent attack is observed, in the form of some trenching in or alongside the grain boundary network such that the surface remains largely unattacked away from the grain boundaries, carry out an appropriate stress corrosion test at the relevant potentials.

3.1.2.2 Pipeline steel

SCC of pipeline steel in carbonate-bicarbonate environments is very similar to SCC of other carbon steel. A critical potential range in which SCC occurs has been reported in the literature.[2,3] Figure 15 is a graph of potential versus pH showing the pH dependence of the intergranular SCC range for pipeline steel in various carbonate-bicarbonate solutions at 75°C.

3.2 High-Strength Low-Alloy (HSLA) Steels

Low-alloy steels have undergone some developments of significant importance that have led to high strength products. Their development has provided structural steels which have yield strengths of greater than 70 ksi (500 MPa).

3.2.1 HSLA Pipeline Steels

One of the most important applications of HSLA steels is for pipeline use in transporting oil and gas. To increase the capacity of pipelines by using higher operating pressures, heavier walled and larger diameter pipes are used which has resulted in more demanding property requirements of the steel.[33] These demands include higher strength and toughness especially if the pipeline is in the arctic or offshore. The weldability and the resistance to environmental attack must not be sacrificed for improved mechanical properties.

Strengthening mechanisms currently used in HSLA steels are solid solution strengthening, dislocation substructure, precipitation hardening, and grain refinement. Consideration of weldability puts an upper limit on carbon and alloying elements because of their influence on the transformation products during cooling. Solid solution strengthening (except Mn, Ni, and possibly Mo), dislocation substructure, and precipitation hardening increase strength at the expense of toughness. Only grain refinement improves both strength and toughness.

The most useful classification of HSLA steels is based on microstructure, because the properties of engineering materials are, in general, determined by microstructure.

There are three main types of HSLA pipeline steels, namely,

1. conventional ferrite-pearlite steels,
2. bainite/acicular ferrite steels, and
3. newly developed multiphase steels (dual-phase steels included).

Controlled rolling is essential for obtaining steels with high strength and good toughness since grain refinement must occur. Regardless of the types of structure, controlled-rolling appears to be vital in producing steels with optimum properties. The controlled-rolling process is often divided into three stages: deformation in the austenite recrystallization temperature region, deformation in the austenite non-recrystallization region, and deformation in the two-phase austenite-ferrite region. Optimum properties of HSLA steels can be obtained only by careful control of microstructural changes in each stage of controlled rolling. The principal variables are deformation temperature and amount of deformation.

3.2.1.1 Ferrite-pearlite steel

Ferrite-pearlite steels obtain their strength mainly from grain refinement and precipitation hardening. Additional strength can be obtained by deformation in the two-phase region. The steels contain vanadium and niobium as

single alloying elements or in combination. The major role of these elements is to refine the ferrite grain size, but they have the additional important function of increasing strength of ferrite-pearlite steel by precipitation hardening.

3.2.1.2 Bainite/acicular ferrite steel

Bainite is a structure composed of ferrite and carbide which is formed when steel is rapidly cooled to and held at temperatures just above the M_s temperature. To obtain upper bainite, higher temperatures are used ($\simeq$550°C) compared to lower temperatures ($\simeq$350°C) which are used to obtain lower bainite. Bainite is characterized by its carbide distribution. In upper bainite, carbides precipitate between the ferrite laths, while in lower bainite, carbides are finely distributed. Acicular ferrite is a highly substructured, non-equiaxed ferrite that forms in continuous cooling by a mixed diffusion and shear mode of transformation that begins at a temperature slightly higher than the upper bainite transformation temperature range.

Bainite/acicular ferrite steels have quite a good combination of strength and toughness due to a high dislocation density and fine effective grain size. In addition to the high strength and good toughness, these steels have the advantage of continuous yielding which is a consequence of the high density of mobile dislocations present in the ferrite lath. Development of high-strength bainite structures enables the carbon content of steel to be

lowered to ultra-low levels (0.02 % C), allowing for improved weldability and high impact energy.

3.2.1.3 Multiphase steel

Multiphase steels consist of a polygonal ferrite matrix with dispersions of second-phase particles. The second phase can be acicular ferrite, bainite, martensite, or combinations of these, depending on alloy compositions and processing variables. Multiphase steels are essentially similar metallurgically to dual-phase steels developed for sheet applications[24], although the former are produced by controlled rolling, while the latter are produced mainly by intercritical annealing. The strength of multiphase steel is generally determined by the volume fraction and type of second phase. Transformation of austenite to strong second phases introduces a high density of mobile dislocations in the surrounding polygonal ferrite matrix, which allows the steel to be deformed at low stresses with continuous yielding. In addition, the multiphase steels generally have higher initial work hardening rates than ferrite-pearlite and bainite/acicular ferrite steels. This causes the multiphase steel to have a high yield strength, approaching ultimate tensile strength, after pipe forming.

In multiphase steels, sufficient alloying additions and/or the application of accelerated cooling after rolling are necessary to introduce a strong second phase in place of pearlite in the ferrite matrix. Correlation of mechanical properties with microstructure is difficult because of the

complexity of structural features (volume fraction, type, and distribution of second phase). However, some general conclusions can be made. It has been observed that the amount of the second phase should be above 4 % to ensure a continuous yielding stress-strain curve, although the type of second phase is also important in that martensite gives a stronger effect than bainite. Size and distribution of the second phase depends upon the severity of controlled rolling in the second stage (austenite non-recrystallization region).

The development of improving the strength in ferrite-pearlite steels has probably reached a limit. While several bainite/acicular ferrite steels are available with promising properties, multiphase steels appear to be most promising for future development since they possess the advantages of both ferrite-pearlite steels and bainite/acicular ferrite steels. They have high toughness due to their fine polygonal ferrite matrix while the strong second phase gives high strength. However, they may have some limitations in applications, especially for sour gas and oil services, because of the well-known susceptibility of martensitic and bainitic steels to hydrogen-induced cracking and stress corrosion cracking. While there is limited evidence that the strong second phases, when embedded in a ferrite matrix, are not preferential sites for crack nucleation, the effect of second phase on the environmental degradation should be well understood before application of multiphase steels to

potentially aggressive environments.

3.2.2 Dual-Phase Steel

As mentioned already, dual-phase steels[24] are a new class of HSLA steels characterized by a microstructure consisting of a dispersion of about 20 % hard martensite particles in a soft, ductile ferrite matrix. The term "dual-phase" refers to the presence of essentially two phases, ferrite and martensite, in the microstructure, although small amounts of bainite, pearlite, and retained austenite may also be present. These steels have a number of unique properties which include:

1. continuous yielding behavior (no yield point),
2. a low 0.2 % offset yield strength (≈50 ksi; 344 MPa),
3. a high tensile strength (≈100 ksi; 690 MPa),
4. a high work-hardening rate, and
5. unusually high uniform and total elongation.

The high work-hardening rate results in a yield strength of 80 ksi (552 MPa) after only 3 to 5 % deformation. As a result, in formed parts dual-phase steels have a yield strength comparable to that of other 80 ksi (552 MPa) HSLA steels. More importantly, the high work-hardening rate, combined with the high uniform elongation of these steels, gives them a formability equivalent to that of much lower strength sheet steels (see Figure 16). As a result these steels are an attractive material for weight-saving applications in automobiles.[25]

3.2.2.1 Production of dual-phase steel

Dual-phase steels are produced either by an intercritical anneal followed by a quench[24] or by controlled rolling[27] as mentioned earlier under multiphase steels.

Dual-phase sheet steels can be produced by intercritical heat treatment with either continuous annealing or box annealing techniques.

In the continuous annealing technique, the steel sheet is heated for a short time (≈2 min) into the intercritical temperature range (two-phase region) to form ferrite-austenite mixtures, followed by accelerated cooling (≈10°C/s) to transform the austenite phase into martensite. The actual cooling rate is dependent on sheet thickness and the quenching conditions on a given annealing line. As a result, steel compositions must be adjusted to obtain the hardenability needed for the cooling rate (sheet thickness). For hot-rolled grades (thickness greater than 0.178 cm) and for thinner, cold-rolled grades typical compositions are given in Table 3.

In the box annealing technique, a similar heat treatment is performed, but the annealing times are much longer (≈3 h) and the cooling rates are much slower (≈20°C/h). Because of the slow cooling rate, much higher alloy steels are required to achieve the desired hardenability. See Table 3 for a typical composition.

Dual-phase steels have been produced in the as-rolled condition by carefully controlling the continuous cooling

transformation characteristics of the steel. This generally requires the addition of substantial amounts of Si, Cr, and Mo in addition to about 1.0 wt % Mn. A typical as-rolled dual-phase steel composition is given in Table 3.

A desired type of continuous cooling transformation is shown in Figure 17. Additions of molybdenum have been found to be particularly beneficial in suppressing the pearlite transformation without preventing the formation of polygonal ferrite during cooling, over a wide range of cooling rates. Silicon and chromium have also been found to be beneficial because Si accelerates the polygonal ferrite reaction, and because Si and Cr both increase the hardenability of the remaining austenite. Most as-rolled dual-phase steels therefore contain appreciable amounts of these alloying elements.

Production of the as-rolled dual-phase steels has the obvious advantage of saving energy costs by eliminating a heat treatment step. However, these steels have a higher alloy cost and more variability in properties.

3.2.2.2 Structure-property relationships

Structure-property relationships in dual-phase steels have been extensively studied. In particular, the effect of the volume fraction martensite, the carbon content of the martensite, the grain size of the ferrite, and the solute content of the ferrite on the yield and tensile strength are well documented. The ductility of dual-phase steels is less understood because it is influenced not only by the above

factors but also by carbon content of the ferrite, amount of retained austenite, and the amount of epitaxial ferrite.

As the amount of martensite phase is increased, both the yield and tensile strength are increased.[28] Similarly, if the carbon content in the martensite phase is increased the yield and tensile strengths increase. As expected, the strength increases as the ferrite grain size decreases.[29] Also, additions of strong solid solution strengthening elements such as Si and P increase the strength of dual-phase steels.[28]

Uniform and total elongation decrease as the percentage of martensite is increased and also when the carbon content (strength) of the martensite is increased.[28] Distribution of the martensite phase must also influence ductility, but very few studies of this variable have been reported.[31] A set of widely spaced, small martensite particles is desired. Chains of martensite particles that are linked up may be detrimental to ductility because this may offer an easy crack propagation path through the matrix.

Solid solution strengthening by addition of Si results in increased ductility.[28] The exact explanation for the Si effect is not known but it has been suggested that it arises from a lowering of the carbon content of the ferrite phase.[32] Lowering of the carbon content of the ferrite phase by decreasing the cooling rate after continuous annealing has been reported to be critical in obtaining the highest possible ductility in dual-phase steels.[33]

The amount of epitaxial ("new") ferrite formed upon cooling has an important effect on ductility, the ductility improving as the amount of epitaxial ferrite is increased.[34] The transformation of retained austenite (if present) during plastic straining and the resultant increase in work-hardening rate has also been used to explain the higher ductility of dual-phase steels.[35,36]

3.2.2.3 Uses

The use of dual-phase steel has been mainly restricted to the automotive industry where weight-saving applications have been made. The high strength associated with excellent formability is useful for forming automotive parts such as wheel rims and brackets.

3.3 Environmental Attack of Dual-Phase Steel

Hydrogen embrittlement of two dual-phase steels with tensile strengths of about 100 ksi (690 MPa) has been reported by Davies.[37] The steels were cathodically charged in a 4 % H_2SO_4 solution containing a small amount of arsenic trioxide and pulled in tension at 0.1 in/min (0.254 cm/min) until failure. Both standard tensile specimens and double-notched specimens were used.

Hydrogen embrittlement resulted in a reduction in fracture strength, although no pre-yield failures were observed, and a change in fracture mode from ductile dimpling to transgranular cleavage. It was concluded that the presence of the 15 to 20 % high-carbon (0.6 % C) high-strength martensite in the dual-phase steels was responsible for the hydrogen embrittlement. The cleavage crack was probably initiated in the high strength martensite or at the martensite-ferrite interface, and then was able to propagate through the softer ferrite.

The initiation of a crack in hydrogen charged dual-phase steel appears to require the expenditure of a large amount of work. Under no conditions was fracture observed unless there had been considerable macroscopic deformation.

SCC susceptibility of a dual-phase steel in 3 1/2 wt % NaCl solution of varying pH was investigated by Pierce[38] and Stiksma.[39] The steel was tested in the as-received, 5 % cold worked, and welded conditions. SCC susceptibility was shown

to increase with a decrease in pH due to hydrogen embrittlement. Failure occurred after a crack propagated through the material and cracks did not initiate until after considerable deformation occurred (c.f. Davies[37]).

4. Materials and Solutions

4.1 Dual-Phase Steel

The dual-phase steel used in this research was provided by Dofasco Steel Company. Five sheets of steel (0.188 in x 12 in x 12 in; 0.478 cm x 30.48 cm x 30.48 cm) were supplied as well as a list of the composition and mechanical properties (see Table 4).

It is a low-carbon, low-alloy steel with high strength and good ductility. Significant alloy additions include Mn, Si, Cr, and Mo. The reasons for Si and Cr additions have already been mentioned in Chapter 3.

4.2 X-65 Steel

A pipeline steel was tested for comparison with the dual-phase steel. The composition and mechanical properties of the Grade X-65 steel, which must have a specified minimum yield strength of 65 ksi (448 MPa), are given in Table 5.

The steel is a low-carbon, low-alloy ferrite-pearlite steel. A significant amount of niobium (Nb) and some vanadium (V) has been added to the steel for grain refinement and for precipitation of carbides to improve the strength.

The steel received a rare earth treatment (Ce) for sulphide shape control. Test specimens of the steel were obtained from a flattened portion of welded pipe and therefore some residual stresses were most likely present.

The wall thickness of the pipe was 5/16 in (0.794 cm).

4.3 Test Solution

A 0.5 M sodium carbonate - 0.5 M sodium bicarbonate solution was used as the corrosive test solution. It is composed of 0.5 moles of sodium carbonate (Na_2CO_3) and 0.5 moles of sodium bicarbonate ($NaHCO_3$) both in one litre of triple distilled water, i.e., the solution is a 1 N Na_2CO_3 - 0.5 N $NaHCO_3$ solution. The chemicals were laboratory grade. The triple distilled water was obtained from the Department of Zoology on the University of Alberta campus. The mainline de-ionized water was passed through four purification columns resulting in a very pure water with a resistivity of 18 Megohm-cm.

The pH of the test solution was 9.5 which is dependent on the amount of HCO_3^- and CO_3^{2-} ions in solution.

4.4 Inert Oil Medium

A Fisherbrand Mechanical Pump Fluid was used as the inert oil medium for tests done at temperatures other than room temperature. The fluid had a low vapor pressure so that at high temperatures it would not vaporize enough to cause experimental problems.

5. Experimental Procedure

5.1 Microscopic Examination of the Steels

5.1.1 Dual-Phase Steel

To observe the microstructure of the dual-phase steel an etching technique developed for dual-phase steel to discriminate between martensite and ferrite was used.[40] The etchant was composed of two solutions in a 1:1 volume ratio. One solution was 1% sodium metabisulfite in distilled water and the other was 4% picric acid in ethyl alcohol (4% picral).

The etching procedure was as follows.

a. The steel was mounted in bakelite, wet ground with 600 grit SiC paper, and dried with ethyl alcohol and a hot air blower.

b. The steel was then rough polished with 6 micron diamond paste and Buehler Metadi Fluid on nylon, washed with soap, rinsed with water, and dried.

c. The steel was preliminarily etched with the 4% picral solution for 6-8 s, rinsed, and dried.

d. The steel was polished with 0.3 micron alpha-alumina and water on cloth, washed with soap, rinsed, and dried.

e. The steel was final polished with 0.05 micron gamma-alumina and water on cloth, washed with soap, rinsed, and dried.

f. The 1:1 volume ratio of the solutions was prepared.

g. The steel was immersed in the etchant for 15-20 s, rinsed with ethyl alcohol, and dried.

5.1.2 X-65 Steel

To observe the microstructure of the X-65 steel the following etching technique involving 2% nital (2% nitric acid in ethyl alcohol) was used.

a. The steel was mounted in bakelite, wet ground with 600 grit SiC paper, and dried with ethyl alcohol and a hot air blower.

b. The steel was then rough polished with 6 micron diamond paste and Buehler Metadi Fluid on nylon, washed with soap, rinsed with water, and dried.

c. The steel was polished with 0.3 micron alpha-alumina and water on cloth, washed with soap, rinsed, and dried.

d. The steel was final polished with 0.05 micron gamma-alumina and water on cloth, washed, rinsed, and dried.

e. The steel was immersed in 2% nital for 5-10 s, rinsed, and dried.

5.1.3 Examination with the Microscope

The steel microstructures were observed under a metallurgical microscope (Carl Zeiss, Model No. 67210)

capable of taking photographs with Polaroid and 35 mm film using appropriate attachments. Magnifications of 200X, 400X, and 600X were used. Black and white photographs were taken.

5.2 Polarization Curves

5.2.1 Equipment

The curves were produced with the aid of the following instruments.

a. ECO Model 551 Potentiostat-Galvanostat.
This potentiostat-galvanostat gives a fast response of 0.1 μs with a medium voltage-current product, (33V X 1A). The instrument is capable of measuring the rest potential of the cell when no potential is applied (i.e., when the cell is out).

b. ECO Model 567 Digital Function Generator.
This instrument has been designed to be used as a driver for the potentiostat. It supplies waveforms to carry out all the modern electrochemical techniques involving linear scanning with or without delay. A simple ramp waveform of potential with time was used in the research.

c. ECO Model 560/LOG Linear/Logarithmic Interface.
This instrument has been designed to interface the ECO potentiostat providing for 23 linear ranges from 0.5 μA up to 10 A, and with 4 logarithmic ranges of 4 decades each with thresholds fixed at 0.1, 1, 10, and 100 μA.
In the research, the polarization curves were plotted in the most accurate logarithmic range of current.

d. Hewlett-Packard Model 7044A X-Y Recorder.

This recorder was used to plot log current on the x-axis and potential on the y-axis. Blue and red pens were used to distinguish between the forward and reverse potential scans.

See Figure 18 for a picture of the equipment used.

5.2.2 Cell Arrangement

The corrosion cell was composed of a working electrode (dual-phase or X-65 steel), a counter electrode (platinum), and a reference electrode (saturated calomel). These electrodes were assembled in a flask which was specifically designed for electrochemical studies. The flask with attachments such as a gas inlet tube and capillary Luggin probe were made by Lab Glass, Inc., Vineland, N.J., U.S.A. A thermometer was also introduced into the flask. See Figure 19 which shows the complete cell arrangement.

A description of each electrode follows.

a. Working Electrode

The working electrode was made by mounting two pieces of steel in bakelite in an arrangement that made it easy to make an electrical connection with the steel without exposing the connection to the environment. See Figures 20 and 21 which show the working electrode assembly.

b. Counter Electrode

The counter electrode was a piece of platinum wire

which was coiled and connected via mercury to a copper wire inside a glass tube assembly (see Figure 22).

c. Reference Electrode

A Fisher Scientific saturated calomel electrode (s.c.e.) was used. (Cat. No. 13-639-52)

Electrode: Hg / Hg_2Cl_2 / KCl (saturated)

Potential: 0.242 V vs. Hydrogen electrode at 25°C

Temperature dependence: $dE/dT = -7.6 \times 10^{-4}$ V/°C

The reference electrode was connected to the corrosion cell via a salt bridge of the capillary Luggin-probe type. The solution in the salt bridge was the same as the test solution (0.5 M Na_2CO_3 and 0.5 M $NaHCO_3$). See Figure 23 which shows the salt bridge assembly.

5.2.3 Temperature Control

A heating mantle was used to heat the solution in the flask for tests at temperatures higher than room temperature. The amount of heat supplied by the mantle was controlled by a Variac which controls the amount of current passing through the mantle. The temperature was monitored by a thermometer to within 0.5°C of the desired temperature

(see Figure 24). Polarization curves were obtained for the following temperatures: Room temperature, 50, 70, and 90°C.

5.2.4 Sample Preparation

The steel mounted in bakelite was wet ground with 600 grit SiC paper and dried with ethyl alcohol and a hot air blower. The preparation of the surface took place within 5 min of the start of the test so that there was minimal oxidation of the steel.

5.2.5 Scanning Procedure

The scanning procedure for producing a polarization curve was as follows.

a. The salt bridge was assembled and connected to the flask. After the solution was added, the reference electrode was placed into the top opening of the salt bridge.

b. The counter electrode was assembled and connected to the flask. The thermometer, the gas inlet tube, and the gas outlet tube were placed in the flask.

c. The test solution was poured into the flask and the leads from the potentiostat were fastened to the electrodes.

d. Nitrogen gas was bubbled through the solution at a rate of approximately 0.5 cm^3/s for 1 h.

e. For runs above room temperature, the heating mantle was brought into contact with the flask and

the solution was heated to the desired temperature.

f. After 1 h of removing oxygen from the solution, the working electrode (which had just been ground) was added to the cell, and the steel surface submerged in the test solution.

g. The steel was immediately set to a potential of -1100 mV vs. s.c.e. (well in the cathodic range) and kept there for 5 min to clean the surface. The flowrate of bubbled nitrogen was reduced to approximately 0.1 cm^3/s.

h. A potential scan from -1100 mV vs. s.c.e. to just above the rest potential, E(corr), was performed at a constant rate of 333 μV/s (20 mV/min). This potential vs. log current portion of the polarization curve was recorded on an expanded potential scale and was used for Tafel extrapolation.

i. Immediately, the potential was reset to -1100 mV vs. s.c.e., the potential scale on the recorder reduced, and the potential increased at a constant rate of 333 μV/s (20 mV/min) through the active and passive regions to the transpassive region.

j. The potential was held in the transpassive region for approximately 10 s to exchange the blue pen for the red pen.

k. The potential scan was reversed. The potential

decreased from the transpassive region to -1100 mV vs. s.c.e. at a constant rate (1 mV/s, 3 mV/s, or 20mV/min).

1. Once the reverse scan was completed, the working electrode assembly was removed from the cell, the bakelite mount detached, and the surface area of the steel measured. The potential - log current curves were then converted to potential - log current density curves.

In one test run of dual-phase steel at 22°C, a rate of 33 μV/s (≈2 mV/min) was used for a forward potential scan.

In another test run of dual-phase steel at 22°C, air was bubbled through the solution at a rate of 0.1 cm^3/s ensuring oxygen saturation.

5.3 Constant Potential Tests

5.3.1 Equipment

The potentiostat-galvanostat, described earlier, was used to hold the corrosion cell at a constant potential. At a constant potential the current could be read directly from the potentiostat-galvanostat since it has an ammeter attached. No continuous recording of the current was required.

5.3.2 Cell Arrangement

The cell arrangement which was used for producing polarization curves was also used for the constant potential tests.

5.3.3 Temperature Control

For tests at temperatures higher than room temperature, a heating mantle in contact with the flask was used to maintain the temperature within 0.5°C of the test temperature. Refer to the temperature control in the polarization curve section.

5.3.4 Sample Preparation

The polishing technique was the same as for microscopic examination of the X-65 steel except that the sample was unetched. It took place within 5 min of the start of the test so that there was minimal oxidation of the surface.

5.3.5 Test Procedure

The test procedure was as follows.

a. The corrosion cell was assembled (excluding the working electrode) in the same manner as was done for the polarization curve tests. The test solution was poured into the flask and the leads from the potentiostat were fastened to the electrodes. Nitrogen gas was bubbled through the solution at a rate of approximately 0.5 cm^3/s for 1 h. For tests above room temperature, the heating mantle was brought into contact with the flask and the solution was heated to the desired temperature.

b. After 1 h of nitrogen purging, the working electrode, which had just been polished, was added to the cell, and the steel surface submerged in the test solution. The steel was immediately set to a potential of -1100 mV vs. s.c.e. and kept there for 5 min to clean the surface. The flow rate of nitrogen was reduced to 0.1 cm^3/s.

c. After a few seconds the potential was brought to the test potential and held at that potential for a specified time depending on the temperature.
Room temperature: 20 min.
50°C and 70°C: 5 min.
The current was monitored on the potentiostat during the test.

d. Once the test was completed, the working electrode was removed from the cell, rinsed with ethyl alcohol and air dried. The steel surface was examined for corrosion attack with the microscope.

5.3.5.1 Extended rest potential tests

Aerated and de-aerated tests were also performed. The working electrode (dual-phase steel) was polished with 6 micron diamond paste and Buehler Metadi Fluid on nylon, washed with soap, rinsed with water, and dried with ethyl alcohol and a hot air blower.

The working electrode was submerged in the test solution in the corrosion cell with no applied potential. The rest potential was monitored by the potentiostat; 18 h for the de-aerated test and 19 h for the aerated test. Nitrogen or air, depending on the test, was continuously bubbled through the solution at approximately 0.1 cm^3/s. After the test, the corrosion attack was observed under the microscope.

5.3.6 Examination with the Microscope

The Carl Zeiss metallurgical microscope, previously described, was used to observe the corrosion attack of the steels. Magnifications of 200X, 400X, and 600X were used. Polaroid black and white pictures were taken.

5.4 Constant Strain Rate Tests

5.4.1 Specimen Preparation

Since the constant strain rate test used for determining SCC susceptibility is a slow tensile test in a specific environment, a tensile specimen was used. The tensile specimen is the working electrode in the corrosion cell.

The tensile specimen was machined from a plate of steel with the longitudinal direction of the specimen in the direction of rolling. See Figures 25 and 26 for the dimensions of the specimen. The gage length was 0.75 in (1.91 cm), the gage width was 0.5 in (1.27 cm), and the thickness was 0.112 in (0.284 cm).

The tensile specimen was wet ground with 600 grit SiC paper in the reduced section (see Figure 26) prior to the run.

5.4.2 Equipment

The potential on the steel during the constant strain rate test was kept constant by the use of a potentiostat (ECO Model 549 Potentiostat-Galvanostat). This potentiostat differs from Model 551, which was previously described in the Polarization Curve section, in that it cannot measure the rest potential of the cell when the cell has no applied potential. Also, this potentiostat is not as precise as Model 551.

The tensile testing machine used was the Material Test System (see Figure 27).

5.4.2.1 Material Test System

The MTS 810 was used. The system is comprised of a 45.5 L/min, 3000 psi (20.7 MPa) hydraulic supply, a 25 tonne load frame and load cell, and two 100 kN hydraulic grips.

The system was used since it could handle the slow strain rates required for the constant strain rate test. Also, since the crosshead of the load frame is moved hydraulically, the movement is smooth. This is essential for very slow strain rates.

The strain rate was set by moving the crosshead a specified distance in a certain amount of time. Since the strain rate used was 2×10^{-4} s^{-1} and the gage length of the tensile specimen was 0.75 in (1.91 cm), the crosshead was set to move 0.525 in (1.333 cm) in 3.5×10^{3} s, which is referred to as stroke control. No strain gages are required on the tensile specimen which would be awkward in a corrosive environment. The MTS 442 Controller and MTS 410 Digital Function Generator were used to set up the stroke control.

A simple ramp function was set on the function generator. The MTS 430 Digital Indicator was used for instantaneous measurements of the crosshead movement and load. A Heath Built Servo-Recorder (Model EUW - 20A) was used to record the load on the specimen as a function of time. It was used instead of the MTS Recorder since the slow

strain rate tests took over 2 days and an expanded graph was required. The recorder was set at 1 in/h (2.54 cm/h).

5.4.3 Cell Arrangement

The cell was composed of the tensile specimen (working electrode), two 2-in (5.08 cm) lengths of platinum wire (counter electrodes), and a salt bridge which was used in conjunction with the saturated calomel electrode (reference electrode). A plastic container was used to hold the electrodes in the test solution. See Figure 28,29 and 30 for a picture and detailed illustrations of the cell. Two nylon sleeves attached to the tensile specimen were required to allow the specimen to slide freely through the plastic container during straining of the specimen. Central Scientific Company Sealstix Cement was used to ensure no leakage through the bottom nylon sleeve along the tensile specimen (see Figure 31). The cement was allowed to set for 1 h before assembling the cell.

5.4.3.1 Recirculation system

Two litres of test solution were prepared for each test. The solution was pumped by a peristaltic pump from an external reservoir (flask) to the corrosion cell (plastic container) via tubing. A special silicone rubber tubing was required for the peristaltic pump since ordinary Tygon tubing was not able to withstand the cyclic pinching during pumping. The flow rate of the solution through the system was approximately 6 mL/s. The external reservoir was used

for control of the temperature for tests at temperatures greater than room temperature. Also, nitrogen was bubbled through the reservoir to remove the oxygen from the solution. See Figure 32 which shows the recirculation system.

5.4.4 Temperature Control

The cell temperature was monitored by a Chromel-Alumel thermocouple connected to a Fluke digital thermometer. The solution was heated in the external reservoir (flask) with a heating mantle or a hotplate. The temperature of the reservoir solution was monitored by means of a thermometer. The heat input was regulated by the amount of current passing through the heating mantle or hotplate (see Figure 32). The temperature was regulated to within 1°C of the desired temperature. The test temperatures were 22, 50, 70, and 90°C.

5.4.5 Test Procedure

The test procedure for constant strain rate testing was as follows.

a. The tensile specimen was degreased with ethyl alcohol. The reduced section of the tensile specimen was wet ground with 600 grit SiC paper, and dried with ethyl alcohol and a paper towel.
b. The nylon sleeves were attached to the specimen by Sealstix Cement. The cement was allowed to cool

and set for 1 h. Teflon tape was also used so that only the gage of the tensile specimen was exposed.

c. In the meantime the test solution was added to the external reservoir (flask) and nitrogen gas bubbled through the solution at a rate of 0.5 cm^3/s.

d. When the cemented specimen was ready, it was inserted through the plastic container and the corrosion cell was prepared with all the attachments.

e. The cell was mounted in the hydraulic grips of the MTS tensile testing machine. The test solution was then added to the salt bridge and the saturated calomel electrode inserted.

f. The electrodes were then connected to the potentiostat (ECO Model 549).

g. If required, the external reservoir was heated to the test temperature, the circulation was started, and the steel specimen was set to a potential of -1100 mV vs. s.c.e. (well in the cathodic range).

h. Once the temperature was regulated to the desired temperature the potential of the steel was set to the test potential for 5 min.

i. After 5 min, the constant strain rate test was started by moving the crosshead at a specified constant rate. The strain rate was set at $2 \times 10^{-4}\ s^{-1}$ (engineering strain rate). The

recorder began to plot the load on the specimen as a function of time.

j. The specimen was removed when broken and measurements were taken from the specimen. Also, measurements from the graph were obtained.

5.4.5.1 Oil tests

For the constant strain rate tests performed in the oil medium the procedure was slightly different. The cell did not have to be assembled with all the attachments, since no electrochemical reactions take place in oil. The circulation was performed in the same manner as before, except that oil was circulated instead of the carbonate/bicarbonate solution.

5.4.6 Examination with the Microscope

For some of the specimens, the ISI-60 Scanning Electron Microscope (SEM) was used to obtain fractographs of the fracture surface to observe the mode of cracking. An inhibited hydrochloric acid pickling technique was used to remove corrosion debris (oxides) without affecting the fracture surface.[1] The technique allows meaningful evaluations to be made at relatively high magnifications.

6. Results and Discussion

6.1 Microscopic Examination

6.1.1 Dual-Phase Steel

With the special etchant previously described, the microstructure of dual-phase steels can be examined. The microstructure of the Dofasco dual-phase steel is shown in Figure 33. The light areas are martensite and the remainder of the structure is ferrite. The ferrite grain boundaries are beginning to be etched but at longer etching times, which would clearly show the ferrite grains, the light areas begin to disappear.

The amount of martensite is about 15 % and is irregular in shape and non-uniform in size. The islands of martensite do not appear to be aligned in any particular direction but rather are randomly distributed. The strength of dual-phase steels is mainly derived from these islands of martensite, whereas the ductility is mainly provided by the ferrite matrix.

6.1.2 X-65 Steel

2 % nital was used to etch the pipeline steel. The microstructure is shown in Figure 34. The dark areas are pearlite and the matrix is ferrite. There is about 15 % pearlite and the rest is ferrite. The pearlite and ferrite grains are elongated in the direction of rolling. No carbide

precipitation is evident from the micrograph since an electron microscope is needed to see it.

6.2 Polarization Curves

Polarization measurements were made potentiodynamically to produce polarization curves of dual-phase steel and pipeline steel (X-65) in a 0.5 M Na_2CO_3 - 0.5 M $NaHCO_3$ solution at temperatures ranging from room temperature to 90°C.

6.2.1 Dual-Phase Steel

Figure 35 illustrates the polarization of dual-phase steel in the test solution at room temperature (22°C). The dual-phase steel behaves in a typical active-passive manner where a large anodic current subsides to a small passive current as potential is increased. The basic parameters which describe this can be readily obtained from the polarization curve. The corrosion potential, E(corr), is -0.855V vs. s.c.e., the primary passivation potential, E(pp), is -0.670V vs. s.c.e., the critical current density, i(c), is 0.31 mA/cm², and the passive current density, i(p), is 0.0044 mA/cm².

At high potentials, approximately 0.8V vs. s.c.e., the current begins to increase due to oxygen evolution arising from water breakdown according to the following reaction.

$$2H_2O \rightarrow O_2 + 4H^+ + 4e^-$$

A cathodic loop occurs at potentials near -0.45V vs. s.c.e. It is termed a cathodic loop since it is a region of net cathodic current surrounded by regions of net anodic current. Both anodic and cathodic processes are occurring at the same time but since the cathodic current is greater than the anodic current a net cathodic current appears as a cathodic loop. This is due to a small amount of dissolved oxygen which is being reduced and thereby producing a cathodic current.

The cathodic process at low potentials is water decomposition.

$$2H_2O + 2e^- \rightarrow H_2 + 2OH^-$$

For a pH of 9.5 at 22°C, water decomposition begins at a potential of -0.557V vs. the standard hydrogen electrode (s.h.e.), or -0.799V vs. s.c.e.

A reverse scan at the same rate as the forward scan shows that the passive film is very stable. The oxygen evolution line is retraced and the net current drops off to very low values. At a potential between 0.2 and 0.0V vs. s.c.e., the net current becomes cathodic and increases cathodically until a potential of approximately -0.55V vs. s.c.e. The current then decreases cathodically and becomes anodic at a potential of -0.58V vs. s.c.e. An anodic peak is

formed which corresponds to the anodic peak of the forward scan.

Another polarization curve was produced at room temperature at a slower scanning rate of 33 μV/s (≈2mV/min). E(corr) and E(pp) remained the same as well as the critical current density (i(c)). The difference between the two curves is the passive region. At a slower scan the system is allowed to proceed toward equilibrium to a greater extent at a specific potential. This is reflected in the lower passive current density (i(p)) of 0.001 mA/cm² compared to 0.0044 mA/cm² for the faster scan. Also the cathodic loop has a much higher cathodic current density of 0.01 mA/cm² compared to 0.001 mA/cm².

The polarization curves of dual-phase steel in the test solution at temperatures of 50, 70, and 90°C are shown in Figures 36, 37, and 38, respectively. The dual-phase steel continues to display the active-passive behavior with increasing temperature. Although the shape of the curve remains relatively the same, the position of the curve is shifted slightly downward in potential and shifted significantly to higher currents. E(corr), E(pp), and the potential where oxygen evolution occurs are all lowered with increasing temperature. Alternatively, i(c) and i(p) are increased with increasing temperature. Table 6 lists the values for these parameters as a function of temperature.

Comparison of the polarization curves reveals that the cathodic loop is most pronounced at 50°C and is not evident

at 90°C. This could be due to the combined effect of a decreasing amount of oxygen in solution with temperature and an increasing iron dissolution with temperature. This will be investigated further in another section concerned with the effect of aeration.

6.2.2 X-65 Steel

The polarization curves of X-65 steel in the test solution at temperatures of 22, 50, and 90°C are shown in Figures 39, 40, and 41, respectively. The behavior of this pipeline steel is very similar to that of dual-phase steel; however, there are a few differences.

Table 7 lists the values of a number of parameters for the different test temperatures. The curves are shifted down in potential and increased in current as temperature is increased.

There are no cathodic loops present at any of the temperatures. At 50 and 90°C there is a second anodic (oxidation) peak at approximately -0.5V vs. s.c.e.. It has been reported in the literature that secondary oxidation peaks occur when iron is passivated in carbonate solutions.'' The first oxidation peak corresponds to the formation of an oxide film, which is probably magnetite (Fe_3O_4). At the same time a film containing ferrous carbonate ($FeCO_3$) forms on the iron surface. The second oxidation peak corresponds to the ferrous carbonate in the surface film being oxidized to a hydrated ferric oxide

($Fe(OH)_3$).

Also, the passive current significantly decreases as the potential is increased. This could indicate that the film becomes more stable with increasing potential or time since the test is potentiodynamic.

6.2.3 Effect of Aeration

Figure 42 shows the polarization curves of dual-phase steel in aerated and de-aerated test solutions at 22°C. Table 8 lists the values of some parameters obtained from the curves to show the effect of aeration. E(corr) is increased, E(pp) is decreased, and both i(c) and i(p) are decreased when the solution is saturated with oxygen.

Figure 42 shows that the polarization in the aerated solution results in an increased cathodic loop at about -0.45V vs. s.c.e.. To explain this effect some reactions which could occur on steel in carbonate/bicarbonate solutions will be investigated of which some of the data has been obtained from Thomas et al.'' Table 9 lists some of these possible reactions. Thermodynamic calculations have been made for these reactions and the equilibrium potentials (or reversible potentials) for the test conditions have been listed.

Using the thermodynamic as well as the kinetic data, Figure 43 has been devised to illustrate how the amount of oxygen present in the solution affects the corrosion behavior of the steel. An increase in oxygen increases the

equilibrium potential of the oxygen reduction process and also increases the limiting current of oxygen reduction. This results in an increase in cathodic loop current and increases the corrosion potential, E(corr). Also, it will decrease the apparent primary passivation potential, E(pp).

6.2.4 Corrosion Rate Calculations

Since more than one reduction process is occurring at potentials more negative than E(corr), the Tafel extrapolation method for determining the corrosion rate is invalid. No straight line (Tafel region) can be found on the blown-up cathodic polarization curves, and therefore no extrapolation to E(corr) can be made.

The only method available under these circumstances is the three-point or general method. For a specific ΔE (E - E(corr)), three current densities (i(ΔE), i($2\Delta E$), and i($-2\Delta E$)), are used to calculate the corrosion current density, i(corr). See Appendix A for the calculations involved in using the three-point method.

Three ΔE values of -0.02V, -0.03V, and -0.04V, were used in determining the Tafel slopes and corrosion current densities of the dual-phase steel and X-65 steel in the test solutions at different temperatures. The results are tabulated in Tables 10 and 11.

6.2.5 Effect of Temperature

The Arrhenius equation gives the rate of a reaction as a function of temperature.

$$\text{Rate of Reaction} = \text{Constant} \times [\exp(-Q/RT)]$$

where Q is the activation energy, R is the gas constant, and T is the absolute temperature. The equation can be rewritten

$$\ln(\text{Rate of Reaction}) = \text{Constant}' - (Q/R)(1/T)$$

For corrosion processes, the rate of reaction is directly proportional to the current density, i(c), i(p), or i(corr). If log(current density) is plotted against 1/T a straight line of slope -Q/2.303R will be obtained. If the rate controlling process changes at a certain temperature, then two regions (each with its own straight line) will become apparent. Table 12 lists the different current densities as a function of temperature. These data points were plotted on semilogarithmic graphs, and, using linear regression, apparent activation energies were obtained.

Well-correlated straight lines are produced when i(c) and i(p) are plotted (see Figures 44 and 45). The passive current density, i(p), was not used for the X-65 steel since no constant i(p) could be obtained from the polarization curves at 50 and 90°C. Since the apparent activation energies are low, less than 20 kcal/mole, the process is

diffusion-controlled. The rate controlling step is probably diffusion of the reactant, Fe, through the oxide film. At i(c) the diffusion may be through a film of Fe_3O_4 and $FeCO_3$, and at i(p) the diffusion would be through the stable, passive film. Since the passive film is more protective (stable) than the anodic peak film, the diffusion of Fe through it is not as great.

The corrosion current density as obtained by the 3-point method did not produce a straight line (throughout the temperature range) for either the dual-phase steel or the pipeline steel (see Figures 46 and 47). There appears to be a change in the rate-controlling step as the temperature is increased for the dual-phase steel. The reaction is more diffusion-controlled at lower temperatures as indicated by the lower slope (see Figure 46). At lower temperatures the apparent activation energy is approximately 1.84 kcal/mole and at higher temperatures it is significantly increased to approximately 17.7 kcal/mole. This could be due to oxygen reduction having a greater effect at the lower temperatures. The amount of oxygen in solution at higher temperatures is less and therefore the limiting current density, i_L, of oxygen is less, resulting in a non-linear Arrhenius plot.

The plot of log (i(corr)) against the inverse of absolute temperature for the X-65 steel does not show much since a test at 70°C was not done. The effect of ΔE on i(corr) is shown to be very significant as compared to the dual-phase steel.

6.3 Constant Potential Tests

6.3.1 Dual-Phase Steel

The potentials used in the constant potential tests were obtained from the polarization curves. Potentials in the vicinity of the anodic peak, both below and above, were used to investigate the corrosion attack of the dual-phase steel at temperatures of 22, 50, and 70°C during the early stages of exposure. Temperature increased the rate of corrosion but it did not affect the way the structure was attacked. Pictures were taken of the corrosion attack at the three temperatures but only those at 50°C will be shown to illustrate the attack and its dependence on potential.

Figure 48 shows the corrosion attack after one hour at the corrosion potential (-0.870V vs. s.c.e.). There appears to be selective corrosion of some grains as well as some grain boundary etching.

Figure 49 shows the corrosion attack at a potential half-way between the corrosion and primary passivation potentials (-0.800V vs. s.c.e.) after 5 min. The corrosion is quite uniform but some pitting is evident.

A further increase in potential to the primary passivation potential (-0.725V vs. s.c.e.) results in uniform corrosion with some grain boundary etching after 5 min (see Figure 50). The surface has some pitting.

Above the primary passivation potential, corrosion attack becomes very selective. Figures 51 and 52 show the

corrosion attack at potentials in the "upper slope" region (see Figure 8) after 5 min. Martensite is selectively corroded with the ferrite virtually unattacked (note the scratches on the surface from the polishing procedure). The corrosion of the martensite at -0.600V vs. s.c.e. is less severe than at -0.625V vs. s.c.e. for the same amount of time simply because the current is lower.

The selectively corroded regions were investigated to see if they were martensite. First of all, the amount of the corroded area is about the same as the amount of martensite in the steel (≃15%; c.f. Figure 33). Also,the special etchant to discriminate martensite was used to etch the steel after it was corroded in the test solution at a constant potential in the "upper slope" region. The dark corroded spots, with time in the etchant, changed to light (white) spots. The etchant does change martensite to white when used to observe the microstructure of the dual-phase steel[6], and since the dark spots turn white, the selectively corroded regions can be identified as martensite.

Carbon steel has been shown to have grain boundaries etched out at corresponding "upper slope" potentials.[7] The grain boundary etching was shown to occur in the critical potential range in which SCC occurs. The grain boundary attack produced a susceptible path for SCC to occur along.

The selective dissolution of martensite does not produce a susceptible path since the martensite areas in the

steel are not connected. If cracks do form in the martensite phase they would probably blunt when the ductile ferrite phase is reached.

6.3.1.1 Extended rest potential tests

Two tests were performed at room temperature; an aerated test for 19 h and a de-aerated test for 18 h. The rest potential was monitored for both tests.

The potential of the aerated test was approximately -0.425V vs. s.c.e. initially and steadily increased to approximately -0.235V vs. s.c.e. after 19 h. The potential was in the passive region throughout the test (c.f. polarization curve in aerated solution at 22°C), and no corrosion was observed under the microscope.

The potential of the de-aerated test fluctuated from -0.859 to -0.873V vs. s.c.e., near the corrosion potential, E(corr), in the de-aerated solution at 22°C (c.f. polarization curve). Corrosion attack was similar to the corrosion attack after 1 h at -0.870V vs. s.c.e. at 50°C (Figure 48) but to a greater extent. Selective corrosion of some grains was observed with deep grain boundary attack and minimal pitting.

6.3.2 X-65 Steel

Constant potential tests were done on X-65 steel only at a temperature of 50°C. A "lower slope" potential, the primary passivation potential, and an "upper slope" potential were used. These potentials were obtained from the

polarization curve done at 50°C (Figure 40).

Figure 53 shows the corrosion attack at a "lower slope" potential of -0.790V vs. s.c.e. after 5 min. The attack is uniform with minimal pitting. An increase in potential to the primary passivation potential (-0.700V vs. s.c.e.) results in the corrosion attack after 5 min to be relatively uniform with over-etched regions which given more time would result in pits (see Figure 54)

Excessive pitting after 5 min at an "upper slope" potential of -0.675V vs. s.c.e. is shown in Figure 55. The rest of the microstructure is uniformly corroded. Pits are known to initiate stress corrosion cracks and if there is a susceptible microstructure present then the crack will not be slowed or stopped and will propagate through the material.

6.4 Constant Strain Rate Tests

6.4.1 Dual-Phase Steel

A number of constant strain rate tests were conducted at temperatures of 21, 50, and 70°C. The test potentials ranged from well below the corrosion potential through the anodic peak region to potentials in the passive region. The results of these tests are listed in Table 13. The most useful SCC parameters are reduction in area and elongation which both describe the ductility of the material. Since no reduction in area calculations were made, the elongation parameter was used to evaluate SCC susceptibility.

Figure 56 shows percent elongation as a function of potential for the dual-phase steel in the test solution at 21°C. Hydrogen charging at -1.1V vs. s.c.e. results in a reduction in elongation (26.7%) as compared to the elongation achieved in air (43.7%). At the corrosion potential there is also a loss of ductility (34.8% elongation). As the potential is increased further the ductility increases until the maximum ductility available is reached, corresponding to the ductility of the steel in the inert environment (air). Hydrogen charging of steel under these environmental conditions occurs at potentials lower than -0.8V vs.s.c.e. and therefore most likely the reduction in ductility at the lower potentials is due to hydrogen embrittlement.

Figures 57 and 58 show percent elongation as a function of potential at 50 and 70°C, respectively. The same behavior as at room temperature is apparent. The ductility is reduced as the potential is lowered into the hydrogen charging range. This is again due to hydrogen embrittlement and it appears that hydrogen embrittlement is most severe at 50°C for a potential of -1.1V vs. s.c.e.. As at room temperature, for potentials higher than E(corr) the ductility approaches the ductility in the inert environment.

There is no significant drop in ductility as the result of SCC in a critical range above the primary passivation potential as is known to occur in carbon and pipeline steels. This is probably due to the absence of a susceptible path in the microstructure along which cracking can occur. The martensite is selectively corroded in the "upper slope" potential range during initial stages of corrosion and results in a discontinuous corrosion path. Selective corrosion of the martensite phase leaves approximately 85 % of the material unattacked and unsusceptible to SCC. Also, initially the martensite is attacked severely leaving the martensite unsusceptible to SCC since SCC usually does not occur where corrosion rates are high.

Figures 59, 60, and 61 show the elongation parameter (e/e_{inert}) as a function of potential at 21, 50, and 70°C, respectively. These graphs show the susceptibility of the steel to environmental attack with respect to the test done in the inert environment, air or oil. The ratio of the

elongation in the test environment to the elongation in the inert environment is plotted against potential. As the ratio approaches 1, then the susceptibility is virtually nil. The elongations of specimens A, 28, and 29 were used as the elongation of the steel in the inert environment.

6.4.2 Scanning Electron Microscopy

All the dual-phase steel specimens that had a significant loss in ductility were observed under the scanning electron microscope (SEM). Also, the tests done in the inert environments were observed for comparison purposes.

Figure 62 is a picture of specimen 1 which shows a typical ductile failure occurring after considerable necking. Figure 63 is an SEM fractograph showing ductile fracture due to microvoid coalescence of specimen 28 at 50°C in oil. The black areas are voids and the white lines are the last strands of material which were broken upon failure of the specimen.

Figure 64 shows specimen 12 which was embrittled by hydrogen at -1.1V vs. s.c.e. at 21°C. Some secondary cracks on the specimen can be seen. The crack propagated from the edge to approximately halfway across the specimen when finally failure occurred due to mechanical overload. SEM fractographs of the cracked surface and the overload surface are shown in Figures 65 and 66, respectively. In comparison to the ductile failure of steel in oil at 50°C, these

fracture surfaces are flat with few voids present. This reveals that the failure is brittle both during cracking and overload.

Figure 67 shows specimen 6 which was tested at E(corr) at 21°C. Many secondary cracks can be seen on the surface and edges of the specimen. Failure appears to have occurred by stepwise cracking through the specimen, a ductile tearing from one brittle crack to another. This stepwise cracking occurs in a steel when it is embrittled by hydrogen as was shown for carbon steel in an ammonium carbonate solution as well as in a sodium carbonate-sodium bicarbonate solution.' Figure 68 shows the cracked surface and there is considerable ductility present with some flat areas associated with brittleness. Referring to specimens 6 and 12, it is evident that for higher hydrogen content (lower potentials) less secondary cracking is present. This also has been observed by other researchers.'

Figure 69 shows specimen 33 which was tested at E(corr) at 70°C. Considerable necking is shown but a brittle failure occurred as is evident in Figure 70 which is the fracture surface. However, this brittle failure occurred at almost 38% elongation and therefore is not that severe.

6.4.3 X-65 Steel

Constant strain rate tests were also performed on X-65 steel at varying potentials. Most of the tests were done at 21°C, one at 50°C, and one at 70°C. Table 14 lists the

results of these tests.

Figure 71 is a graph of percent elongation versus potential at 21°C. Hydrogen embrittlement occurs at -1.1V vs. s.c.e. as expected. The percent elongation at E(corr) and E(pp) is approximately the same as in air. E(corr) at 21°C for X-65 steel during the constant strain rate test was -0.810V vs. s.c.e. although E(corr) from the polarization curve was -0.869V vs. s.c.e. (compare Tables 7 and 14). At -0.810V vs. s.c.e. there is not much hydrogen charging of the steel and this is reflected in no loss of ductility. If the potential had been set to -0.869V vs. s.c.e., most likely a loss of ductility would be observed since there would be a significant amount of hydrogen charging.

There appears to be a loss in ductility as the potential is increased above E(pp) into the critical potential range of SCC. The specimens continued to neck but the amount or extent of necking was reduced at potentials within the critical range. Figure 72 is a graph of the elongation parameter versus potential and this shows the loss in ductility at potentials above E(pp) more readily since the elongations are normalized to the inert environment test on a scale of 0 to 1.0.

6.5 Comparison of the Steels

The microstructures of the two steels are quite different. The dual-phase steel has a ferrite-martensite structure whereas the pipeline steel (X-65) has a ferrite-pearlite structure. The difference in microstructure is the main reason for the different mechanical behavior of dual-phase steel. The dual-phase steel is very ductile and formable compared to the pipeline steel.

The polarization of the two steels in the 0.5 M Na_2CO_3 - 0.5 M $NaHCO_3$ solution is similar. No cathodic loops are observed at any of the temperatures tested for the pipeline steel whereas cathodic loops are observed for the dual-phase steel. The effect of temperature on the corrosion behavior is similar for both steels since the activation energies calculated for the anodic peak region are approximately the same.

The structure dependence of corrosion at potentials in the "upper slope" region are significantly different. Martensite is selectively attacked in the dual-phase steel whereas pitting and relatively uniform corrosion occurs in the pipeline steel. Referring to the constant strain rate tests performed at temperatures of 21, 50, and 70°C, the pipeline steel appears to be susceptible to SCC if the elongation parameter is used (see Table 15). The elongation parameters for the temperatures of 50 and 70°C for the pipeline steel were calculated using $e_{....} = 32.5$ % (the elongation at room temperature in air). The elongation

parameter decreases as the temperature is increased for the pipeline steel indicating increased susceptibility to SCC. Comparing the elongation parameter (0.83) at 70°C (-0.700 V vs. s.c.e.) to the elongation parameter (0.73) at 21°C for hydrogen embrittlement (-1.1 V vs. s.c.e.) the reduction in ductility in the "critical" potential range is approaching the reduction in ductility resulting from hydrogen embrittlement at 21°C. The specimen that was embrittled by hydrogen cracked, whereas the specimens in the "critical" range at both 50 and 70°C had reduced necking (i.e., a lower reduction in area at fracture) compared to the inert test. The dual-phase steel does not show a decrease in the elongation parameter with temperature; it remains near 1.0. The above indicates that the pipeline steel is somewhat susceptible to SCC at the potentials tested and that the dual-phase steel appears to be unsusceptible to SCC at corresponding "critical" potentials.

The reason for no susceptibility to SCC in the "critical" range is probably due to fact that the selectively corroded martensite islands are not linked together and thereby not producing a susceptible cracking path.

Table 15 also shows that hydrogen embrittlement at -1.1 V vs. s.c.e. and 21°C in the dual-phase steel is worse than in the pipeline steel under the same conditions if the elongation parameter is used. However, if the absolute elongation is compared, the pipeline steel appears to be

more susceptible to hydrogen embrittlement for a certain amount of overpotential (see Figure 73). One must take the yield strengths into consideration since the elongation will decrease with an increase in strength. The mode of failure and the amount of secondary cracking for the two steels were similar. The dual-phase steel initiated the primary crack at an elongation of 24.5 % and this crack propagated through the material until final brittle fracture due to overload occurred at an elongation of 26.7 %. The pipeline steel had already been necking when the primary hydrogen-induced crack was initiated at the center of the specimen at an elongation of 23.8 %. Almost instantaneous failure of the specimen occurred after initiation.

The strong, hard phase of martensite in the dual-phase steel is susceptible to hydrogen embrittlement and an increase in volume percent of martensite would probably increase the susceptibility to hydrogen embrittlement of dual-phase steels.

6.6 Suitability of Dual-Phase Steel for Pipeline Application

Carbonates and bicarbonates that form near buried pipelines have been shown to contribute to SCC of pipeline steels.[11,12] The dual-phase steel shows virtually no susceptibility to SCC in a carbonate-bicarbonate solution. No "critical" potential range in which SCC occurs has been found for dual-phase steel at any of the test temperatures although a "critical" range has been observed when conventional pipeline steels were tested.[2] This would indicate that the dual-phase steel would be more suitable than the presently-used pipeline steel if this were the only factor to be concerned with.

Pipelines are cathodically protected and therefore some parts of the pipeline may be overprotected, which results in some hydrogen charging. The dual-phase steel and pipeline steel that were tested appear to respond similarly to hydrogen charging (see Figure 73). For both steels, a significant amount of deformation must occur before hydrogen has any effect. The two steels were tested at the same overpotential (-1.1V vs. s.c.e.) and this resulted in the same amount of hydrogen charging as indicated by approximately the same cathodic current density.

At the rest potential or corrosion potential, the dual-phase steel is susceptible to hydrogen as is indicated by the many secondary cracks and reduced ductility. In comparison, at rest potential and 21°C in the carbonate-bicarbonate solution, the pipeline steel does not

show any susceptibility to hydrogen embrittlement since the potential is close to the reversible potential of hydrogen (-0.8V vs. s.c.e.). It appears that at increasing potentials in the water decomposition range where hydrogen charging of the steel occurs, the amount of deformation which is needed for hydrogen embrittlement to occur is increased. Since the pipeline steel is not as ductile as the dual-phase steel the amount of deformation needed for embrittlement at higher potentials cannot be achieved and therefore a ductile failure occurs. For dual-phase steels, at these higher potentials, the deformation needed is attainable and failure occurs as a result of hydrogen-induced cracking.

Taking the above into consideration, the dual-phase steel does not appear to be any more susceptible to hydrogen embrittlement than pipeline steel, although the effect of hydrogen is evident over a wider range of potentials due to its greater ductility.

In summary, the suitability of dual-phase steel for pipeline application appears to be as good or better than the presently-used ferrite-pearlite pipeline steel. The dual-phase steel shows virtually no susceptibility to SCC in carbonate-bicarbonate solution and hydrogen embrittlement of the dual-phase steel is very similar to that of pipeline steel.

7. Conclusions

1. Dual-phase steel is less susceptible to SCC than pipeline steel in a 0.5 M Na_2CO_3 - 0.5 M $NaHCO_3$ solution at potentials in the region where passivation begins to occur (above the primary passivation potential, E(pp)). At these potentials, initial corrosion after exposure of the dual-phase steel to the environment is structure dependent. There is selective attack of the martensite phase and this phase is not aligned in any direction but randomly distributed, resulting in a microstructure which is unsusceptible to SCC. Selective corrosion of the martensite phase leaves approximately 85 % of the material unattacked and unsusceptible to SCC. Initially the martensite is attacked severely, leaving the martensite unsusceptible to SCC since SCC usually does not occur where corrosion rates are high.
2. Hydrogen embrittlement of dual-phase steel is similar to hydrogen embrittlement of pipeline steel at a potential of -1.1V vs. s.c.e. in the range where water decomposition occurs. An increase in potential in this range to the corrosion or rest potential (-0.856V vs. s.c.e.) for dual-phase steel results in an increase in the amount of deformation needed for hydrogen embrittlement to occur and an increase in the amount of secondary cracking.

Table 1. Some Environments that may cause SCC of Ordinary Steels

Environment
NaOH solutions
$NaOH-Na_2SiO_2$ solutions
Calcium, ammonium, and sodium nitrate solutions
Mixed acids ($H_2SO_4-HNO_3$)
HCN solutions
Acidic H_2S solutions
Seawater
Molten Na-Pb alloys

Table 2. Compositions of some Solutions near Cracks (from Fessler and Barlo'[3])

	Amount in Solution, percent				
pH	CO_3^{2-}	HCO_3^-	OH^-	Cl^-	NO_3^-
9.7	0.5	0.5	-	-	-
12.3	1.0	N	0.1	0.01	0.007
10	1.4	0.5	N	0.12	0.004
10	0.9	0.8	N	0.02	0.01
9.6	0.5	0.6	N	N	-
10.5	0.7	0.4	N	-	N

- the primary cation in all of the solutions was sodium

N - nondetectable

Table 3. Typical Compositions of Dual-Phase Steels (from Speich[24])

Production Technique	Compositions, wt. %									
	C	Mn	Si	Cr	Mo	V	Al	N	S	P
Continuous Annealing, Hot-Rolled	.12	1.55	.61	-	-	.06	.05	.007	.006	.015
	.11	1.43	.58	.12	.08	-	.04	.007	.012	.015
Continuous Annealing, Cold-Rolled	.11	1.20	.40	-	-	-	.04	-	.005	.015
Box Annealing	<.13	<2.20	<1.5	<1.0	-	-	<.08	-	<.020	<.02
As-Rolled	.06	.90	1.35	.50	.35	-	.03	-	.010	.010

- other additions include rare earths

Table 4. Composition and Mechanical Properties of the Dofasco Dual-Phase Steel

DOFASCO EXPERIMENTAL AS-ROLLED DUAL-PHASE STEEL

Mechanical Properties (Rolling Direction)

Yield Strength ksi(MPa)	Tensile Strength ksi(MPa)	% Elongation (in 2")
59.6(411)	90.7(625)	30.0

Product Analysis (Wt. %)

C	Mn	P	S	Si	Cr	Sn	Al
.06	.82	.009	.009	1.61	.57	<.001	.006

Cu	N	Zr	Mo	V	Nb	Ti	Ni
.02	.007	.004	.38	.005	.009	.003	.02

Table 5. Composition and Mechanical Properties of the X-65 Pipeline Steel

X-65 PIPELINE STEEL

Mechanical Properties (Rolling Direction)

Yield Strength ksi(MPa)	Tensile Strength ksi(MPa)	% Elongation (in 2")
68.8(474)	85.7(591)	33.0

Product Analysis (Wt. %)

C	Mn	P	S	Si	Nb	Cu	Ni
.096	1.47	.016	.005	.16	.045	.029	.012

Cr	Mo	V	Sn	Ce
.049	.006	.005	.005	.016

Table 6. Active-Passive Parameters as a function of Temperature for Dual-Phase Steel

Temperature (°C)	E(corr) (V)	E(pp) (V)	i(c) (mA/cm²)	i(p) (mA/cm²)
22	-0.855	-0.670	0.31	0.0044
50	-0.876	-0.725	0.71	0.0088
70	-0.910	-0.750	1.95	0.010
90	-0.923	-0.790	3.31	0.017

- the potentials are with respect to the saturated calomel electrode (s.c.e.)

Table 7. Active-Passive Parameters as a function of Temperature for X-65 Pipeline Steel

Temperature (°C)	E(corr) (V)	E(pp) (V)	i(c) (mA/cm²)
22	-0.869	-0.683	0.33
50	-0.902	-0.694	1.58
90	-0.924	-0.788	4.98

- the potentials are with respect to the saturated calomel electrode (s.c.e.)

Table 8. Active-Passive Parameters as a function of Dissolved Oxygen for Dual-Phase Steel

Environment	E(corr) (V)	E(pp) (V)	i(c) (mA/cm²)	i(p) (mA/cm²)
Aerated	-0.830	-0.690	0.38	0.0046
De-aerated	-0.855	-0.670	0.31	0.0044

- the potentials are with respect to the saturated calomel electrode (s.c.e.)

Table 9. Possible Reactions in Carbonate/Bicarbonate Solution

Specific conditions:

$[CO_3^{2-}] = 0.5M$
$[HCO_3^-] = 0.5M$
pH = 9.5
Temp. = 22°C
$[O_2] = 2.781 \times 10^{-4}M$ (Aerated)
$[O_2] = 10^{-4}M$ (De-aerated)

Reaction	E (V s.h.e.)	E (V s.c.e.)
Oxygen evolution		
$2H_2O \rightarrow O_2 + 4H^+ + 4e^-$ $E = 1.229 - 0.0586\ pH$	0.672	0.430
Oxygen reduction		
$O_2 + 2H_2O + 4e^- \rightarrow 4OH^-$ $E = 0.401 + 0.0586\ (14 - pH) + 0.0147 \log[O_2]$		
Aerated:	0.612	0.370
De-aerated:	0.576	0.334
Water decomposition		
$2H_2O + 2e^- \rightarrow H_2 + 2OH^-$ $E = -0.0586\ pH$	-0.557	-0.799
Iron oxidation		
$Fe + CO_3^{2-} \rightarrow FeCO_3 + 2e^-$ $E = -0.755 - 0.0293 \log[CO_3^{2-}]$	-0.746	-0.988
$Fe + HCO_3^- \rightarrow FeCO_3 + H^+ + 2e^-$ $E = -0.45 - 0.0293\ pH - 0.0293 \log[HCO_3^-]$	-0.720	-0.962

Table 10. Corrosion Rate as a function of Temperature for Dual-Phase Steel

Temp. (°C)	ΔE (V)	β_a (V/decade)	β_c (V/decade)	i(corr) (mA/cm²)
22	-0.02	0.162	-0.0602	0.0215
50	-0.02	0.0750	-0.0591	0.0500
70	-0.02	**	**	**
90	-0.02	0.0785	-0.0840	0.372
22 *	-0.02	0.173	-0.157	0.0455
22	-0.03	0.155	-0.0693	0.0254
50	-0.03	0.0947	-0.0637	0.0573
70	-0.03	0.0985	-0.0669	0.146
90	-0.03	0.114	-0.105	0.512
22 *	-0.03	0.0960	-0.179	0.0347
22	-0.04	0.229	-0.0992	0.0467
50	-0.04	0.106	-0.0709	0.106
70	-0.04	0.124	-0.0758	0.163
90	-0.04	0.109	-0.0945	0.450
22 *	-0.04	0.0850	-0.0814	0.020

* - test solution saturated with oxygen.

** - U_1 and U_2 could not be calculated since the $r_2^2 - 4\sqrt{r_1}$ term was negative.

Table 11. Corrosion Rate as a function of Temperature for X-65 Steel

Temp. (°C)	ΔE (V)	β_a (V/decade)	β_c (V/decade)	i(corr) (mA/cm²)
22	-0.02	0.0809	-0.0498	0.0150
50	-0.02	0.0721	-0.0409	0.0478
90	-0.02	0.0663	-0.0459	0.0959
22	-0.03	0.151	-0.0830	0.0315
50	-0.03	0.0870	-0.0502	0.0590
90	-0.03	0.419	-0.173	0.857
22	-0.04	*	-0.226	0.185
50	-0.04	0.288	-0.0817	0.186
90	-0.04	0.123	-0.0805	0.260

* - U_2 was too close to 1.0 and resulted in an invalid slope.

Table 12. Current Densities as a function of Temperature

DUAL-PHASE STEEL

Temp. (°C)	i(c) (mA/cm²)	i(p) (mA/cm²)	ΔE=-0.02V i(corr) (mA/cm²)	ΔE=-0.03V i(corr) (mA/cm²)	ΔE=-0.04V i(corr) (mA/cm²)
22	0.31	0.0044	0.0215	0.0254	0.0467
50	0.71	0.0088	0.0500	0.0573	0.106
70	1.95	0.010	*	0.146	0.163
90	3.31	0.017	0.372	0.512	0.450

* - could not be calculated.

X-65 STEEL

Temp. (°C)	i(c) (mA/cm²)	i(p) (mA/cm²)	ΔE=-0.02V i(corr) (mA/cm²)	ΔE=-0.03V i(corr) (mA/cm²)	ΔE=-0.04V i(corr) (mA/cm²)
22	0.33	*	0.0150	0.0315	0.185
50	1.58	*	0.0478	0.0590	0.186
90	4.98	*	0.0959	0.857	0.260

* - passive current not constant but decreases with increasing potential.

Table 13. Constant Strain Rate Test Results for Dual-Phase Steel

Specimen	T (°C)	Environment	Yield Strength (ksi)	Tensile Strength (ksi)	Elongation (%)
A	21	Air	57.6	85.9	43.7
1	21	Air	57.4	86.2	42.0
3	21	-0.670 V	58.0	87.9	43.5
4	21	-0.600 V	59.0	87.1	44.8
5	21	-0.550 V	58.1	88.9	44.0
6	21	-0.856 V *	59.7	90.0	34.8
9	21	-0.770 V	56.0	90.6	41.5
10	21	-0.450 V	57.5	89.2	43.8
12	21	-1.100 V	58.2	86.1	26.7
14	50	-1.100 V	54.7	87.2	22.9
15	50	-0.876 V *	54.1	86.9	40.1
17	50	-0.800 V	57.3	83.5	43.2
19	50	-0.625 V	51.3	89.4	42.1
20	50	-0.470 V	52.0	86.2	43.6
21	50	-0.350 V	52.2	88.4	43.5
22	50	-0.725 V	49.7	89.4	41.5
23	50	Rest Pot.**	47.5	87.7	43.7
24	50	-0.725 V	54.1	85.2	43.4
26	21	Air ($2\times10^{-4}s^{-1}$)	52.5	94.3	47.0
27	21	Air ($2\times10^{-4}s^{-1}$)	49.2	92.6	44.4
28	50	Oil	50.8	88.5	44.4
29	70	Oil	52.5	89.3	43.9
30	90	Oil	50.4	87.8	44.4
32	70	-1.100 V	48.7	86.0	32.0
33	70	-0.894 V *	51.2	87.6	37.9
34	70	-0.750 V	49.2	86.9	42.3
36	70	-0.632 V	54.4	86.4	42.1

- 1 ksi = 6.895 MPa

- potentials are with respect to the saturated calomel electrode (s.c.e.).

* - current during the test is kept as close to zero as possible by adjusting the potential.

** - no applied potential.

- specimen #15: strain rate=$3.5\times10^{-4}sec^{-1}$

Table 14. Constant Strain Rate Test Results for X-65 Steel

Specimen	T (°C)	Environment	Yield Strength (ksi)	Tensile Strength (ksi)	Elongation (%)
1	21	Air	63.5	82.5	32.5
2	21	-0.810 V *	67.2	83.2	33.5
3	21	-1.100 V	63.4	83.2	23.8
4	21	-0.683 V	64.1	82.8	32.8
5	21	-0.590 V	64.4	83.7	31.0
6	21	-0.517 V	76.7	87.9	29.7
7	50	-0.675 V	64.7	84.1	28.1
8	70	-0.700 V	63.5	84.9	27.0

- 1 ksi = 6.895 MPa

- potentials are with respect to the saturated calomel electrode (s.c.e.).

* - current during the test is kept as close to zero as possible by adjusting the potential.

Table 15. Comparison of Dual-Phase Steel and X-65 Steel

Steel	T (°C)	Environment	Elongation (%)	Elongation Parameter ($e/e_{in\,air}$)
Dual-Phase	21	-0.600 V *	44.8	1.03
Dual-Phase	50	-0.625 V *	42.1	0.95
Dual-Phase	70	-0.632 V *	42.1	0.96
Dual-Phase	21	Air	43.7	
Dual-Phase	50	Oil	44.4	
Dual-Phase	70	Oil	43.9	
Dual-Phase	21	-1.100 V	26.7	0.61
X-65	21	-0.590 V *	31.0	0.95
X-65	50	-0.675 V *	28.1	0.86
X-65	70	-0.700 V *	27.0	0.83
X-65	21	Air	32.5	
X-65	21	-1.100 V	23.8	0.73

- potentials are with respect to the saturated calomel electrode (s.c.e.).

* - upper slope potential from the polarization curve.

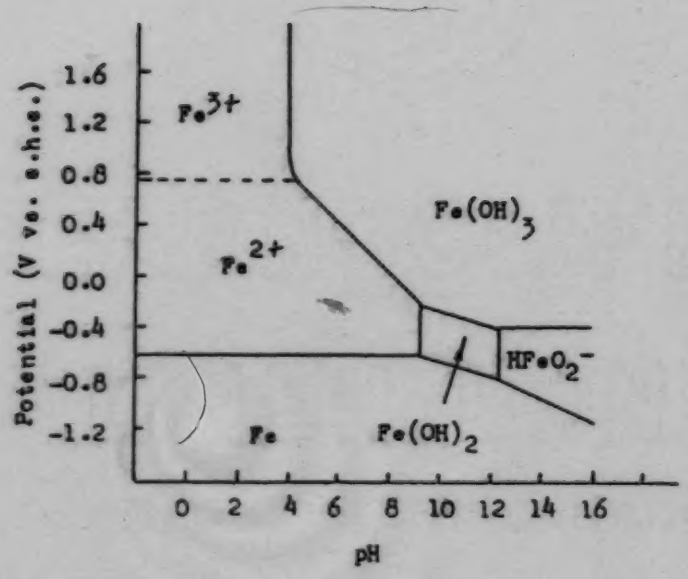

Figure 1. Potential-pH Diagram for the Fe-H_2O System (modified from Pourbaix[4])

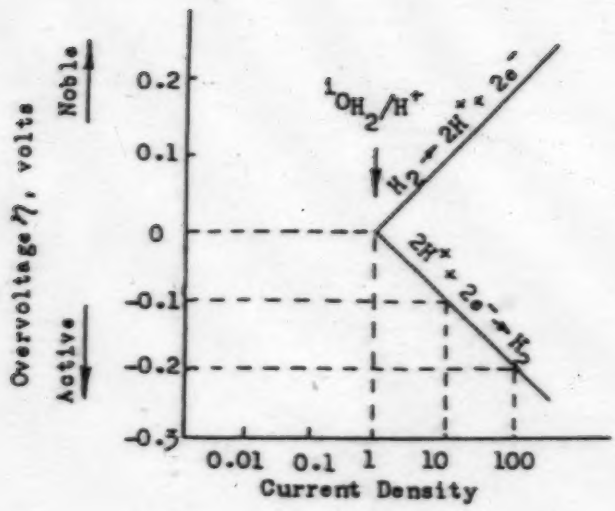

Figure 2. Activation Polarization Curve of a Hydrogen Electrode

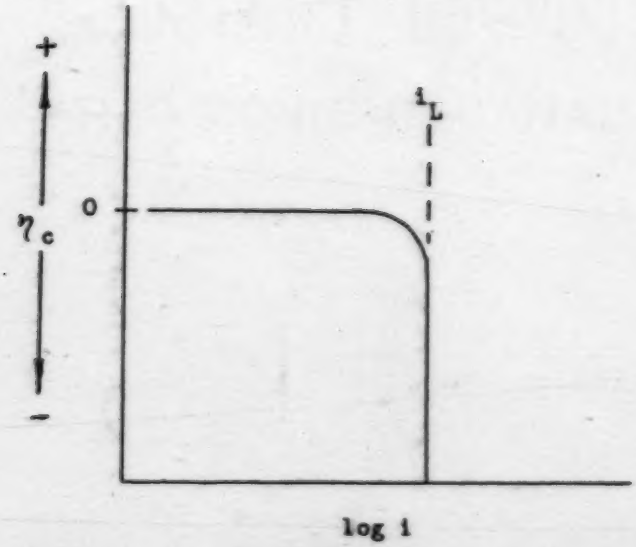

Figure 3. Concentration Polarization Curve

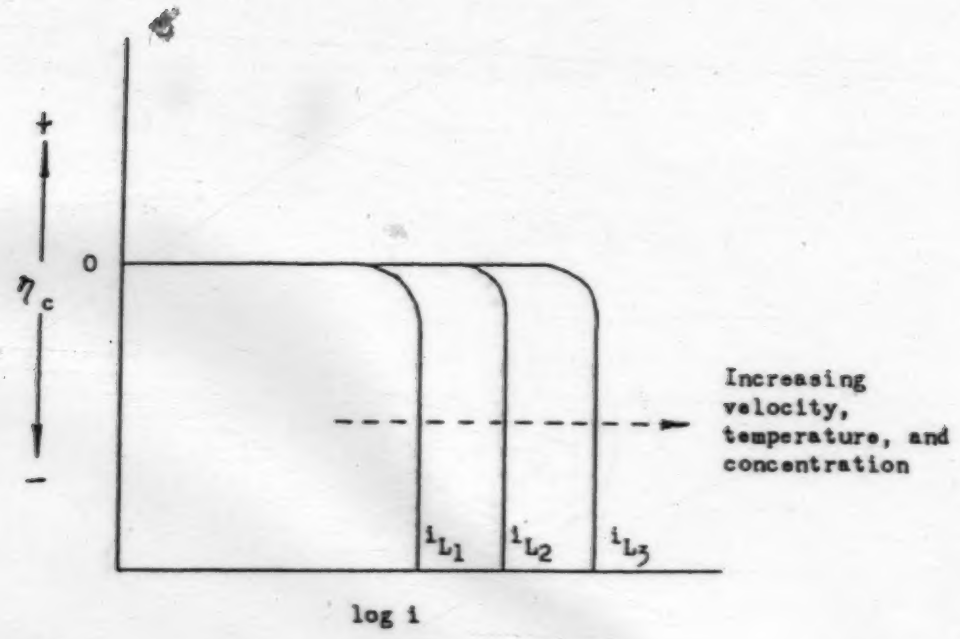

Figure 4. Effect of Environmental Variables on Concentration Polarization

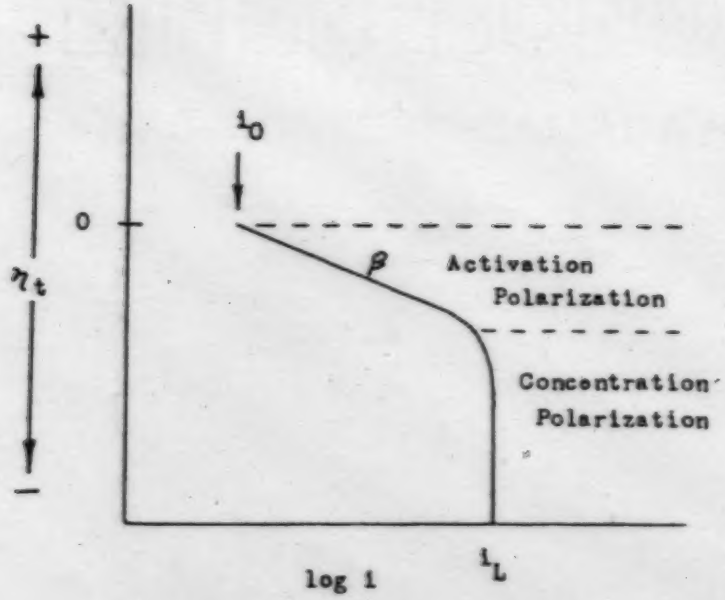

Figure 5. Combined Polarization Curve

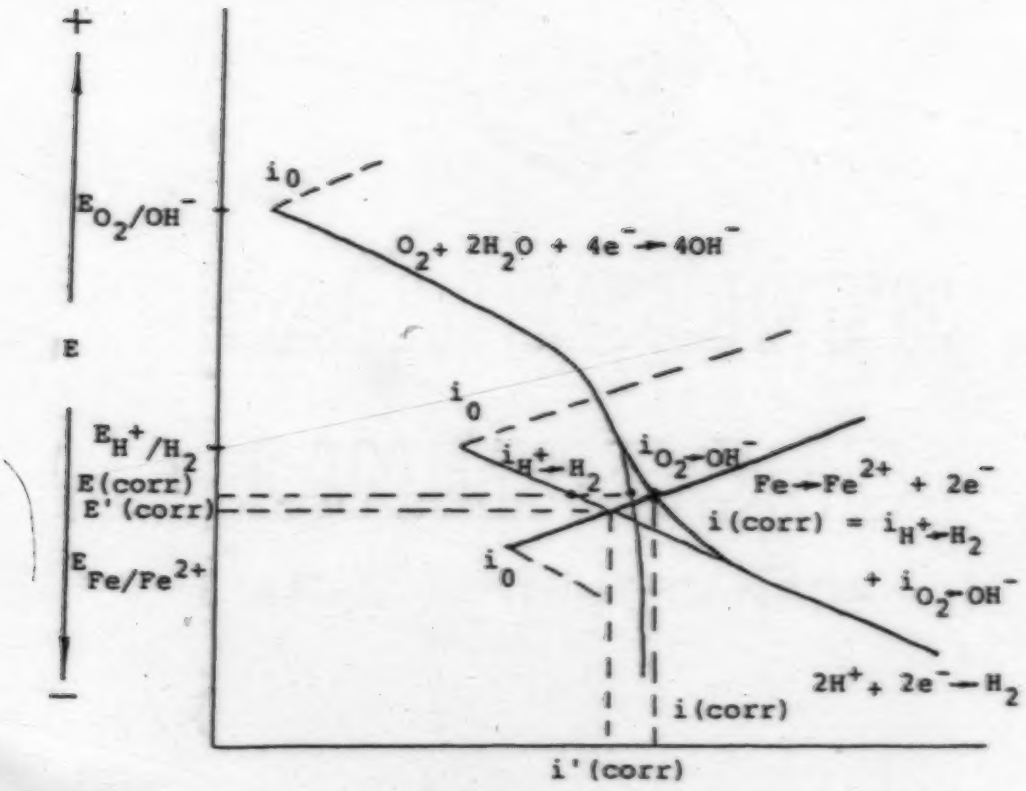

Figure 6. Behavior of Fe in Carbonate Solution

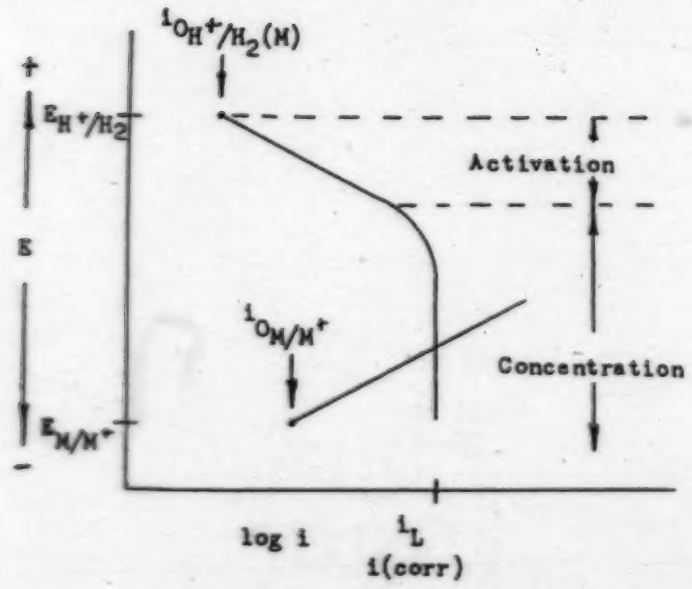

Figure 7. Corrosion of Metal under Diffusion Control

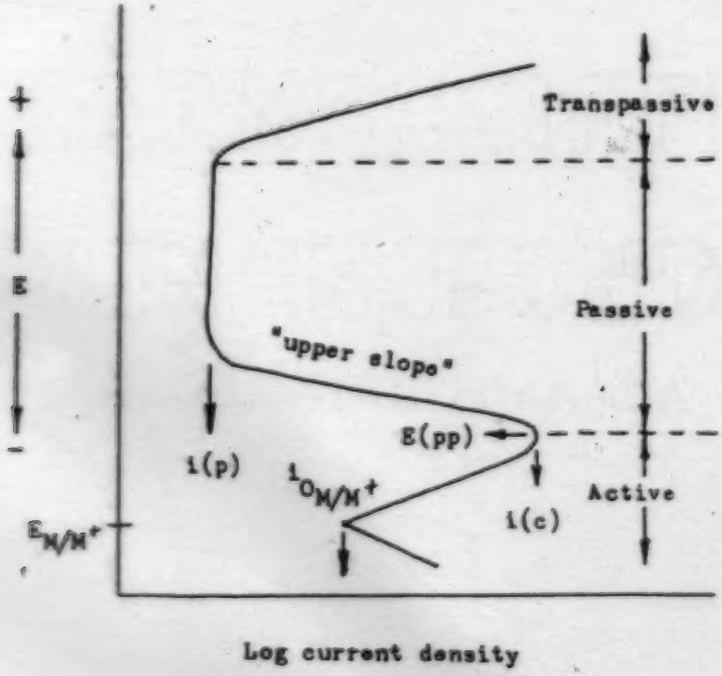

Figure 8. Anodic Dissolution Behavior of an Active-Passive Metal

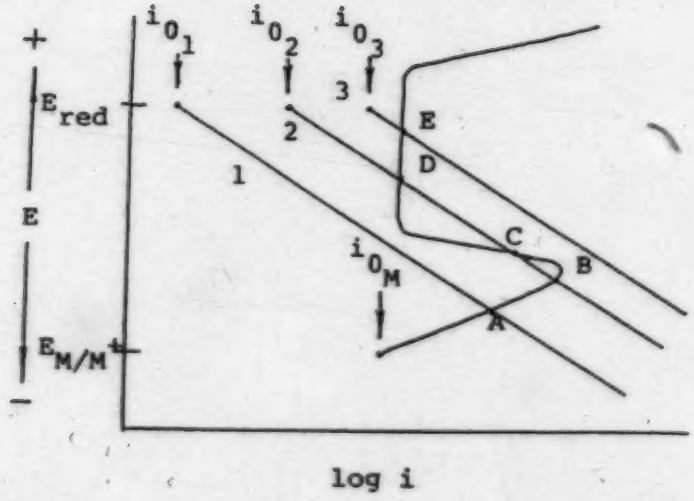

Figure 9. Behavior of an Active-Passive Metal under Corrosive Conditions

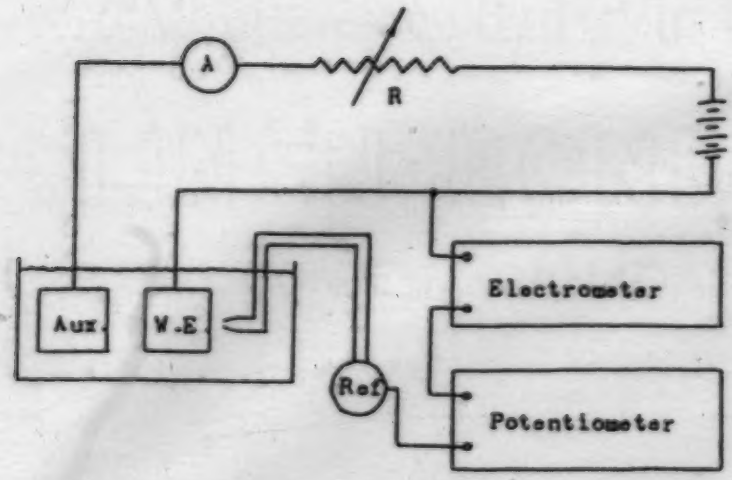

Figure 10. Electric Circuit for Cathodic Polarization Measurement

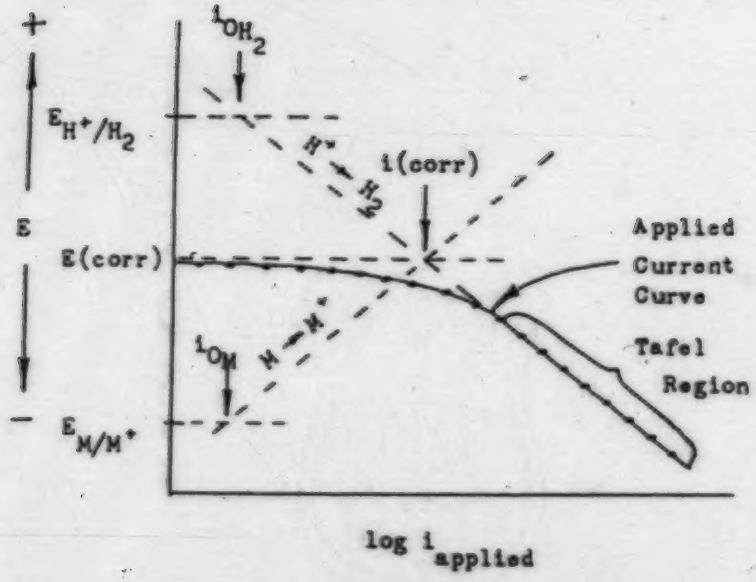

Figure 11. Applied Current Cathodic Polarization Curve

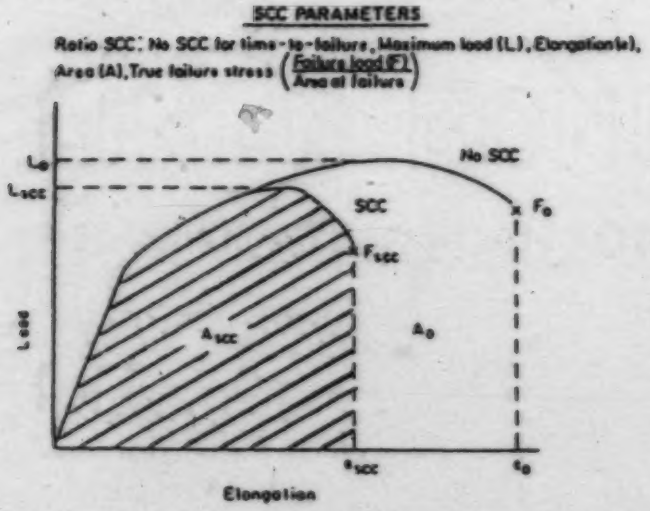

Figure 12. SCC Parameters (from Payer et al.[10])

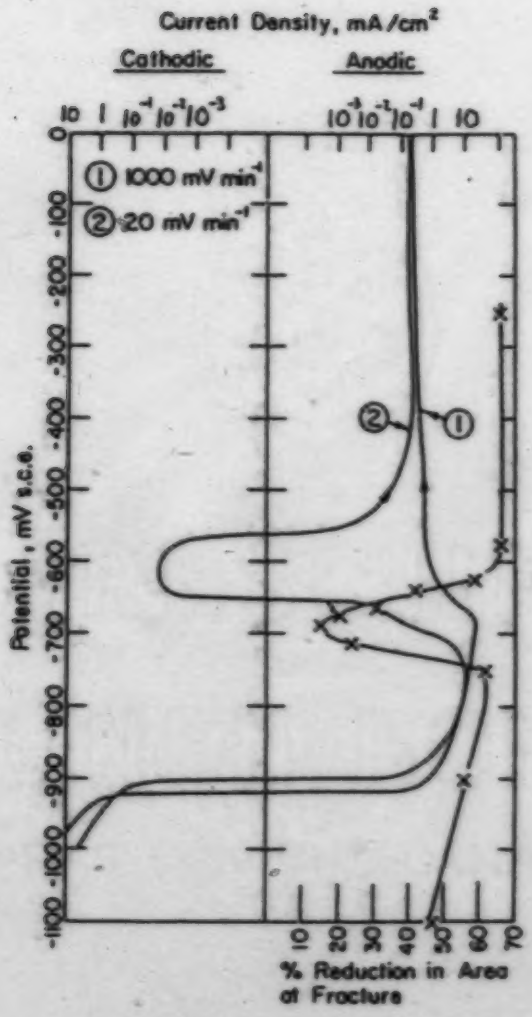

Figure 13. Polarization Curves and SCC Test Results for Mild Steel in 1N Na_2CO_3 - 1N $NaHCO_3$ at 90°C (modified from Sutcliffe et al.[1])

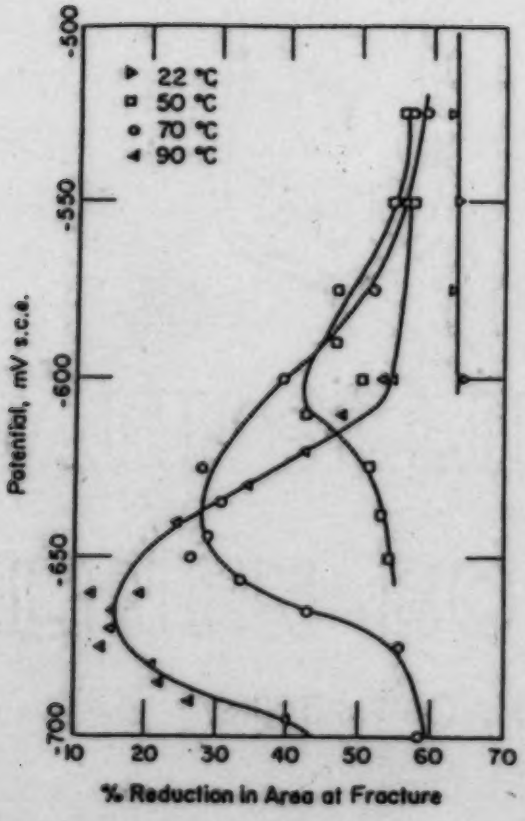

Figure 14. Effect of Temperature upon SCC of Mild Steel at Various Potentials in 1N Na_2CO_3 - 1N $NaHCO_3$ at 90°C (modified from Sutcliffe et al.')

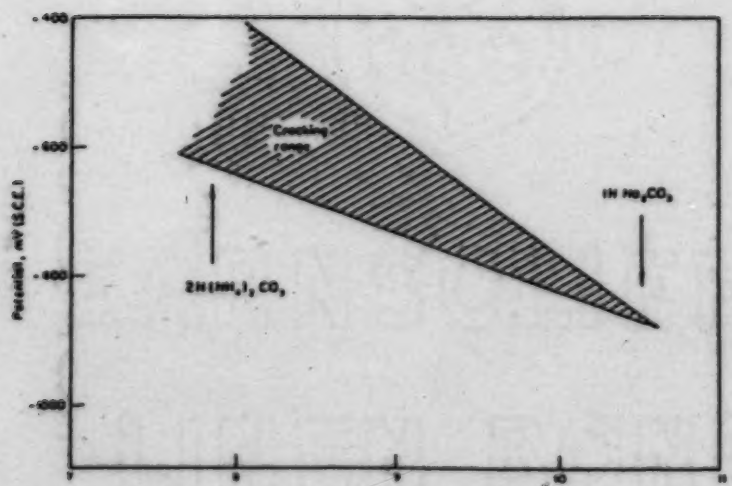

Figure 15. The pH Dependence of the SCC Range for Pipeline Steel (from Payer et al.[1])

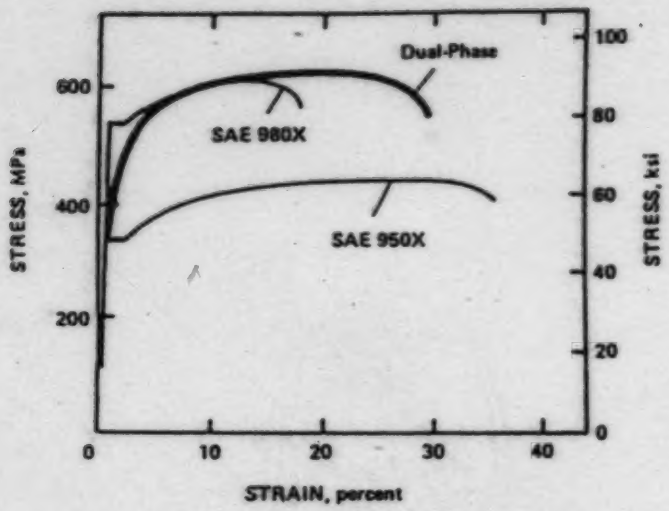

Figure 16. Comparison of Stress-Strain Curves for Dual-Phase Steel and Conventional HSLA Steel (from Speich[24])

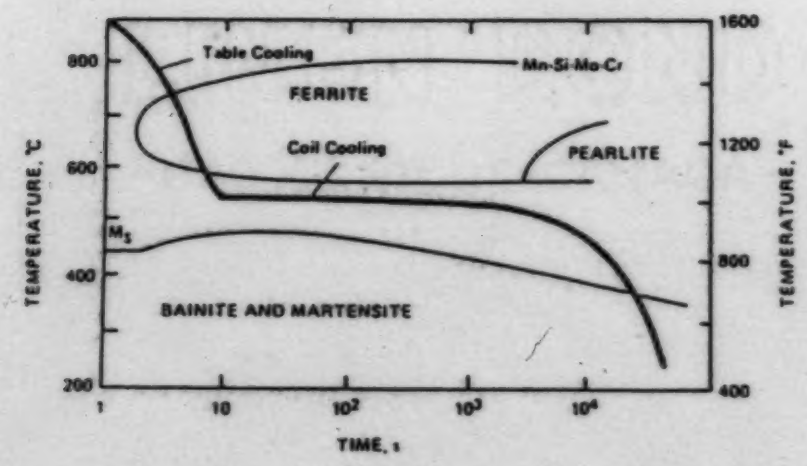

Figure 17. Continuous-Cooling Transformation for As-Rolled Dual-Phase Steel (from Speich[24])

Figure 18. Polarization Equipment

Figure 19. Cell Arrangement

Figure 20. Working Electrode Assembly

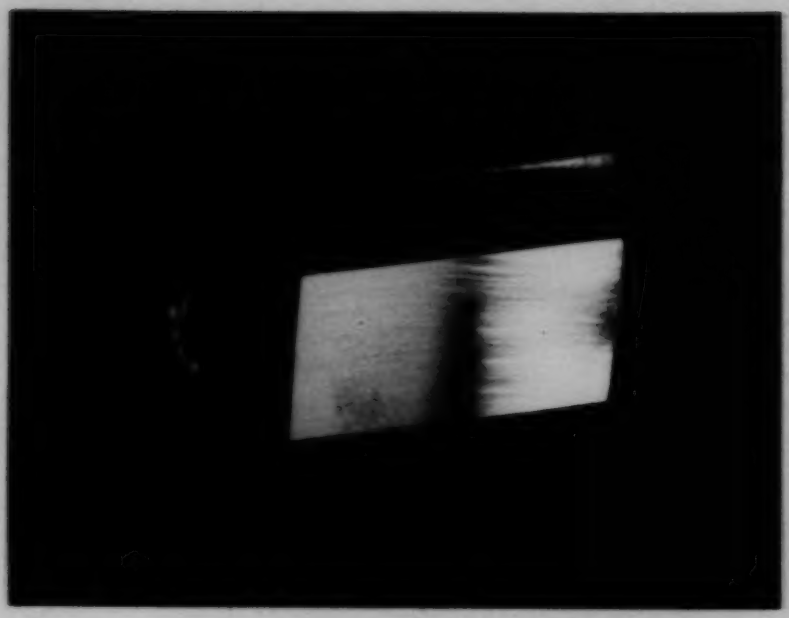

Figure 21. Steel Mounted in Bakelite

Figure 22. Counter Electrode Assembly

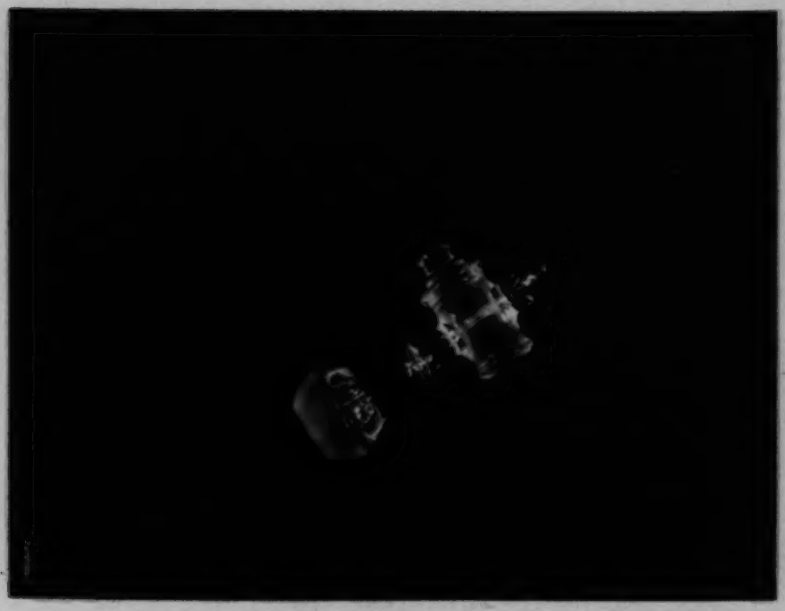

Figure 23. Salt Bridge Assembly

Figure 24. Temperature Control

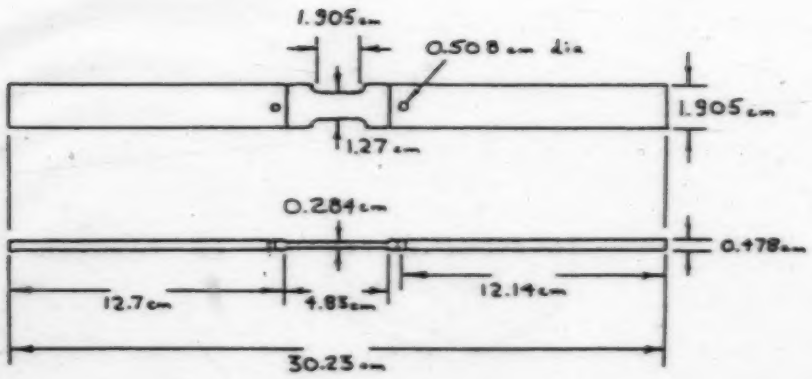

Figure 25. Tensile Specimen

Figure 26. Reduced Section of Tensile Specimen

Figure 27. Material Test System

Figure 28. Test Cell

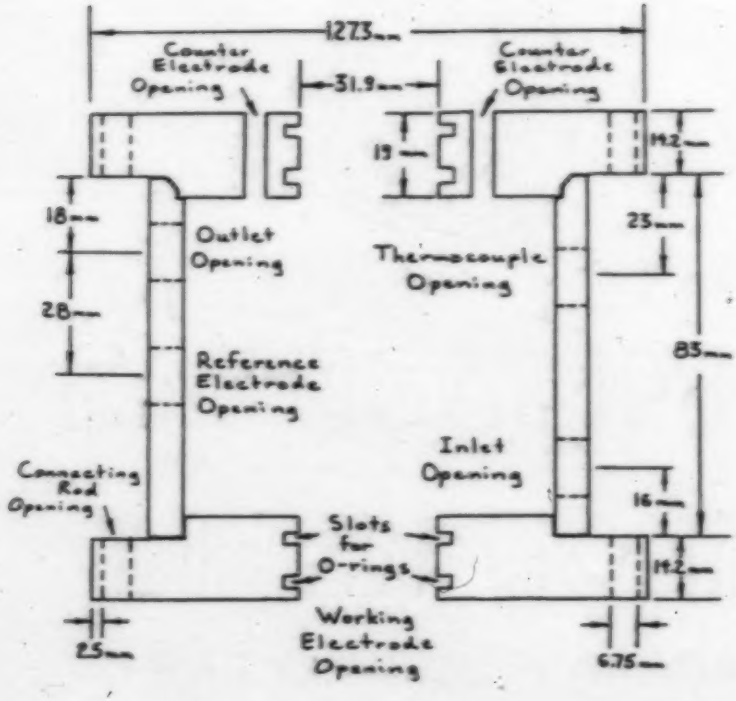

Figure 29. Test Cell Dimensions (side view)

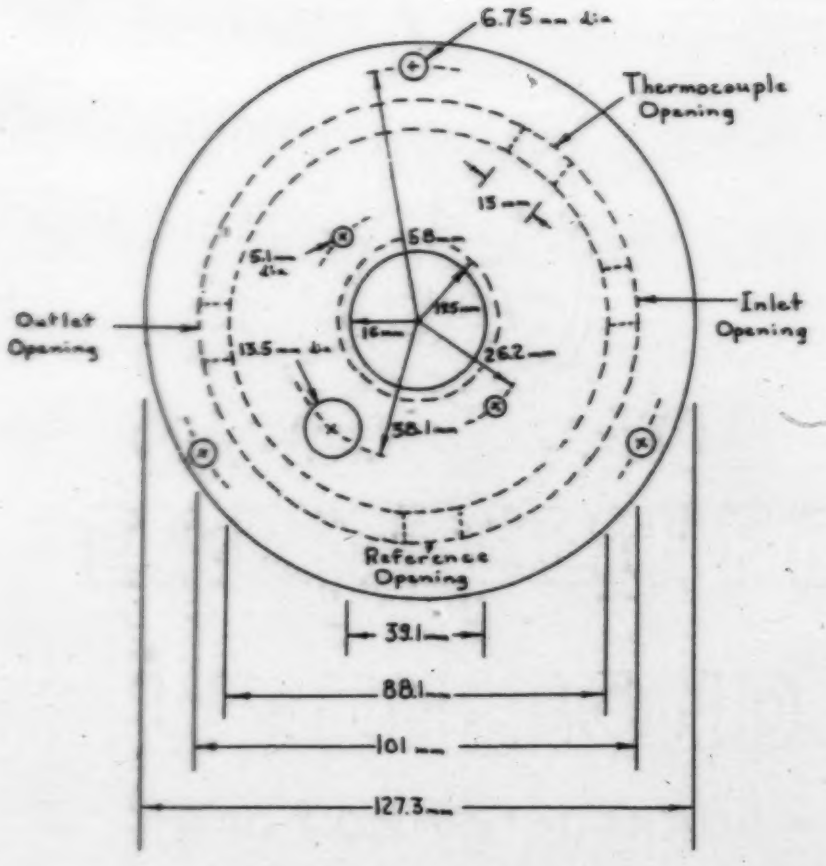

Figure 30. Test Cell Dimensions (top view)

Figure 31. Cemented Nylon Sleeve

Figure 32. Recirculation System

Figure 33. Dofasco Dual-Phase Steel (600X)

Figure 34. X-65 Pipeline Steel (600X)

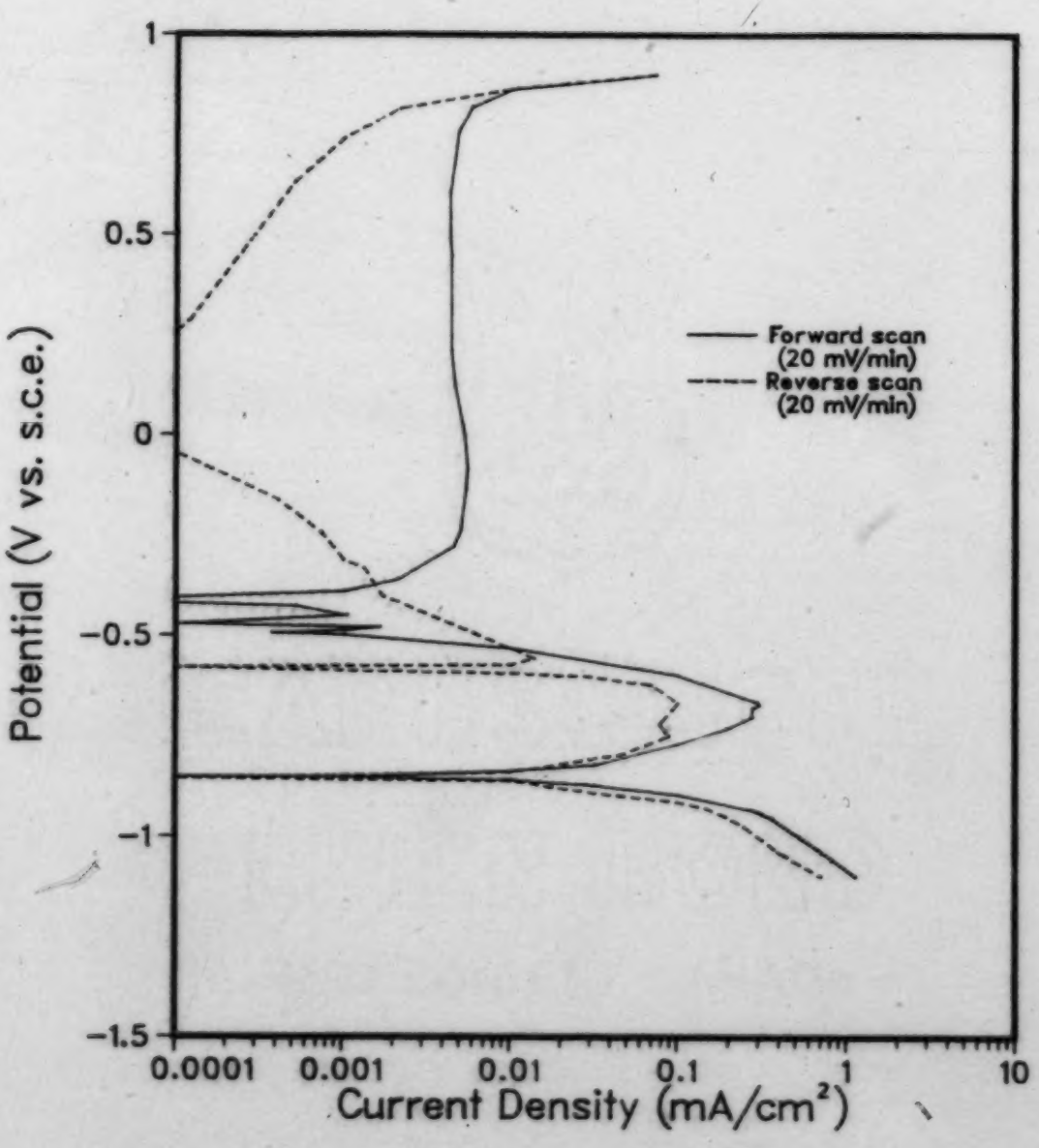

Figure 35. Polarization Curve of Dual-Phase Steel at 22°C

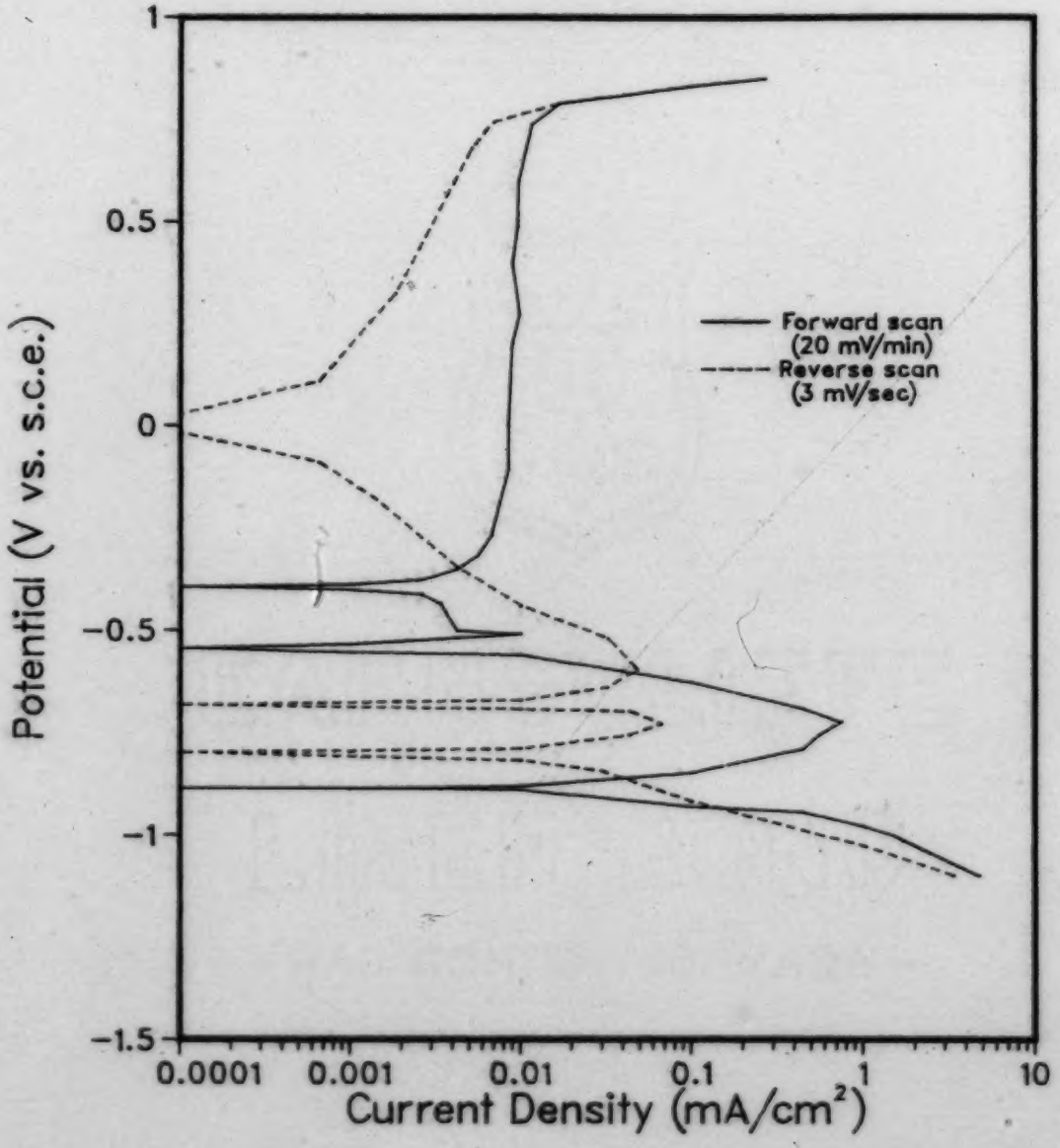

Figure 36. Polarization Curve of Dual-Phase Steel at 50°C

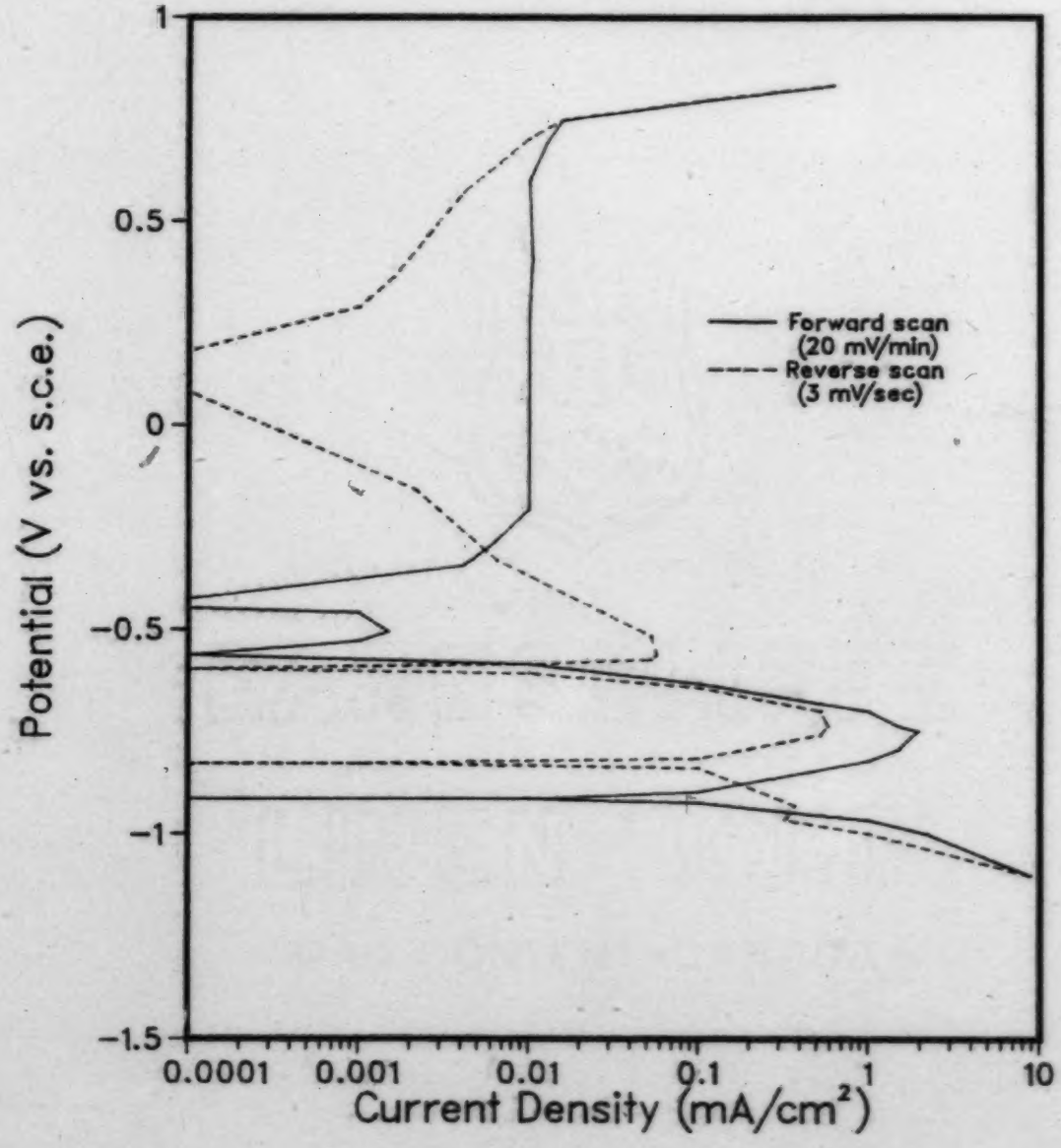

Figure 37. Polarization Curve of Dual-Phase Steel at 70°C

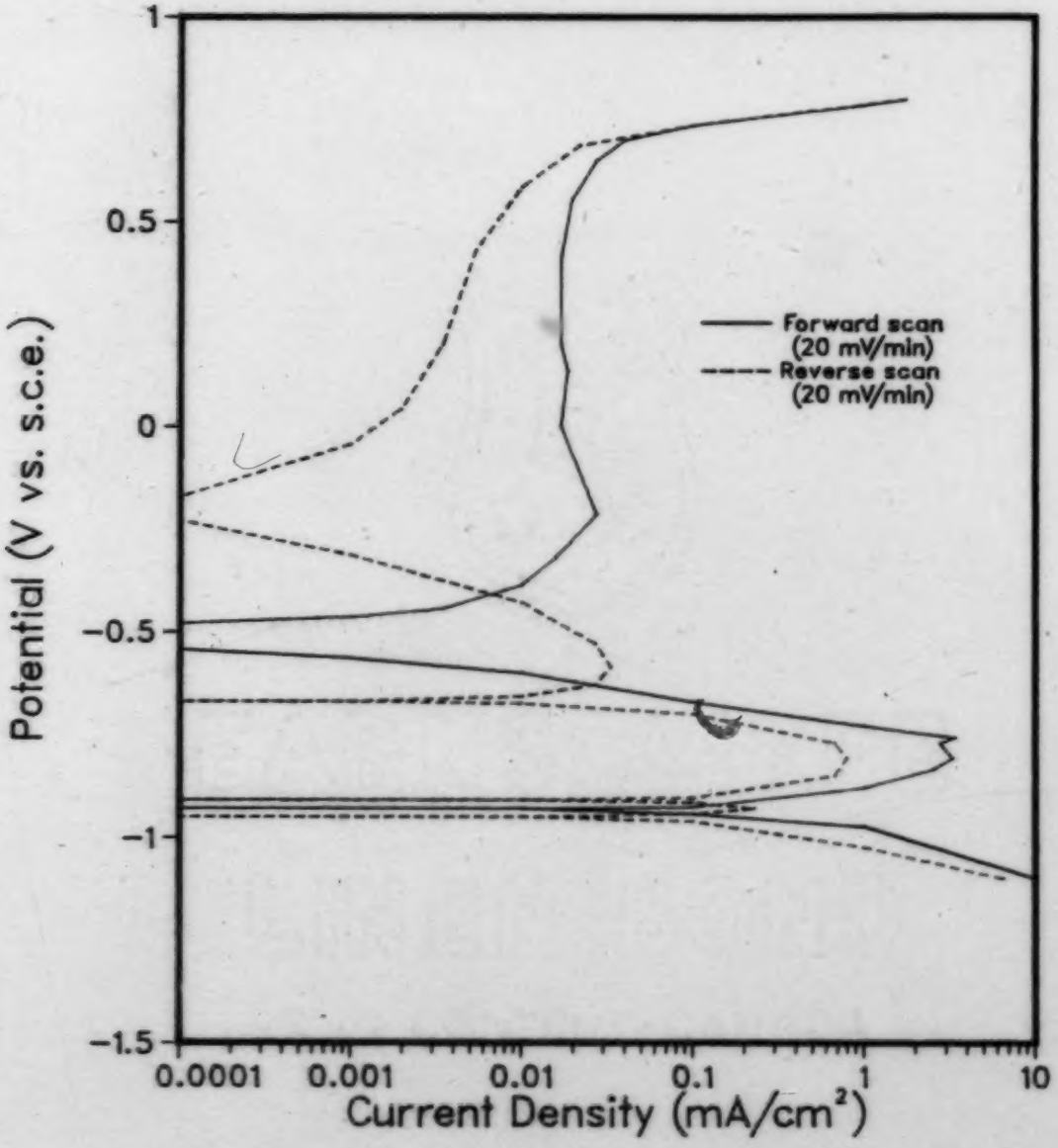

Figure 38. Polarization Curve of Dual-Phase Steel at 90°C

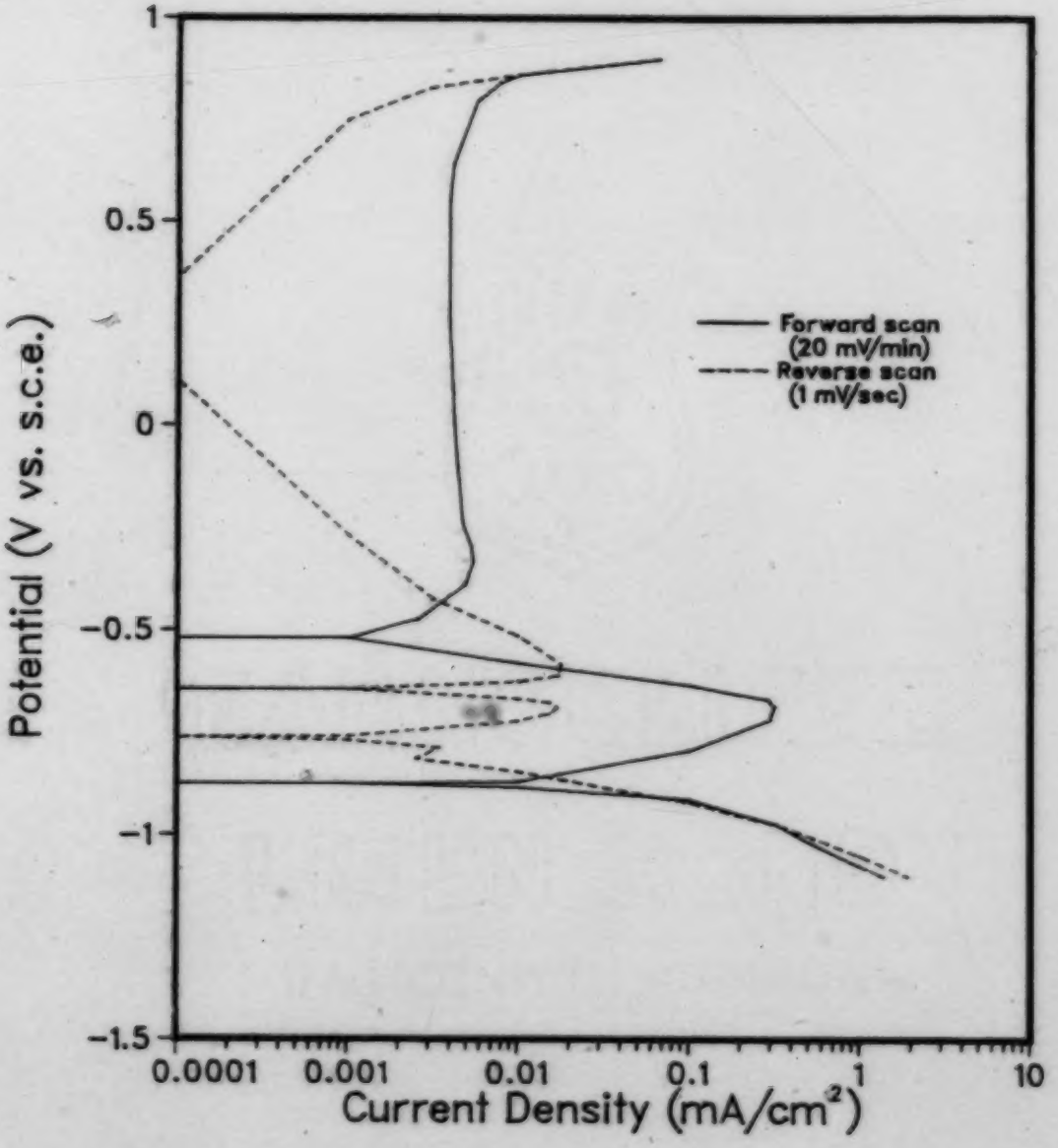

Figure 39. Polarization Curve of X-65 Steel at 22°C

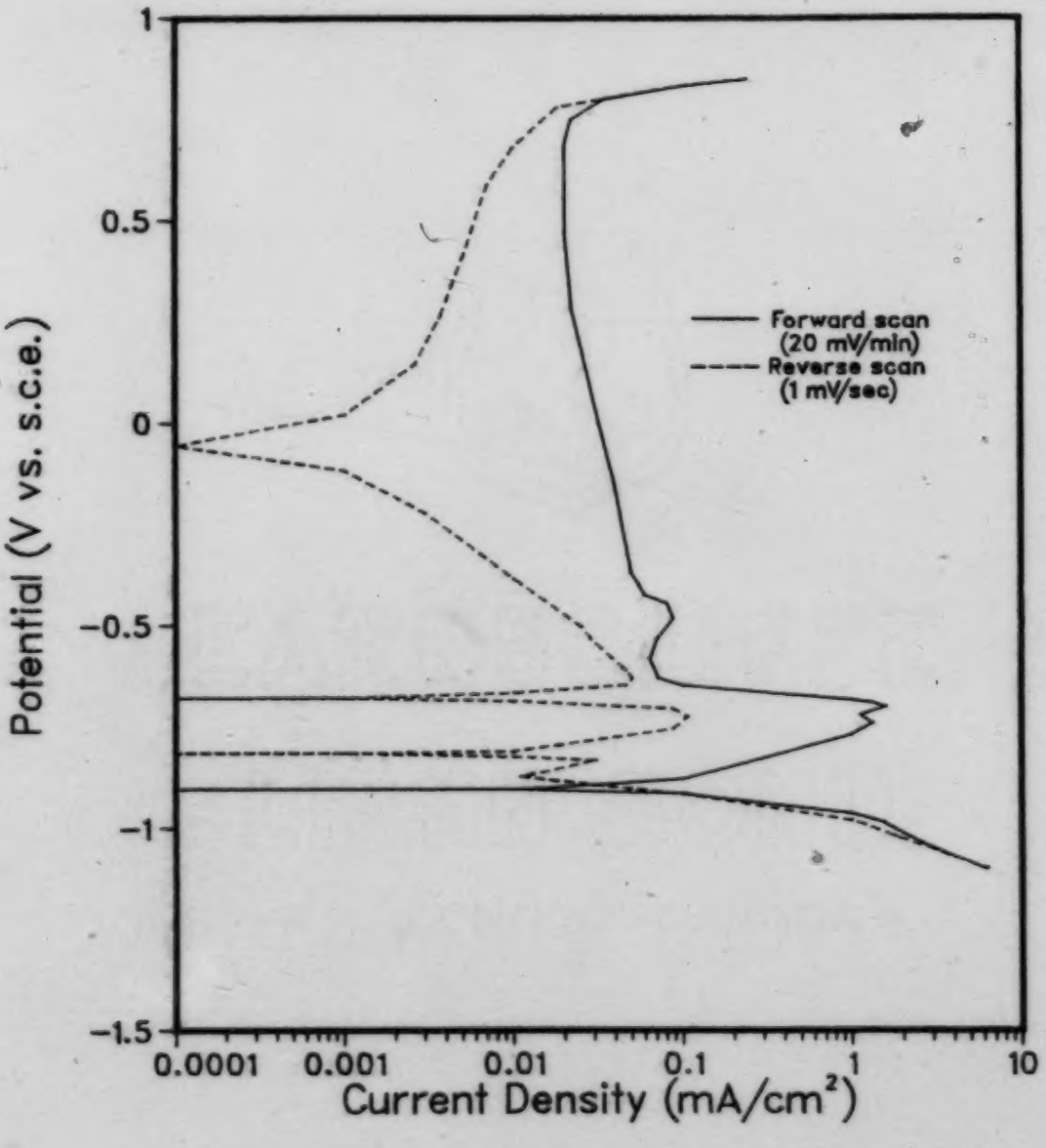

Figure 40. Polarization Curve of X-65 Steel at 50°C

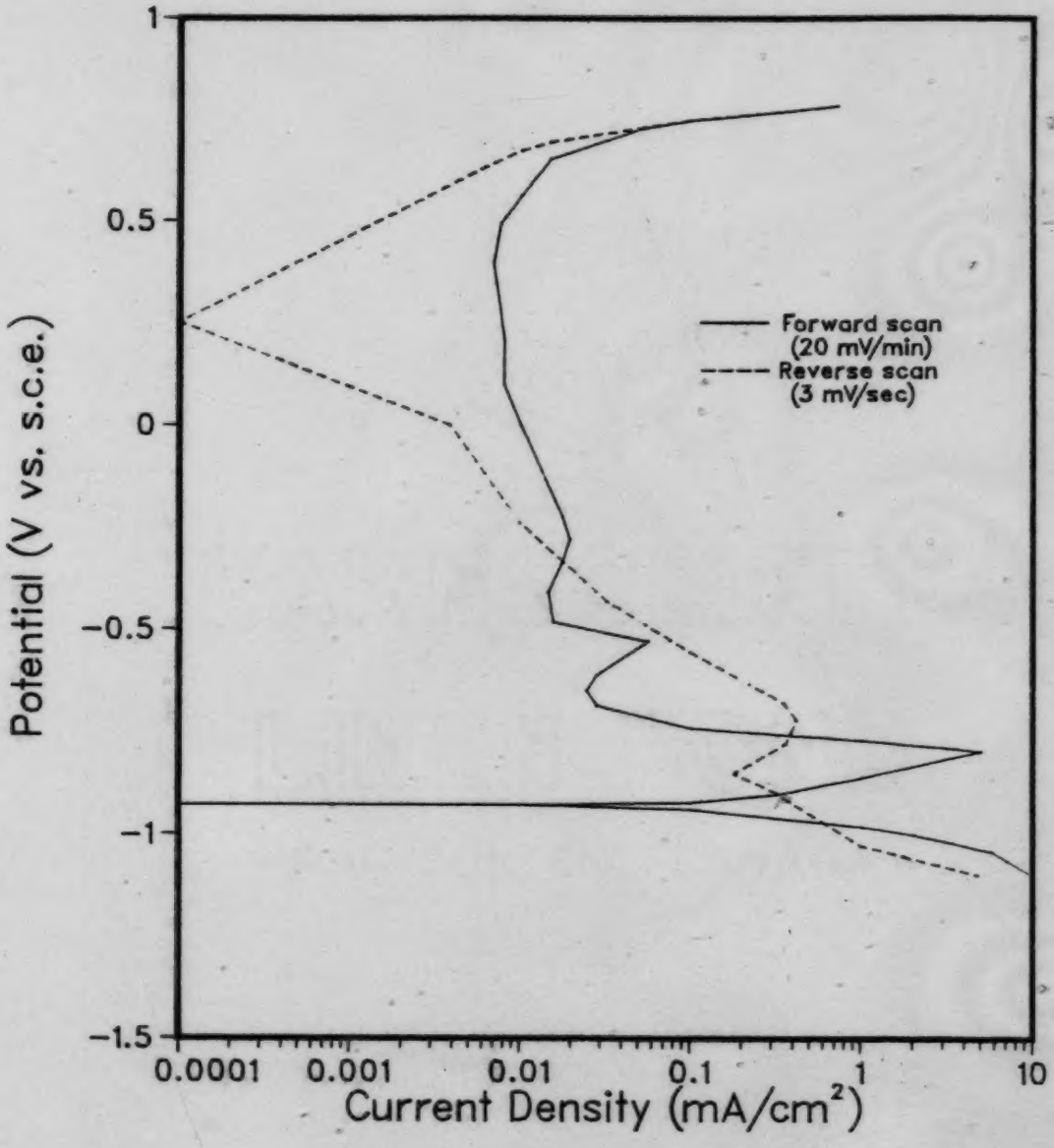

Figure 41. Polarization Curve of X-65 Steel at 90°C

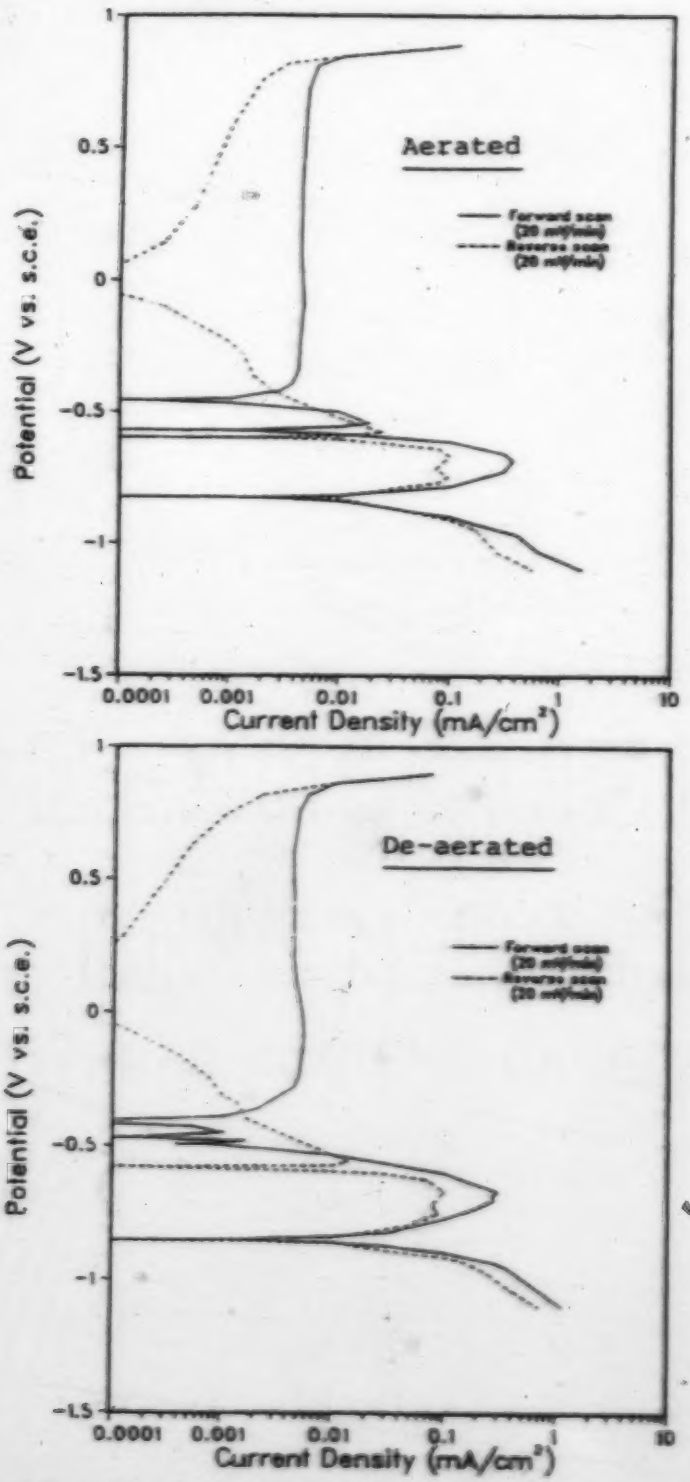

Figure 42. Polarization Curves of Dual-Phase Steel in Aerated and De-aerated Test Solution at 22°C

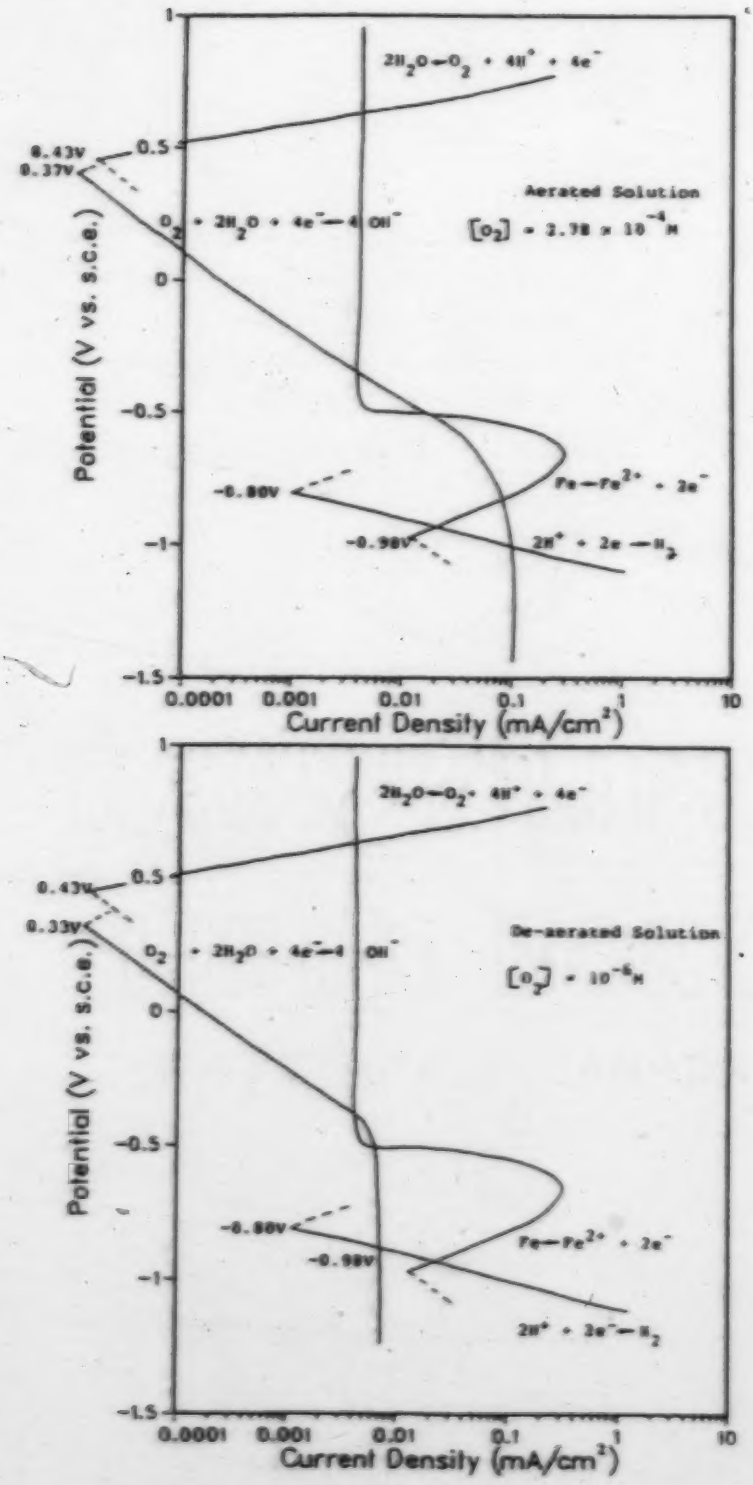

Figure 43. Polarization Curves showing the Effect of Oxygen

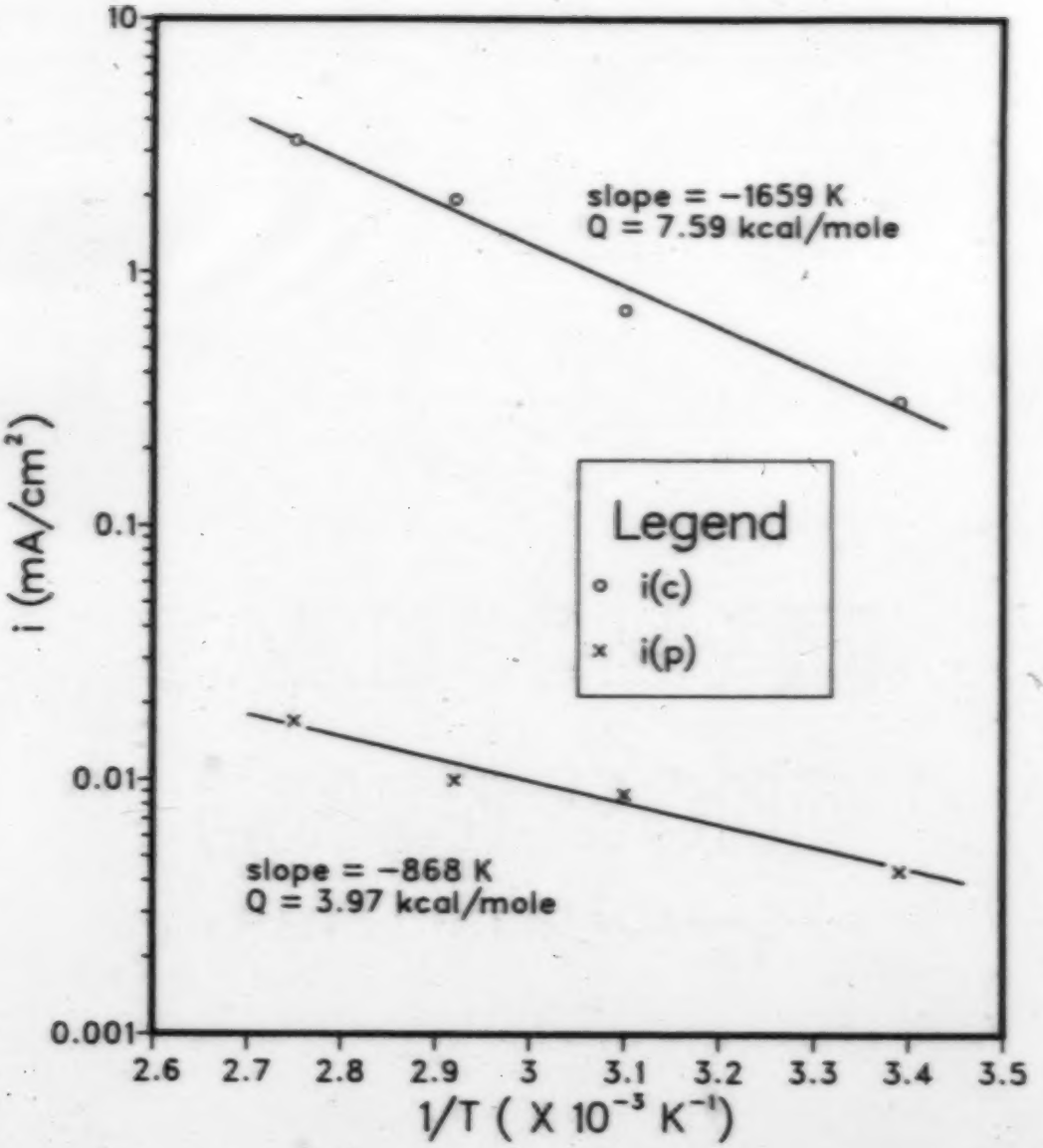

Figure 44. Log i(c) and log i(p) versus 1/T Plot for Dual-Phase Steel

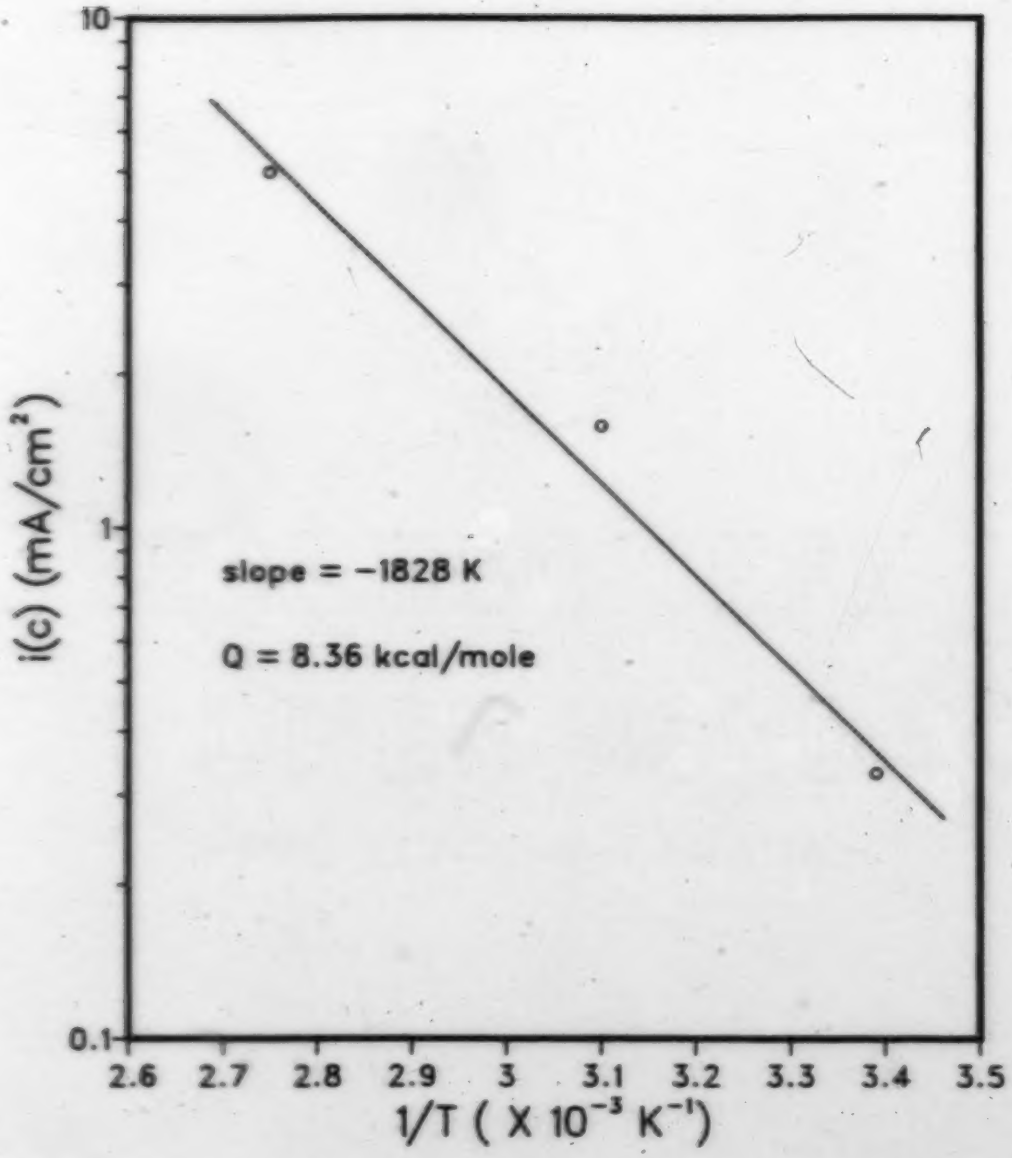

Figure 45. Log i(c) versus 1/T Plot for X-65 Steel

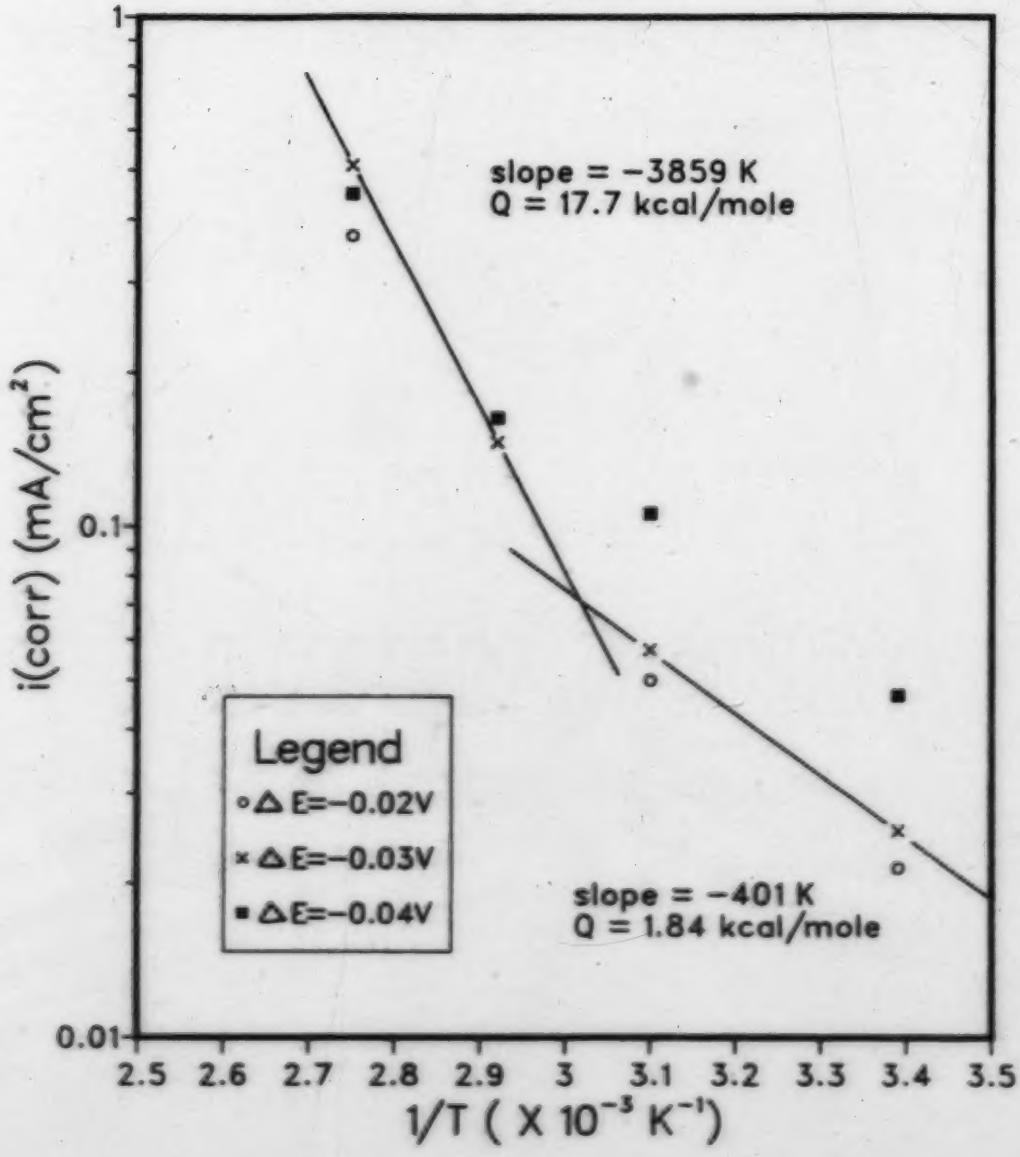

Figure 46. Log i(corr) versus 1/T Plot for Dual-Phase Steel

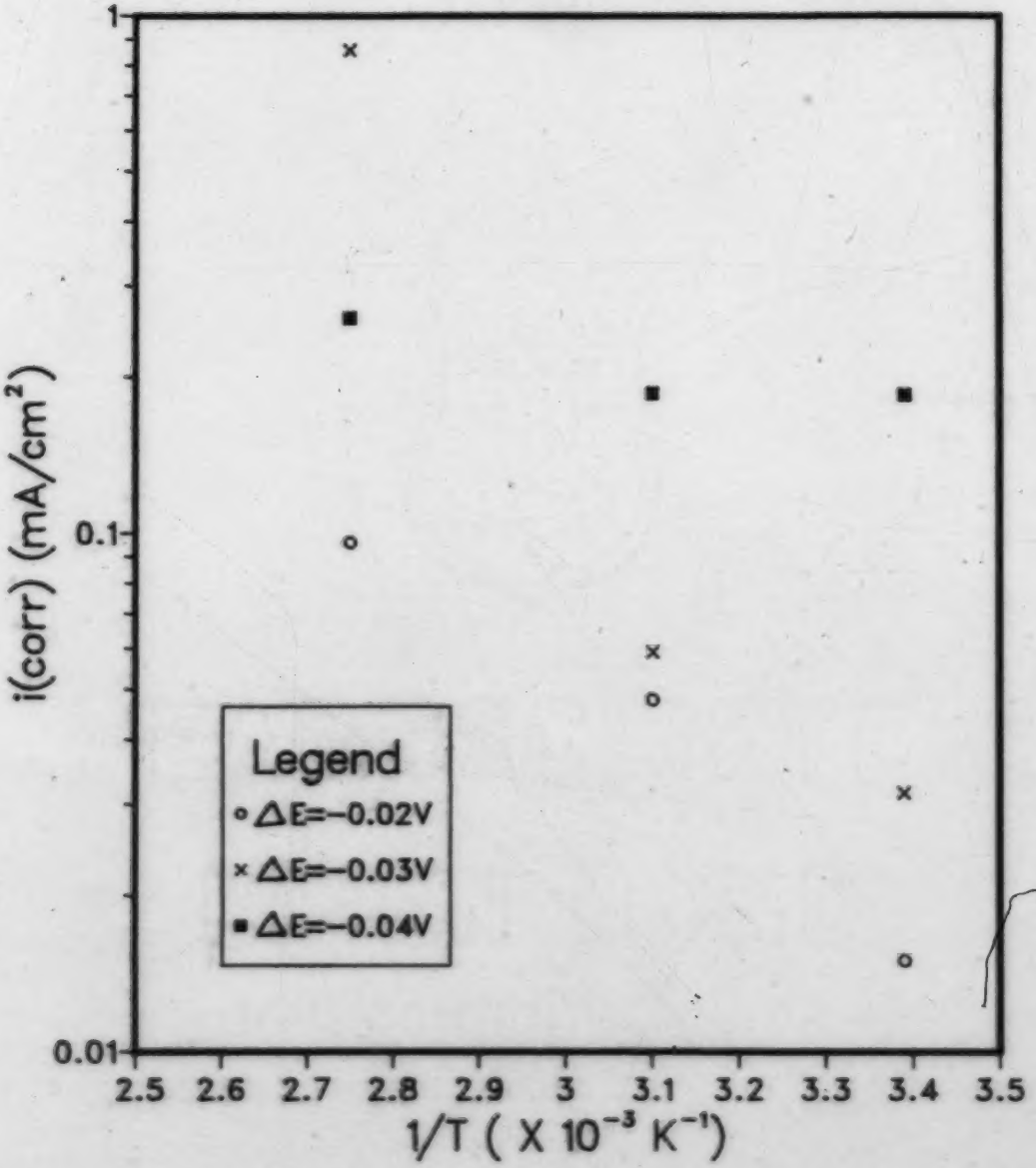

Figure 47. Log i(corr) versus 1/T Plot for X-65 Steel

Figure 48. Corrosion Attack of Dual-Phase Steel after 1 h at E(corr) and 50°C (600X)

Figure 49. Corrosion Attack of Dual-Phase Steel after 5 min at -0.800V vs. s.c.e. and 50°C (600X)

Figure 50. Corrosion Attack of Dual-Phase Steel after 5 min at E(pp) and 50°C (600X)

Figure 51. Corrosion Attack of Dual-Phase Steel after 5 min at -0.625V vs. s.c.e. and 50°C (600X)

Figure 52. Corrosion Attack of Dual-Phase Steel after 5 min at -0.600V vs. s.c.e. and 50°C (600X)

Figure 53. Corrosion Attack of X-65 Steel after 5 min at -0.790V vs. s.c.e. and 50°C (600X)

Figure 54. Corrosion Attack of X-65 Steel after 5 min at E(pp) and 50°C (600X)

Figure 55. Corrosion Attack of X-65 Steel after 5 min at -0.675V vs. s.c.e. and 50°C (600X)

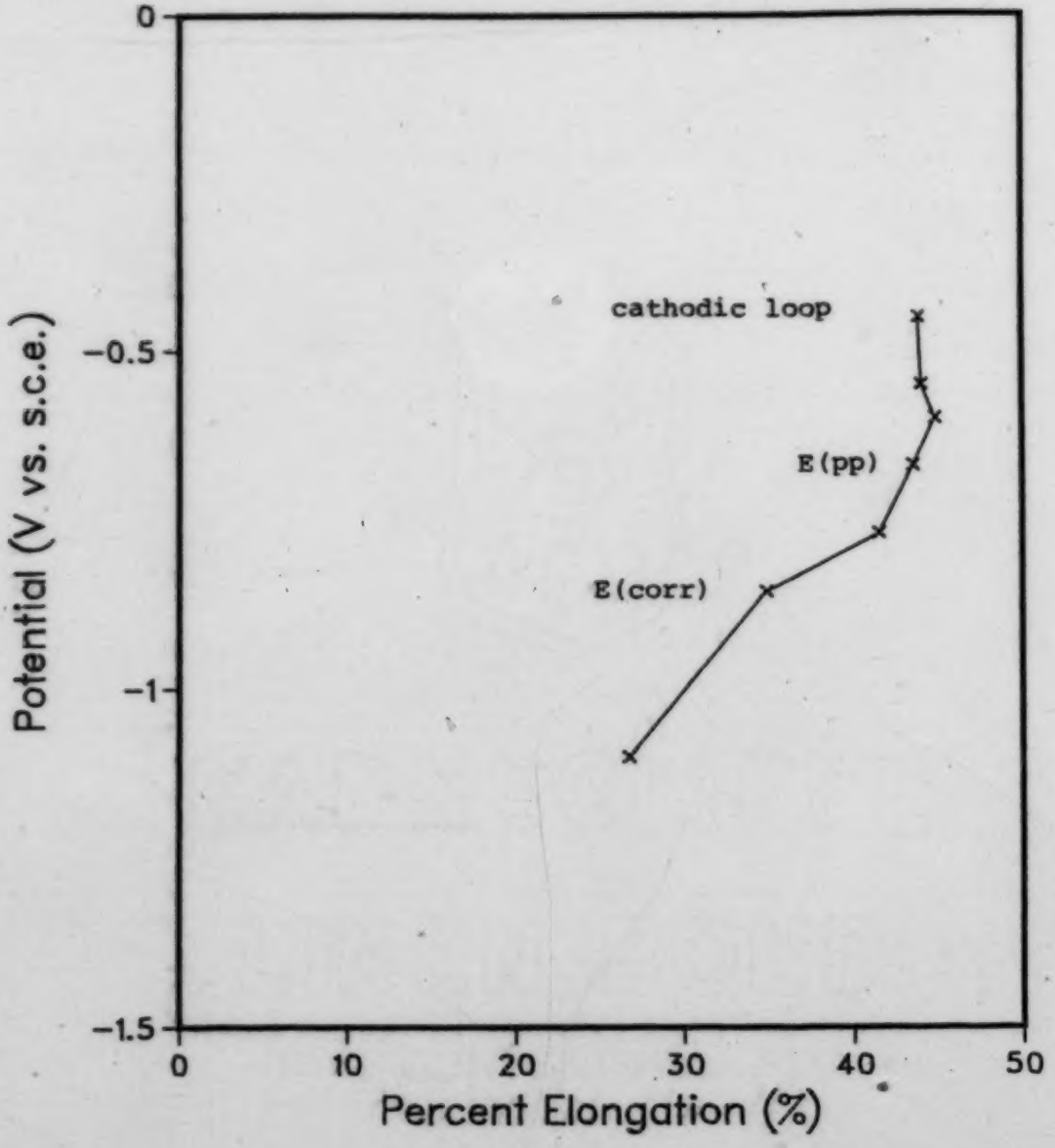

Figure 56. Percent Elongation as a function of Potential for Dual-Phase Steel at 21°C

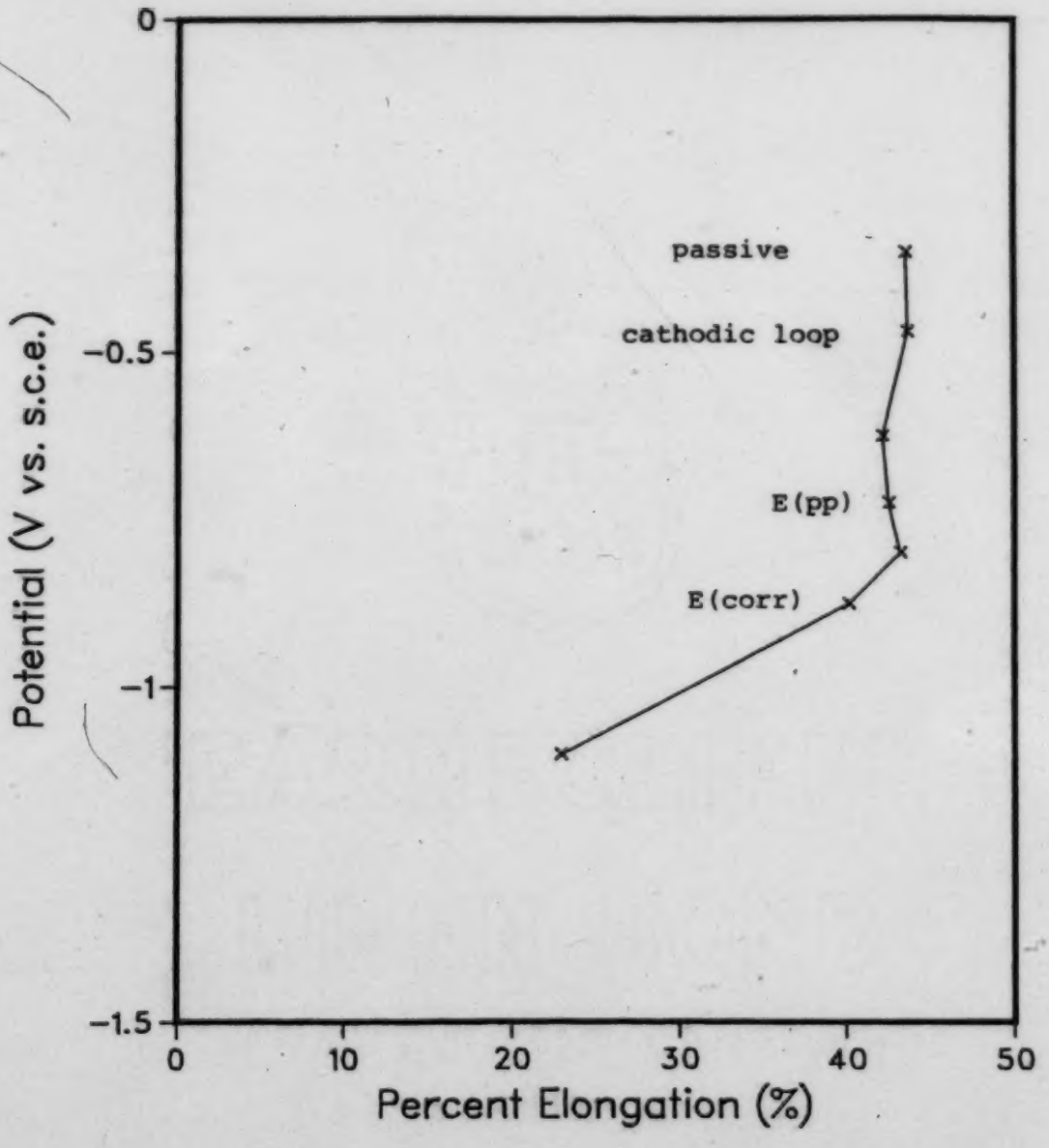

Figure 57. Percent Elongation as a function of Potential for Dual-Phase Steel at 50°C

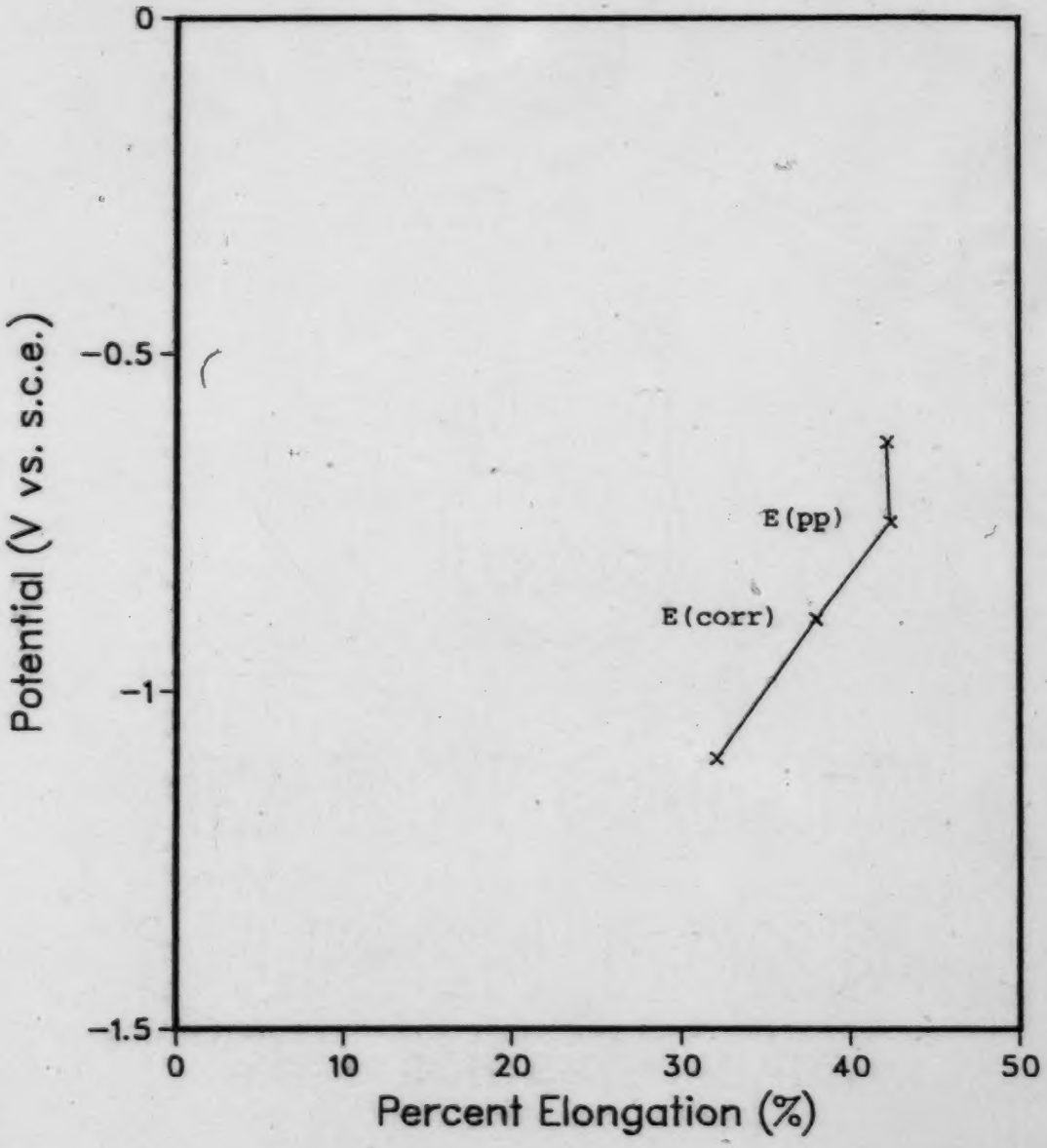

Figure 58. Percent Elongation as a function of Potential for Dual-Phase Steel at 70°C

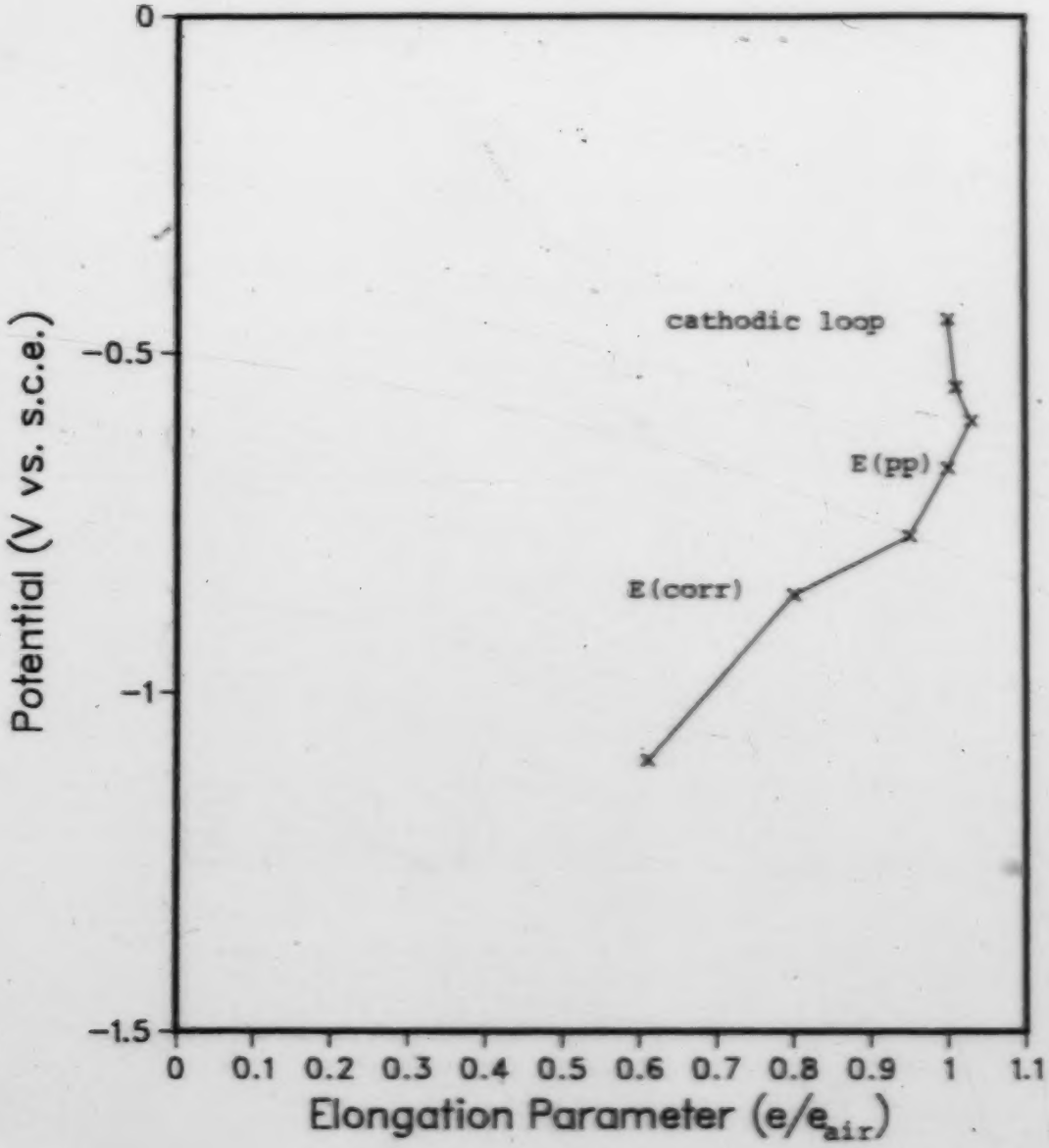

Figure 59. Elongation Parameter as a function of Potential for Dual-Phase Steel at 21°C

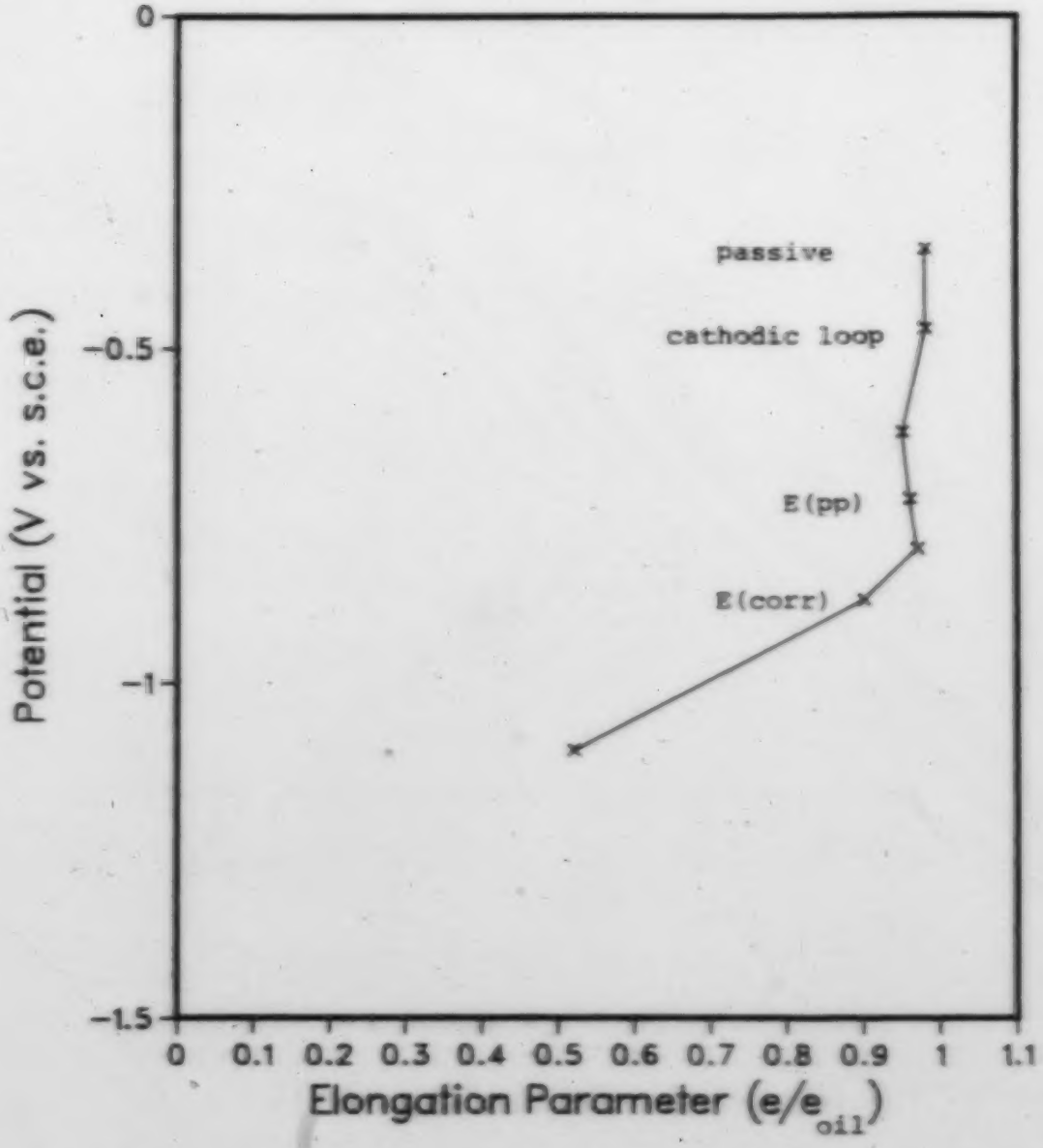

Figure 60. Elongation Parameter as a function of Potential for Dual-Phase Steel at 50°C

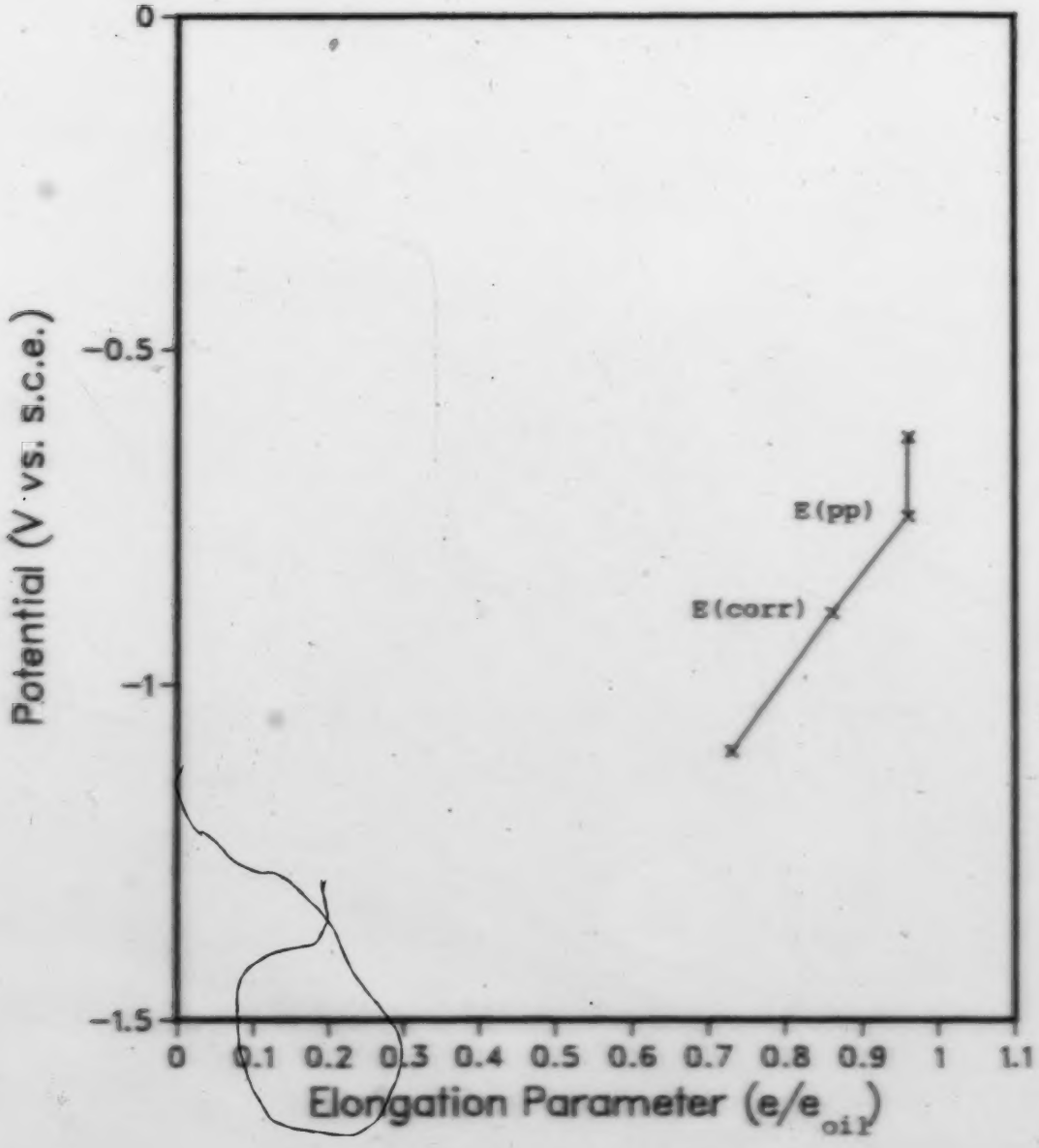

Figure 61. Elongation Parameter as a function of Potential for Dual-Phase Steel at 70°C

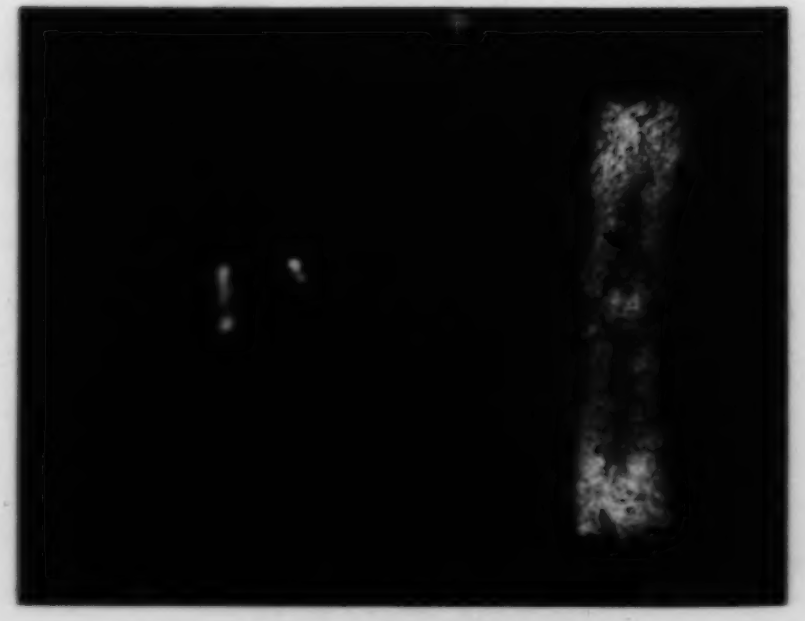

Figure 62. Specimen 1 (6.4X)

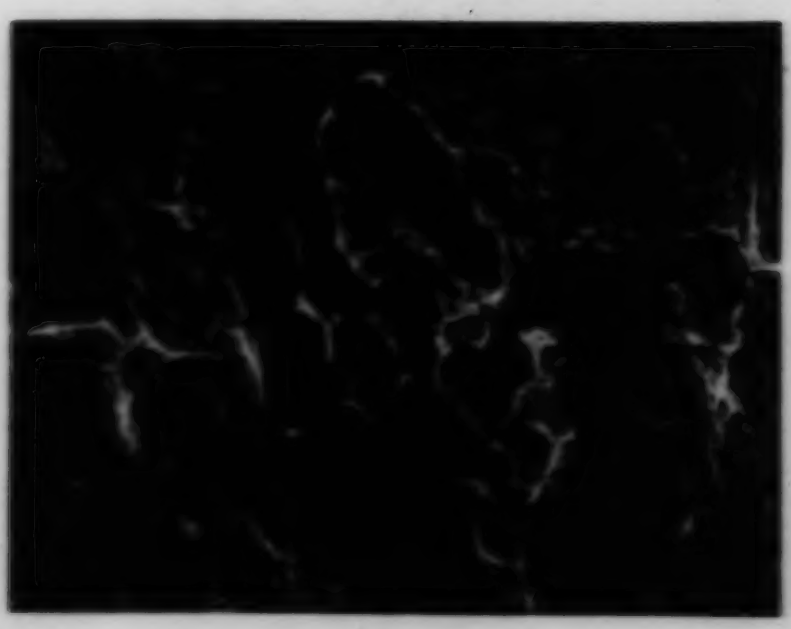

Figure 63. SEM Fractograph of Specimen 28 (1500X)

Figure 64. Specimen 12 (6.4X)

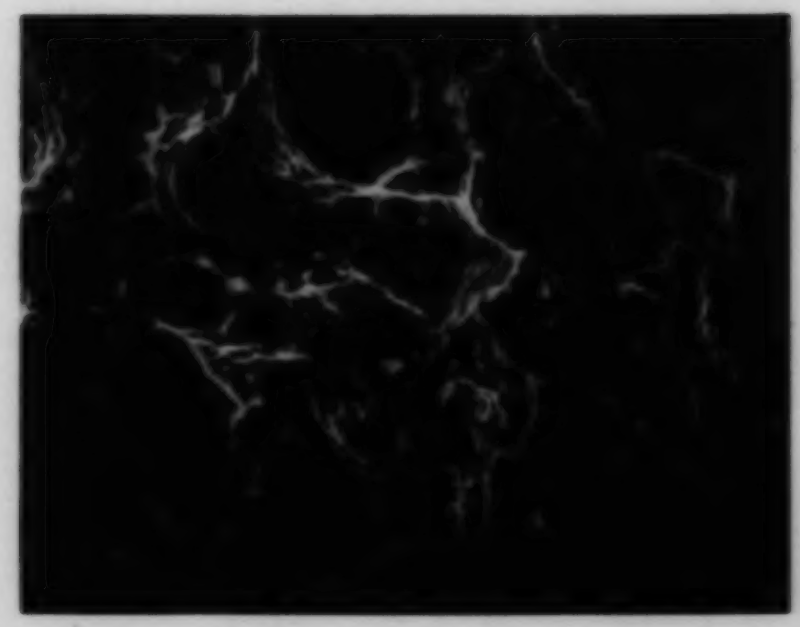

Figure 65. SEM Fractograph (cracked region) of Specimen 12 (1500X)

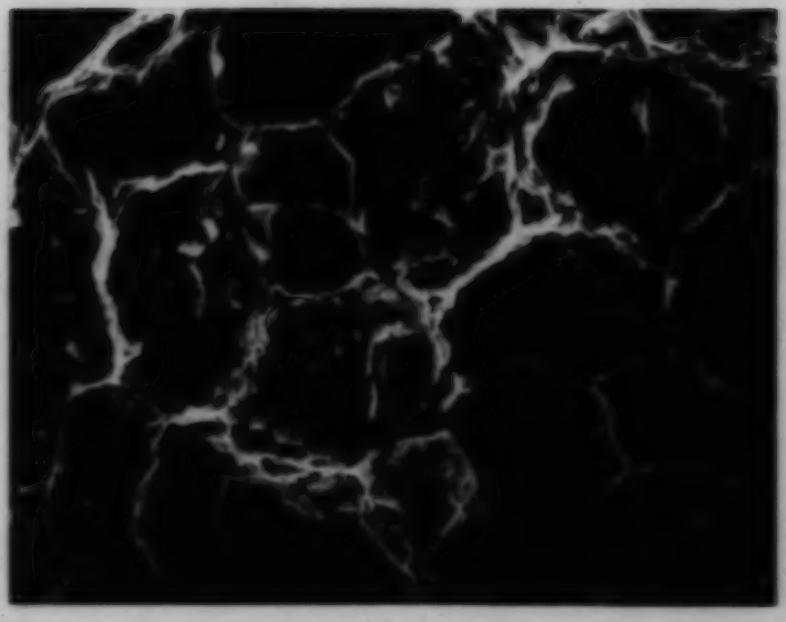

Figure 66. SEM Fractograph (overload region) of Specimen 12 (1500X)

Figure 67. Specimen 6 (6.4X)

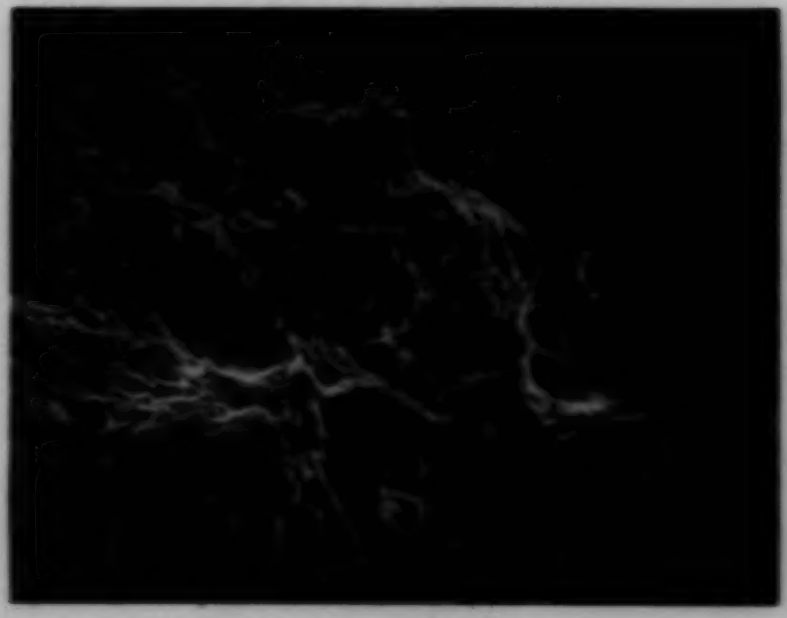

Figure 68. SEM Practograph of Specimen 6 (1500X)

Figure 69. Specimen 33 (6.4X)

Figure 70. SEM Fractograph of Specimen 33 (1500X)

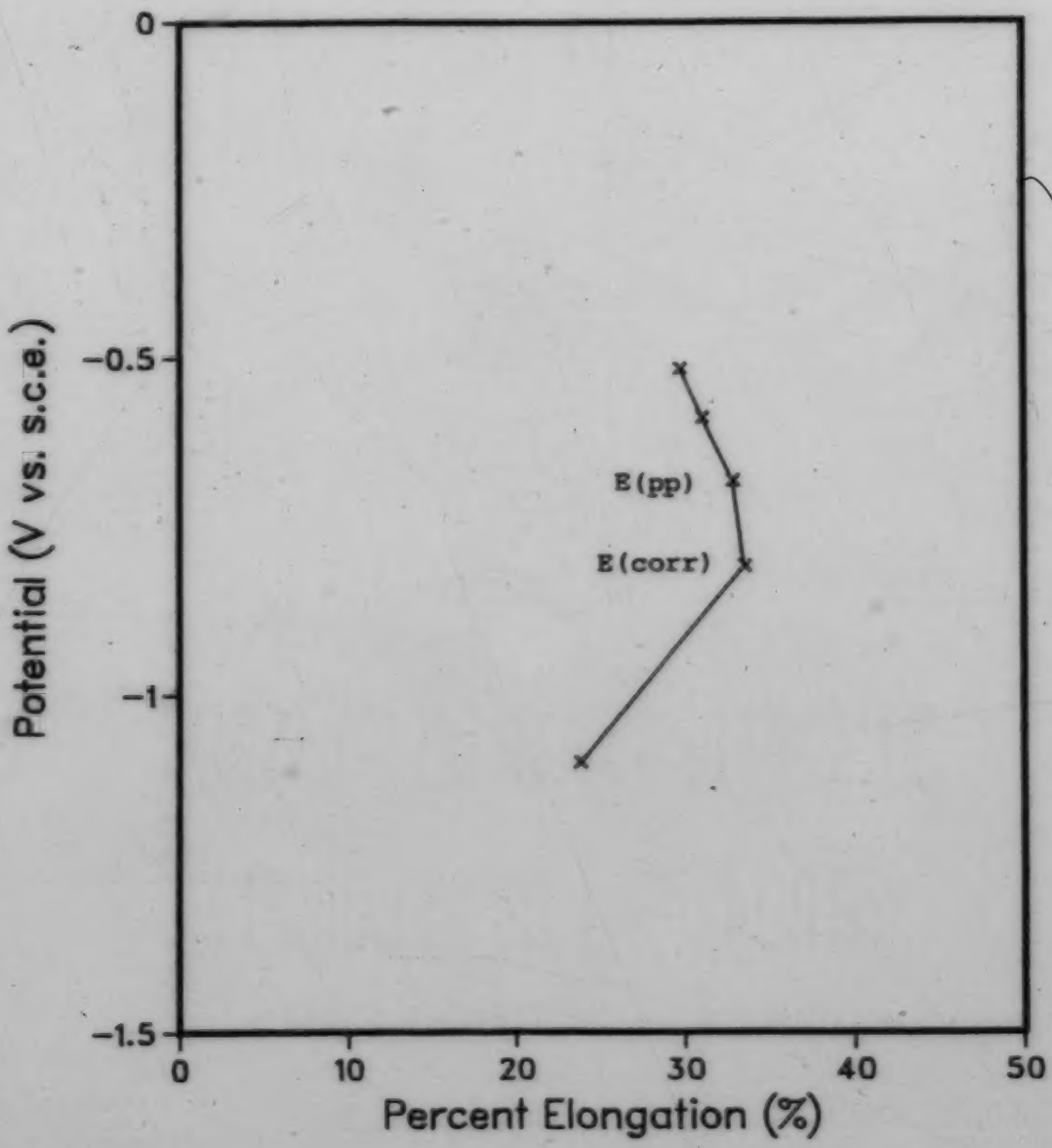

Figure 71. Percent Elongation as a function of Potential for X-65 Steel at 21°C

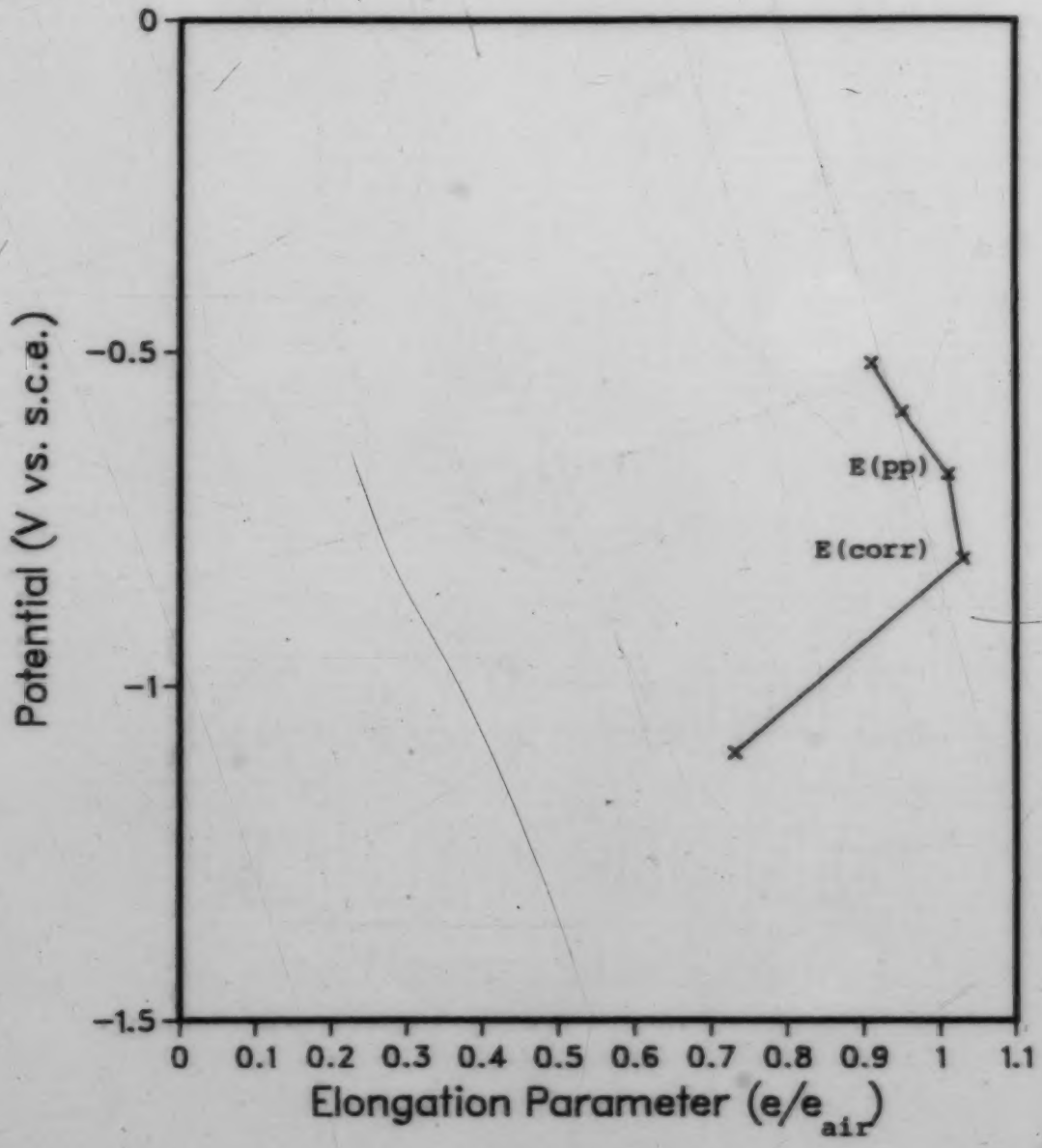

Figure 72. Elongation Parameter as a function of Potential for X-65 Steel at 21°C

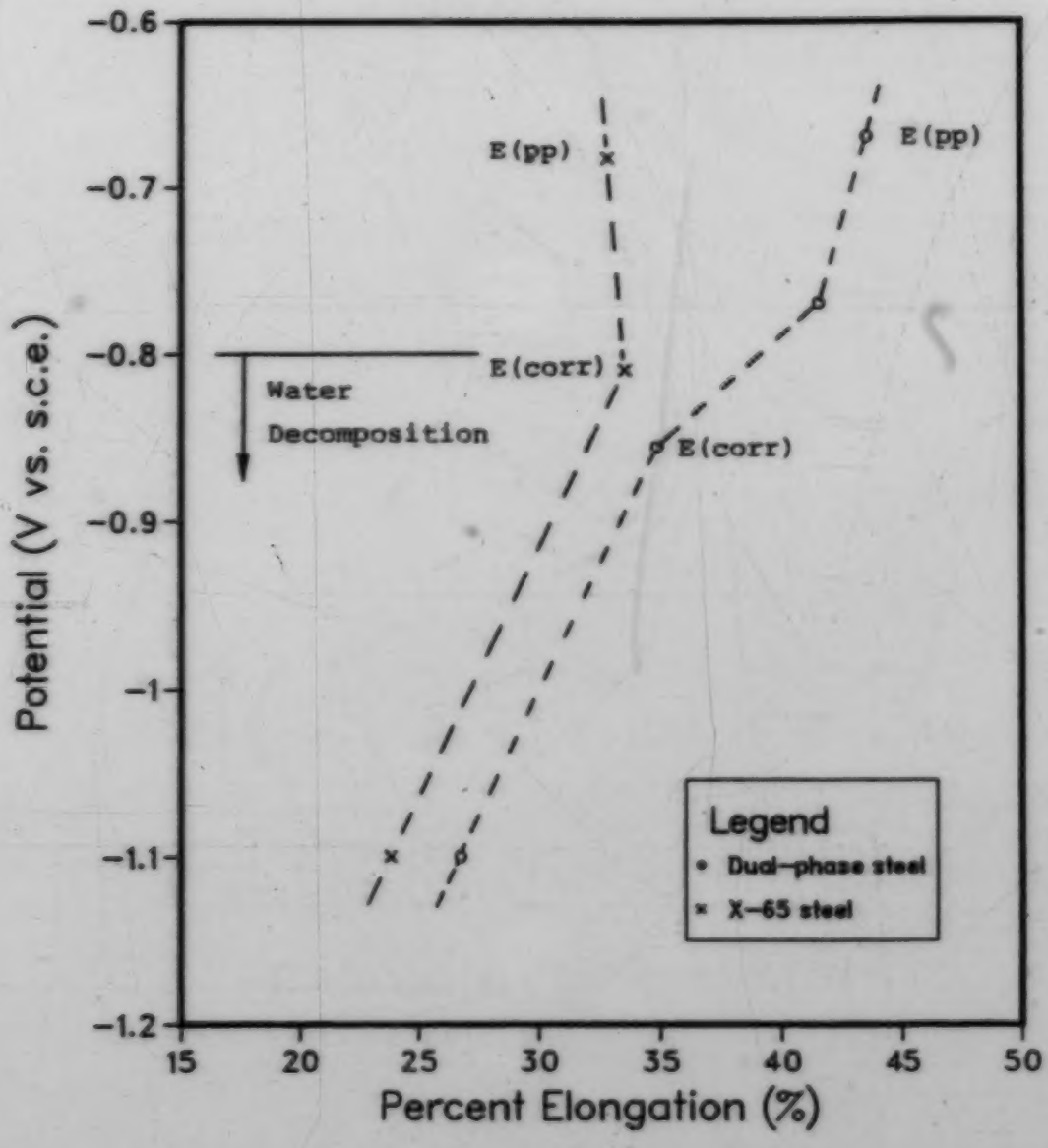

Figure 73. Effect of Hydrogen Charging on Percent Elongation of Dual-Phase Steel and X-65 Steel at 21°C

References

1. Sutcliffe, J.M., Fessler, R.R., Boyd, W.K., and Parkins, R.N., Stress Corrosion Cracking of Carbon Steel in Carbonate Solutions. *Corrosion*, Vol. 28, p. 313 (1972).
2. Payer, J.H., Berry, W.E., and Parkins, R.N., *Stress Corrosion Cracking - The Slow Strain-Rate Technique*, ASTM STP 665, Ugiansky, G.M. and Payer, J.H., Eds.; p. 222 (1979).
3. Payer, J.H., Berry, W.E., and Boyd, W.K., *Stress Corrosion - New Approaches*, ASTM STP 610, Craig, H.L., Jr., Ed.; p. 82 (1976).
4. Pourbaix, M.M., *Atlas of Electrochemical Equilibria in Aqueous Solutions*. NACE, Houston, Texas (1974).
5. Wagner, C. and Traud, W., *Z. Elektrochem.*, Vol. 44, p. 391 (1938).
6. Barnartt, S., Electrochemical Nature of Corrosion. *Electrochemical Techniques for Corrosion*, Baboian, R., Ed., NACE, p. 1 (1977).
7. Barnartt, S., Two-Point and Three-Point Methods for the Investigation of Electrode Reaction Mechanisms. *Electrochimica Acta*, Vol. 15, p. 1313 (1970).
8. Barnartt, S. and Donaldson, M., Three-Point Method for Evaluating Corrosion Current and Tafel Slopes From a Single Polarization Curve. *Corrosion*, Vol. 39, p. 33 (1983).
9. Hooke, R. and Jeeves, T.A., *Assoc. Computer Machinery*,

Vol. 8, p. 212 (1961).

10. Payer, J.H., Berry, W.E., and Boyd, W.K., *Stress Corrosion Cracking - The Slow Strain-Rate Technique*, ASTM STP 665, Ugiansky, G.M. and Payer, J.H., Eds., p. 61 (1979).

11. Almquist, W.E., Control of Pipeline Stress Corrosion Cracking is Probed. *Oil and Gas Journal*, p. 68, Oct. 23, 1979.

12. Fessler, R.R., Groeneveld, T.P., and Elsea, A.R., *Stress Corrosion Cracking and Hydrogen Embrittlement of Iron Base Alloys, (Conf. Proc.)*, Unieux-Firminy, France, June 12-16, 1973.

13. Fessler, R.R. and Barlo, T.J., Many Causes Possible For Stress-Corrosion Cracking. *Pipeline and Gas Journal*, p. 25, March 1979.

14. Parkins, R.N. and Fessler, R.R., Stress Corrosion Cracking of High-Pressure Gas Transmission Pipelines. *Int. J.Mater. Eng. Appl.*, p. 80, Dec. 1978.

15. Fessler, R.R., Status Report on Prevention of SCC in Buried Pipelines. *Oil and Gas*, Vol. 80, No. 20, p. 68 (1982).

16. Fessler, R.R., Preventative Measures for Pipeline SCC Described. *Oil and Gas J.*,p. 78, Jan. 7, 1980.

17. Thomas, J.G.N., Nurse, T.J., and Walker, R., Anodic Passivation of Iron in Carbonate Solutions. *British Corrosion Journal*, Vol. 5, p. 87 (1970).

18. Henthorne, M. and Parkins, R.N., Some Aspects of the

Influence of Structure upon Stress Corrosion Cracking and Grain Boundary Corrosion in Mild Steels. *British Corrosion Journal*, Vol. 2, p. 186 (1967).

19. Parkins, R.N., Predictive Approaches to Stress Corrosion Cracking Failure. *Corrosion Science*, Vol. 20, p. 147 (1980).
20. Parkins, R.N., Slattery, P.W., and Poulson, B.S., The Effects of Alloy Additions to Ferritic Steels Upon Stress Corrosion Cracking Resistance. *Corrosion*, Vol. 37, p. 650 (1981).
21. Zakroczmski, T. and Parkins, R.N., *Corrosion Science*, Vol. 20, p. 723 (1980).
22. Parkins, R.N., Environment Sensitive Fracture-Controlling Parameters. *Mech. Behav. of Matls.*, (Conf. Proc.), Cambridge, England, p. 139, Aug. 1979.
23. Kim, N.J., The Physical Metallurgy of HSLA Linepipe Steels - A Review. *Journal of Metals*, Vol. 35, p. 21 (April 1983).
24. Speich, G.R., Physical Metallurgy of Dual-Phase Steels. *Fundamentals of Dual-Phase Steels*, AIME, Kot, R.A. and Bramfitt, B.L., Eds.; p. 3 (1981).
25. Davies, R.G. and Magee, C.L., Physical Metallurgy of Automotive High-Strength Steels. *Structure and Properties of Dual-Phase Steels*, AIME, Davenport, A.T., Ed.; p. 1 (1979).
26. Repas, P.E., Metallurgy, Production, Technology, and

Properties of Dual-Phase Steels. *Dual-Phase and Cold-Forming Vanadium Steels in the Automobile Industry*, Vanitec, Berlin, p. 13 (1978).

27. Matsuoka, T. and Yamomori, K., Metallurgical Aspects of Cold-Rolled High Strength Steel Sheets. *Met. Trans. A*, Vol. 6A, p. 1613 (1975).

28. Davies, R.G., Influence of Martensite Composition and Content on the Properties of Dual-Phase Steels. *Met. Trans. A*, Vol 9A, p. 671 (1978).

29. Koo, J.Y., Young, M.J., and Thomas, G., On the Law of Mixtures in Dual-Phase Steels. *Met. Trans. A*, Vol. 11A, p. 852 (1980).

30. Davies, R.G., Effect of Silicon and Phosphorus on the Mechanical Properties of Both Ferrite and Dual-Phase Steels. *Met. Trans. A*, Vol. 10A, p. 113 (1979).

31. Becker, J. and Hornbogen, E., Microscopic Analysis of the Formation of Dual-Phase Steels, *Structure and Properties of Dual-Phase Steels*, AIME, Kot, R.A. and Morris, J.W., Eds.; p. 20 (1979).

32. Thomas, G. and Koo, J.Y., Developments in Strong, Duplex, Ferritic-Martensitic Steels. *Structure and Properties of Dual-Phase Steels*, AIME, Kot, R.A. and Morris, J.W., Eds.; p. 183 (1979).

33. Hayami, S., Furakawa, T., Gondoh, H., and Takechi, H., *Formable HSLA and Dual-Phase Steels*, AIME, Kot, R.A. and Morris, J.W., Eds.; p. 169 (1979).

34. Huppi, G.S., Matlock, P.K., and Krauss, G., An

Evaluation of the Importance of Epitaxial Ferrite in Dual-Phase Microstructures. *Scripta Met.*, Vol. 14, p. 1239 (1980).

35. Marder, A.R., Factors Affecting the Ductility of 'Dual-Phase' Alloys. *Formable HSLA and Dual-Phase Steels*, AIME, Kot, R.A. and Morris, J.W., Eds.; p. 89 (1979).

36. Rashid, M.S. and Rao, B.V.N., Tempering Characteristics of a Vanadium Containing Dual-Phase Steel. *Fundamentals of Dual-Phase Steels*, (Conf. Proc.), AIME, Kot, R.A. and Bramfitt, B.L., Eds.; p. 3 (1981).

37. Davies, R.G., Hydrogen Embrittlement of Dual-Phase Steels. *Met. Trans. A*, Vol. 12A, p. 1667 (1981).

38. Pierce, C.L., Stress Corrosion Cracking of a Dual-Phase Steel. Unpublished undergraduate report, Dept. of Mineral Engineering, University of Alberta (1981).

39. Stiksma, J., Stress Corrosion Cracking of a Dual-Phase Steel. Unpublished undergraduate report, Dept. of Mineral Engineering, University of Alberta (1982).

40. LePera, F.S., Improved Etching Technique to Emphasize Martensite and Bainite in High-Strength Dual-Phase Steel. *Journal of Metals*, Vol. 32, p. 38, March 1980.

41. Kayafas, I., Corrosion Product Removal From Steel Fracture Surfaces for Metallographic Examination. *Corrosion*, Vol. 36, p. 443 (1980).

Appendix A

Corrosion Rate Determination

Figure A.1 illustrates which points (i,E) are used in the 3-point method for determining the corrosion rate from polarization curves. Table A.1 lists the points obtained from the polarization curves of dual-phase steel and X-65 steel at different temperatures.

An example calculation follows.

Dual-Phase Steel, 22°C, ΔE=-0.04V

$i(\Delta E) = 0.0869$ mA/cm²

$i(2\Delta E) = 0.278$ mA/cm²

$i(-2\Delta E) = 0.0970$ mA/cm²

two ratios:

$$r_1 = i(2\Delta E)/i(-2\Delta E) = 2.87$$

$$r_2 = i(2\Delta E)/i(\Delta E) = 3.20$$

quadratic relationship:

$$u^2 - r_2 u + \sqrt{r_1} = 0$$

$$u = r_2 \pm \sqrt{r_2^2 - 4\sqrt{r_1}} / 2$$

where

$$u_1 = r_2 + \sqrt{r_2^2 - 4\sqrt{r_1}} / 2 = \exp(2.303\Delta E/\beta_c) = 2.53$$

and

$$u_2 = r_2 - \sqrt{r_2^2 - 4\sqrt{r_1}} / 2 = \exp(2.303\Delta E/\beta_a) = 0.669$$

also

$$i(\Delta E)/i(corr) = \pm(u_1 - u_2)$$

results: $\beta_c = -0.0992$ V/decade

$\beta_a = 0.229$ V/decade

$i(corr) = 0.0869$ mA/cm² / 1.86 = 0.0467 mA/cm²

Table A.1. Current Densities Obtained From Polarization Curves

Dual-Phase Steel

Temp. (°C)	ΔE (V)	i(ΔE) (mA/cm²)	i(2ΔE) (mA/cm²)	i(-2ΔE) (mA/cm²)
22	-0.02	0.030	0.869	0.0333
50	-0.02	0.0819	0.223	0.161
70	-0.02	0.256	0.471	0.399
90	-0.02	0.437	1.00	1.076
22 *	-0.02	0.0261	0.0552	0.0521
22	-0.03	0.0526	0.176	0.0584
50	-0.03	0.142	0.488	0.240
70	-0.03	0.339	1.12	0.575
90	-0.03	0.709	1.75	1.585
22 *	-0.03	0.0341	0.0668	0.130
22	-0.04	0.0869	0.278	0.0970
50	-0.04	0.223	0.912	0.387
70	-0.04	0.471	1.81	0.702
90	-0.04	1.00	3.08	2.38
22 *	-0.04	0.0552	0.190	0.171

* - test solution saturated with oxygen.

X-65 Pipeline Steel

Temp. (°C)	ΔE (V)	i(ΔE) (mA/cm²)	i(2ΔE) (mA/cm²)	i(-2ΔE) (mA/cm²)
22	-0.02	0.0295	0.0912	0.0447
50	-0.02	0.122	0.440	0.166
90	-0.02	0.214	0.692	0.372
22	-0.03	0.0525	0.154	0.0731
50	-0.03	0.207	0.913	0.285
90	-0.03	0.550	1.288	0.805
22	-0.04	0.0912	0.229	0.100
50	-0.04	0.440	1.40	0.440
90	-0.04	0.692	2.50	1.13

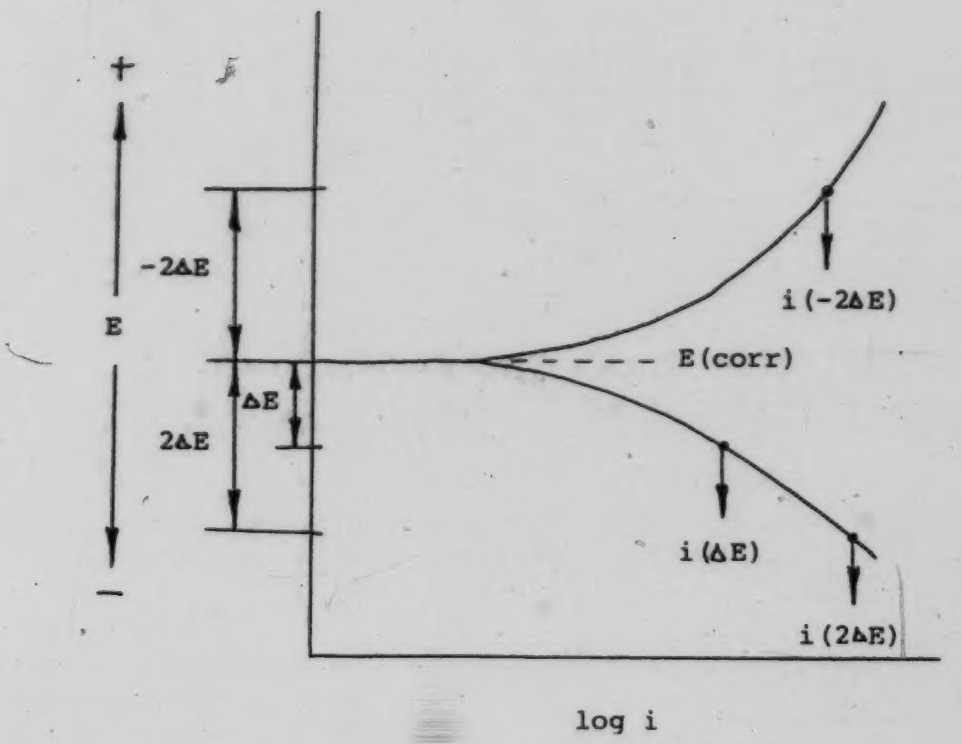

Figure A.1. 3-Point Method